

DISSERTATION  
SUBMITTED TO THE  
COMBINED FACULTIES OF THE NATURAL SCIENCES AND  
MATHEMATICS  
OF THE RUPERTO-CAROLA-UNIVERSITY OF HEIDELBERG, GERMANY  
FOR THE DEGREE OF  
DOCTOR OF NATURAL SCIENCES

PUT FORWARD BY

MASTER PHYS. NATALIA SERGEEVNA KUDRYAVTSEVA  
BORN IN: MOSCOW REGION (RUSSIA)

ORAL EXAMINATION: OCTOBER 15th, 2012

MICRO-ARCSECOND ASTROMETRY OF EXOPLANET HOST  
STARS AND STARBURST CLUSTERS

REFEREES:            PROF. DR. THOMAS HENNING  
                          PROF. DR. JOCHEN HEIDT

---

## Zusammenfassung

Seit Erscheinen der ersten Sternenkataloge hat sich die astrometrische Genauigkeit von Positionsmessungen enorm gesteigert. In meiner Arbeit benutze ich die astrometrischen Techniken, um Starburst Cluster zu untersuchen und diskutiere wie diese unser Wissen über Exoplaneten in Zukunft vergrößern werden. Im ersten Teil dieser Arbeit diskutiere ich die beiden galaktischen Starburst Cluster Westerlund 1 (Wd 1) und NGC 3603 YC, welche zu den massereichsten jungen Sternhaufen in unserer Galaxie zählen. Mithilfe einer astrometrischen sowie photometrischen Analyse der Beobachtungen dieser Cluster mittels adaptiver Optik sowie dem Hubble Space Teleskop untersuche ich auf welchen Zeitskalen sich diese Cluster gebildet haben. Als eine obere Grenze für die Altersunterschiede der Sterne finde ich 0.4 Mio Jahre für den 4 bis 5 Mio Jahre alten Sternhaufen Wd 1 und 0.1 Mio Jahre für den 1 bis 2 Mio Jahre alten NGC 3603 YC. Demzufolge erfolgte in beiden Sternhaufen die Sternentstehung nahezu instantan.

Der zweite Teil dieser Arbeit behandelt die kinematischen Eigenschaften wie auch die ursprüngliche Massenverteilung (IMF) der Sterne in Wd 1. Eine astrometrische Analyse von Aufnahmen mehrerer Epochen im nahen Infrarot wurde hierbei vorgenommen, um Haufenmitglieder von Feldsternen zu unterscheiden. Dadurch konnte eine zuverlässige Geschwindigkeitsverteilung der Sterne bestimmt werden sowie eine IMF Steigung für den Kern des Sternhaufens ( $R < 0.23$  pc) von  $\Gamma = -0.46$ .

Der letzte Teil meiner Arbeit beschäftigt sich mit den Erfolgsaussichten der Planetensuche mit GRAVITY. GRAVITY, ein Instrument der zweiten Generation für das Very Large Telescope Interferometer, soll relative Astrometrie von  $10 \mu\text{as}$  erreichen. Hier diskutiere ich die Entdeckung und Charakterisierung von Exoplaneten bis hinunter zu einigen Erdmassen, ermöglicht durch die hohe Empfindlichkeit von GRAVITY. Weiterhin erstelle ich eine erste Quellenliste.

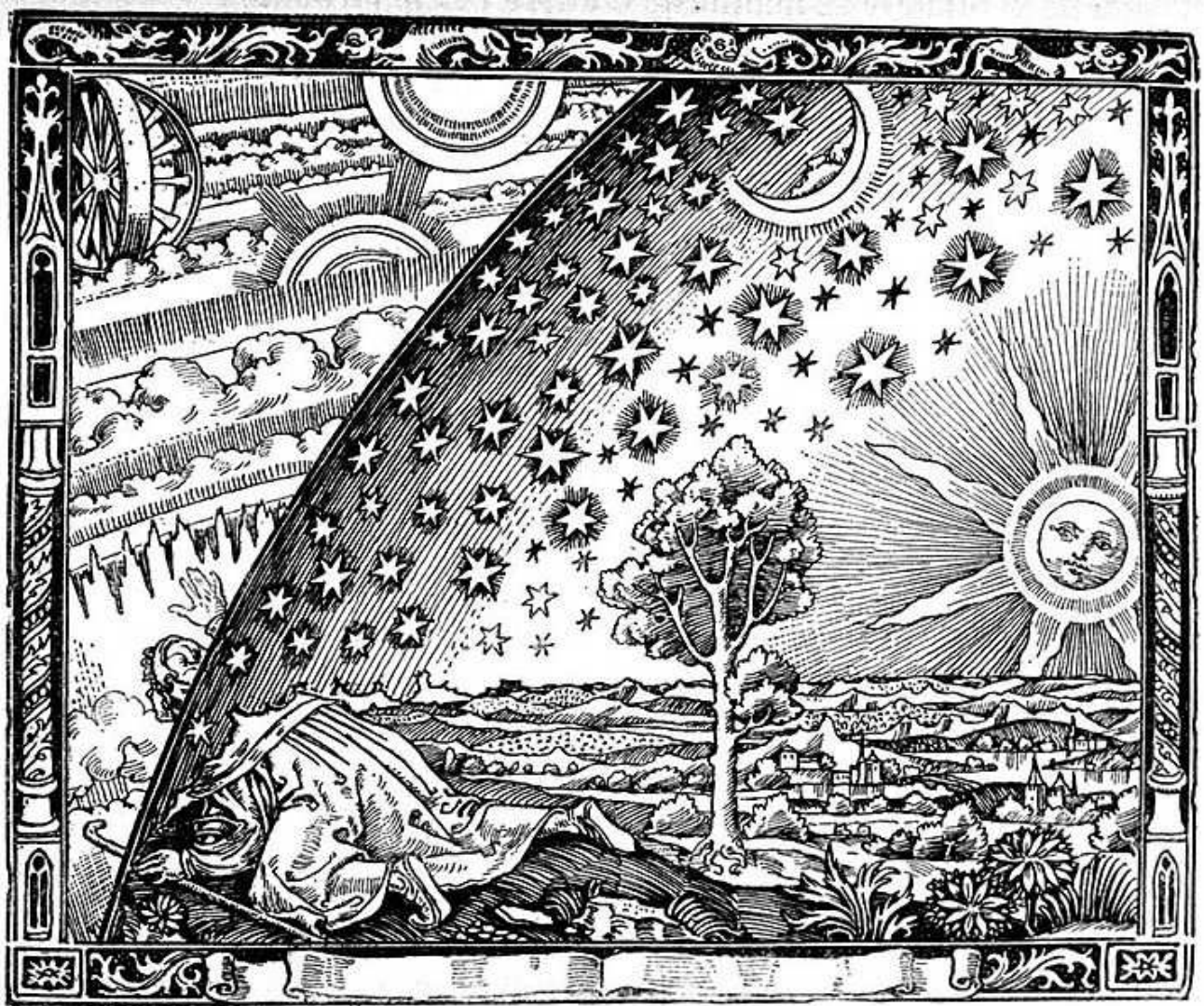
## Abstract

Since the first star catalogues tremendous progress in the astrometric accuracy of positional observations has been achieved. In this thesis, I show how beneficial astrometric techniques are already today for the study of starburst clusters, and how astrometry will fundamentally improve our knowledge on exoplanets in the near future.

I first study two galactic starburst clusters, Westerlund 1 (Wd 1) and NGC 3603 YC, which are among the most massive young clusters in our Galaxy. I perform astrometric and photometric analyses of adaptive optics and Hubble Space Telescope observations of these clusters in order to understand on which time-scales these clusters formed. As a result, I derive upper limits for the age spreads of 0.4 Myr for the 4 to 5 Myr old cluster Wd 1, and 0.1 Myr for the 1 to 2 Myr old NGC 3603 YC. Thus, the star formation process in each of these clusters happened almost instantaneously.

The second part of this thesis deals with the dynamical properties and the initial mass function (IMF) of Wd 1. Astrometric analysis of multi-epoch, near-infrared adaptive optics observations of Wd 1 was used to distinguish the cluster's members from field stars. This lead to an unbiased determination of the internal velocity dispersion of the cluster, and an IMF slope of  $\Gamma = -0.46$  for the core of the cluster ( $R < 0.23$  pc).

The final part of this thesis is devoted to the future prospects of detecting exoplanets with the GRAVITY instrument. The second-generation Very Large Telescope Interferometer instrument GRAVITY aims at achieving  $10 \mu\text{as}$  accuracy. Here, I discuss the possibilities of detecting and characterizing exoplanets with masses down to a few Earth masses with the high sensitivity provided by GRAVITY, in addition to providing an initial target list.



A wood engraving by an unknown artist. First documented appearance is in Flammarion's 1888 book *L'atmosphère : météorologie populaire* ("The Atmosphere: Popular Meteorology").

# Contents

<b>List of Figures</b>	<b>vii</b>
<b>List of Tables</b>	<b>xi</b>
<b>1 Introduction</b>	<b>1</b>
1.1 The first steps in astrometry . . . . .	1
1.2 Hipparcos . . . . .	2
1.3 GAIA . . . . .	3
1.4 Adaptive Optics . . . . .	3
1.5 Astrometry of starburst clusters . . . . .	4
1.6 Long baseline astrometry . . . . .	6
<b>2 Instantaneous starburst of the massive clusters Wd 1 and NGC 3603 YC</b>	<b>9</b>
2.1 Introduction . . . . .	10
2.2 Method . . . . .	11
2.3 Observations and data reduction . . . . .	12
2.3.1 Observations of Wd 1 and NGC 3603 YC . . . . .	12
2.3.2 Completeness correction . . . . .	13
2.3.3 Proper motion selection . . . . .	16
2.4 CMD for Wd 1 and NGC 3603 YC . . . . .	18
2.5 Age likelihood for Wd 1 and NGC 3603 YC . . . . .	18
2.6 Broadening of the age likelihood function . . . . .	22
2.6.1 Photometric error . . . . .	22
2.6.2 Unresolved binarity . . . . .	23
2.6.3 Ongoing accretion . . . . .	25
2.6.4 Sensitivity to age spread . . . . .	26
2.7 Discussion . . . . .	26

## CONTENTS

---

<b>3</b>	<b>The Initial Mass Function and internal dynamics of the starburst cluster Westerlund 1 from near-infrared adaptive optics observations</b>	<b>29</b>
3.1	Introduction . . . . .	30
3.2	Observations . . . . .	31
3.3	Data reduction . . . . .	31
3.3.1	Geometric transformation . . . . .	33
3.3.2	Photometric errors . . . . .	33
3.4	Proper motion membership selection . . . . .	34
3.5	Dynamical properties of Wd 1 . . . . .	36
3.6	Colour-magnitude diagram of Wd 1 . . . . .	38
3.7	Completeness . . . . .	40
3.8	The initial mass function of Wd 1 . . . . .	41
3.9	Discussion and summary . . . . .	42
<b>4</b>	<b>Characterizing exoplanets with GRAVITY</b>	<b>47</b>
4.1	GRAVITY . . . . .	48
4.1.1	Scientific goals . . . . .	52
4.2	Astrometric detection of exoplanets with GRAVITY . . . . .	53
4.2.1	Introduction . . . . .	53
4.2.2	GRAVITY astrometric capability . . . . .	55
4.2.3	Observing strategy . . . . .	58
4.2.4	Target list . . . . .	58
4.3	Transiting exoplanet detection capabilities of GRAVITY . . . . .	61
4.4	Appendix . . . . .	63
<b>5</b>	<b>Conclusions</b>	<b>69</b>
5.1	Results on starburst clusters . . . . .	69
5.2	Results on exoplanets . . . . .	71
<b>6</b>	<b>Acronym</b>	<b>73</b>
	<b>Bibliography</b>	<b>75</b>

# List of Figures

1.1	The development of astrometric accuracy with time, starting from Tycho Brahe. . . . .	2
1.2	Adaptive optics working principle. Courtesy of S.Hippler. . . . .	4
1.3	The schematic location of the starburst clusters in the Milky Way. The yellow dot indicates the Sun. Courtesy of A.Stolte. . . . .	5
2.1	(a): VLT/NACO 2003 image of Wd 1 in $K_S$ -band. (b): HST/WFC3 2010 image of Wd 1 in F125W filter. The overlapping FOV with NACO is enclosed by a white box. (c): HST/WFPC2 2007 image of NGC 3603 YC in F814W filter. (b): HST/WFPC2 2007 image of NGC 3603 YC in F555W filter. . . . .	14
2.2	Average completeness for the WFC3/IR area overlapping with the NACO frame as a function of $m_{F125W}$ (a), for the NACO/VLT frame as a function of $m_{K_S}$ (b), for HST/WFPC2 images as functions of $m_{F555W}$ (c) and $m_{F814W}$ (d). Overplotted are Fermi-functions fitted to the data. . . . .	15
2.3	Proper motion diagram for Wd 1. Stars with proper motions less than 0.8 mas/year are marked by green asterisks. . . . .	16
2.4	Histograms of number of stars vs. proper motion in RA and DEC for Wd 1. Bin size is 0.3 mas/year. Dotted line is a Gaussian function fitted to the histogram. . . . .	17
2.5	Histogram of number of stars vs. cluster membership probability $P_{mem}$ for NGC 3603 YC. Bin size is 0.005. . . . .	17

## LIST OF FIGURES

---

2.6	Color-magnitude diagrams of Wd 1 (a) and NGC 3603 YC (b). Error bars indicate typical errors in color and magnitude. Red boxes show the regions that were taken for the analysis of the age spread. Proper motion selected stars for Wd 1 are marked by green asterisks. The CMD of NGC 3603 YC includes only stars with cluster membership probabilities more than 90%. FRANEC-Padova isochrones (blue) are overplotted. For Wd 1 this is a 5.0 Myr isochrone at $DM=13.0$ mag, for NGC 3603 YC a 2.0 Myr isochrone at $DM=14.1$ mag. . . . .	19
2.7	Two-color diagram of NGC 3603 YC. Red points are simulated stars with masses $3 - 10M_{\odot}$ scattered within 0.025 mag. . . . .	20
2.8	Photometric error of stars on VLT/NACO (a) and HST/WFC3 (b) images of Wd 1 and HST/WFPC2 images (c,d) of NGC 3603 YC. Each error value is averaged within 1 magnitude. . . . .	21
2.9	Two-dimensional map of log-likelihood $\log(L(t, DM))$ for Wd 1. . . . .	22
2.10	(a):Normalized $L(t)$ for Wd 1 at $DM=12.9$ mag. The red curve is a fitted Gaussian. (b):The same at $DM=13.0$ mag. (c):The same at $DM=13.1$ mag. (d):Normalized $L(t)$ for the simulated 5.0 Myr population at $DM=13.0$ mag. (e):Normalized $L(t)$ for the simulated 5.0 Myr population at $DM=13.0$ mag with a binarity fraction of 50%. (f):Normalized $L(t)$ for the simulated population with 70% of the stars being 5.0 Myr old and 30% being 4.5 Myr old. . . . .	23
2.11	Two-dimensional map of log-likelihood $\log(L(t, DM))$ for NGC 3603 YC. . . . .	24
2.12	Normalized $L(t)$ for NGC 3603 YC at $DM=14.0$ mag (a), $DM=14.1$ mag (b), $DM=14.2$ mag (c). Red curves are fitted Gaussian functions. . . . .	24
2.13	(a):CMD for the simulated 5.0 Myr population at $DM=13.0$ mag. The corresponding FRANEC-Padova isochrone (red) is overplotted. (b):CMD for the simulated 5.0 Myr population with a binarity fraction of 50% at $DM=13.0$ mag. Red line is a 5.0 Myr FRANEC-Padova isochrone at $DM=13.0$ mag, blue line is the same but shifted vertically by 0.75 mag. . . . .	25
3.1	The location of Wd 1 NACO FOV on composite colour $JHK_S$ image of Wd 1. . . . .	31
3.2	The error in stellar position in $l$ (left) and $b$ (right) derived with DAOPHOT by comparing two halves of the full data set. . . . .	32
3.3	The photometric error of stars in Wd 1 as a function of magnitude in the $K_S$ (left) and $H$ (right) bands. Each error value is averaged within 1 magnitude. . . . .	33
3.4	Proper motion of the stars in Wd 1 reference frame in Galactic coordinates. Cluster members are marked by red. . . . .	34

**LIST OF FIGURES**

---

3.5	Observable proper motion for stars along the line of sight towards Wd 1 vs. distance from the Sun. . . . .	35
3.6	Histograms of number of stars vs. proper motion components in galactic longitude $l$ (top) and galactic latitude $b$ (below). Histograms are fitted by two-component Gaussians (blue), where one component represents the distribution of the field stars (green), the other the distribution of the cluster members (purple). These plots are made for the magnitude intervals $13 < K_S < 15$ mag (74 stars, left) and $14 < K_S < 16$ mag (88 stars, right). . . . .	37
3.7	Histogram of the membership probabilities $P$ . . . . .	38
3.8	The observed proper motion dispersion in $l$ (left) and $b$ (right) as a function of stellar magnitude. . . . .	38
3.9	<i>Left</i> : CMD of the cluster (including field contamination). <i>Center</i> : CMD for the stars with cluster membership probability $P < 90\%$ . <i>Right</i> : CMD for the stars with $P \geq 90\%$ . . . . .	39
3.10	CMD for the cluster members of Wd 1. Red line is a 5.0 Myr FRANEC-Padova isochrone at $DM=13.0$ mag. Error bars (blue) indicate the typical errors in color and magnitude. . . . .	40
3.11	Average completeness as a function of magnitude for $K_S$ (left) and $H$ (right) bands. The best fitted Fermi-functions are overplotted. . . . .	41
3.12	NACO $K_S$ 2003 image of Wd 1 with superimposed $K_S$ 50% completeness contours. The labels correspond to the $K_S$ magnitudes for which completeness is 50% along the contours. . . . .	42
3.13	<i>Left</i> : IMF for the central region of Wd 1. The dashed line gives completeness-corrected IMF. The 50% completeness limit is indicated by a vertical dotted line. Blue line corresponds to a fitted IMF slope. <i>Right</i> : Cumulative IMF for stars with masses between $0.6$ and $18.0 M_\odot$ . Overplotted are cumulative functions as expected from power laws with slopes $\Gamma = -0.1$ (green) and $\Gamma = -0.5$ (red). . . . .	43
3.14	Composite colour $JHK_S$ image of Wd 1. Overplotted green annuli define the areas of Wd 1 that were analysed by Brandner et al. (2008). Red annulus shows the region of Wd 1 that was analysed at this work. Red star defines the cluster center. . . . .	44
3.15	Mass functions of Wd 1 for 4 annuli found by Brandner et al. (2008) from NTT/SOFI observations. The mass determination is based on a 3.9 Myr isochrone with $Z=0.020$ for stars with masses $\geq 6.0 M_\odot$ , and on a 3.2 Myr Palla Stahler isochrone with $Z=0.019$ for stars with masses $< 6.0 M_\odot$ . The slope of the mass function (dash-dotted line is computed from stars with masses between $3.4$ and $27 M_\odot$ .) . . . . .	45

## LIST OF FIGURES

---

4.1	The VLTI at Paranal. Future location of the GRAVITY beam combiner is marked by a green star. . . . .	48
4.2	Principle of dual-feed interferometry. Image credit: <a href="#">Delplancke (2008)</a> . . .	49
4.3	GRAVITY overview. Only two of 4 telescopes are shown. . . . .	50
4.4	H+K-band NIR wavefront sensor that will be installed on all four 8-m UTs. Image credit: A.Huber and R.Rohloff. . . . .	51
4.5	Beam combination principle, 6-baseline integrated optics beam combiner for the 4-telescopes. . . . .	52
4.6	Number of exoplanets (in percentage) detected via different methods. . . .	54
4.7	Displacement of the star due to a planet. . . . .	55
4.8	GRAVITY astrometric capabilities as compared to radial velocities measurements by HARPS and SPHERE direct imaging. Blue zone corresponds to GRAVITY exoplanet detection capabilities around M7.5 dwarf star at a distance of 6 parsec. . . . .	56
4.9	AstraLux Large M-dwarf multiplicity survey. Courtesy of W.Brandner. . .	59
4.10	Histogram of the mass distribution of the M dwarf GRAVITY potential targets. . . . .	61

# List of Tables

1.1	The most massive galactic clusters. . . . .	6
4.1	Planet-hunting astrometric missions . . . . .	57
4.2	M-dwarf targets . . . . .	60
4.3	Binary stars with known exoplanets . . . . .	62
4.4	Targets from the AstraLux M-dwarf multiplicity survey suitable for observations with GRAVITY . . . . .	63

## LIST OF TABLES

---

# 1

## Introduction

Astrometry is the branch of astronomy that focuses on precise measurements of the positions and movements of stars and other celestial bodies, as well as explaining these movements. The aim of this thesis is to show how powerful this method is today in applications ranging from studies of exoplanets to starburst clusters.

### 1.1 The first steps in astrometry

Planets in the solar system were already discovered in ancient times as objects changing their positions from night to night and week to week relative to the fixed sphere of stars. In approximately 3<sup>rd</sup> century BC Greek astronomers Timocharis of Alexandria and Aristillus created the first star catalogue, that was completed by a Greek astronomer Hipparchus around 150 BC. Hipparchus made his measurements with 1° accuracy using an armillary sphere and obtained the positions of at least 850 stars. Until late 16<sup>th</sup> century the progress was slight. At 1586 the Danish astronomer Tycho Brahe achieved a revolution in astrometric precision, by fixing stellar and planetary positions to about 60'' accuracy. He improved and enlarged existing instruments, and devised the most precise instruments available before the invention of the telescope. The progress in achievable astrometric accuracy, starting from the time of Tycho Brahe, is shown in Fig. 1.1. By the 20<sup>th</sup> century with the progress in meridian circles and the new photographic technique an accuracy of a tenth of a second of arc became possible. A large improvement has been made in the second half of the 20<sup>th</sup> century due to the photoelectric techniques and automatic control of micrometer and telescope. However, the atmospheric turbulence made the further progress difficult.

## 1. INTRODUCTION

---

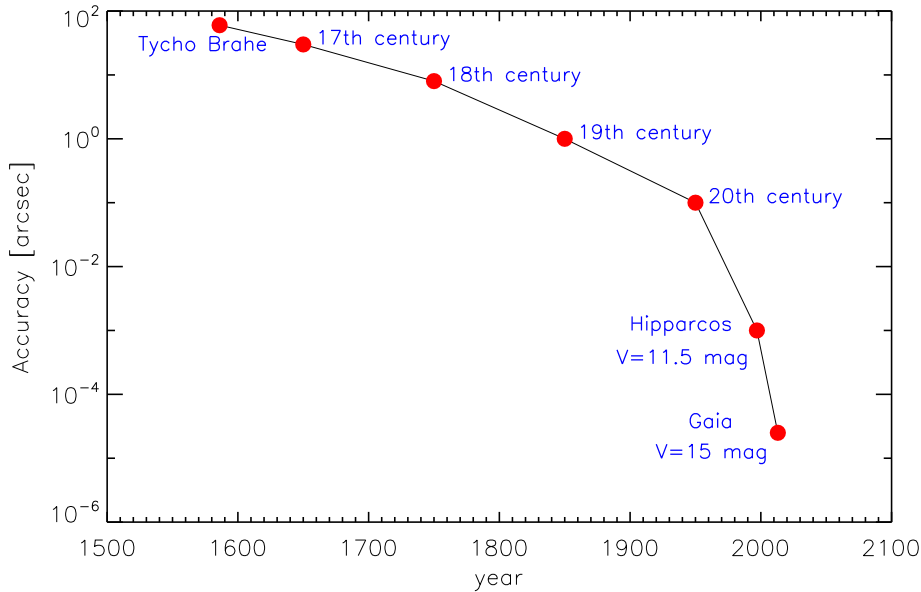


**Figure 1.1:** The development of astrometric accuracy with time, starting from Tycho Brahe.

### 1.2 Hipparcos

The powerful way to overcome the effect of atmospheric blurring is with space-based telescopes. In 1989 the Hipparcos satellite (HIgh Precision PARallax COLlecting Satellite), the first satellite specifically designed for astrometry, was launched. During 3.5 years of observations, from 1989 to 1993, the positions, parallaxes and proper motions of 118 000 stars with magnitudes down to  $V = 12.5$  mag were obtained with one milliarcsecond accuracy and published in 1997 in the Hipparcos Catalogue. An auxiliary star mapper onboard the satellite pinpointed more than one million of stars down to  $V = 11.5$  mag with 25 mas accuracy. This part of the mission was called Tycho. The Tycho-2 Catalogue with more than 2.5 million stars of magnitudes down to  $V = 11$  mag was published in 2000 and has a median error of proper motions 2.5 mas/year. The Hipparcos data provided the distance measurements for more than 400 nearby stars with 1% precision and for 7000 stars with 5% precision. This dramatically improved our knowledge of stellar dynamics and evolution, the cosmic distance scale and the universe's size. In total, the Hipparcos satellite gave a jump in astrometric accuracy by a factor of 100 with respect to the most accurate at that time ground-based catalogue FK5.

### 1.3 GAIA

The next jump in accuracy is expected with the launch of GAIA (Global Astrometric Interferometer for Astrophysics) in 2013. GAIA is an ESA space mission that promises to bring a factor 50 to 100 in positional accuracy and a factor of 10 000 in the number of stars, compared to Hipparcos. This will become possible due to the combination of many factors, the most important being bigger and more efficient detectors, and bigger optics. During its 5 year mission, GAIA will measure the positions of around one billion stars with magnitudes down to  $V = 20$  mag, observing each target 70 times on average. The positions, distances and proper motions will be determined with an accuracy of  $24 \mu\text{as}$  at  $V = 15$  mag and  $200 \mu\text{as}$  at  $V = 20$  mag. GAIA will have its own precision reference frame and as a result will provide absolute astrometric solutions. GAIA will perform a homogeneous whole sky survey and will produce a 3D map of 1 billion stars in the magnitude range between 6 and 20.

### 1.4 Adaptive Optics

The progress of astrometry from the ground came with the invention of Adaptive Optics (AO), a technology that made possible to counteract the atmospheric turbulence and to reduce the effects of the wavefront distortions in real time. The American astronomer Horace Babcock in 1953 was the first to propose the idea of AO, but due to technical reasons it did not come into common usage until the 1990s. The AO working principle is shown in Fig. 1.2. A plane wavefront from a celestial object is corrugated in phase and amplitude by the turbulence in the atmosphere. The shape of this distorted wavefront is independently measured by a wavefront sensor and an appropriate correction is calculated. This is used to change the shape of the deformable mirror and to correct for the atmospheric defocusing and higher order aberrations. These corrections should be applied every few milliarcseconds to keep up with the change of the turbulence. Exploitation of this new capability has led to diffraction-limited image quality at near-infrared wavelength and astrometric accuracies of  $100 \mu\text{as}$  (Cameron et al., 2009).

NAOS/CONICA (NACO) is the AO system and near-infrared camera at the ESO VLT unit telescope. The system was installed in 2002 and was the first AO instrument to begin operations at the VLT. The instrument is capable of diffraction limited imaging, spectroscopy and coronagraphy in 1-5 micron wavelength regime. In chapter 2 and 3 of this thesis we use NACO data in order to study starburst clusters. Starburst clusters are the most massive ( $M \geq 10^4 M_{\odot}$ ) young clusters ( $< 30$  Myr) known in the Milky Way, that contain from ten thousand to a million of stars. The proper motion survey of starburst clusters in the Milky Way have initiated with NACO in 2008. The survey partially benefits

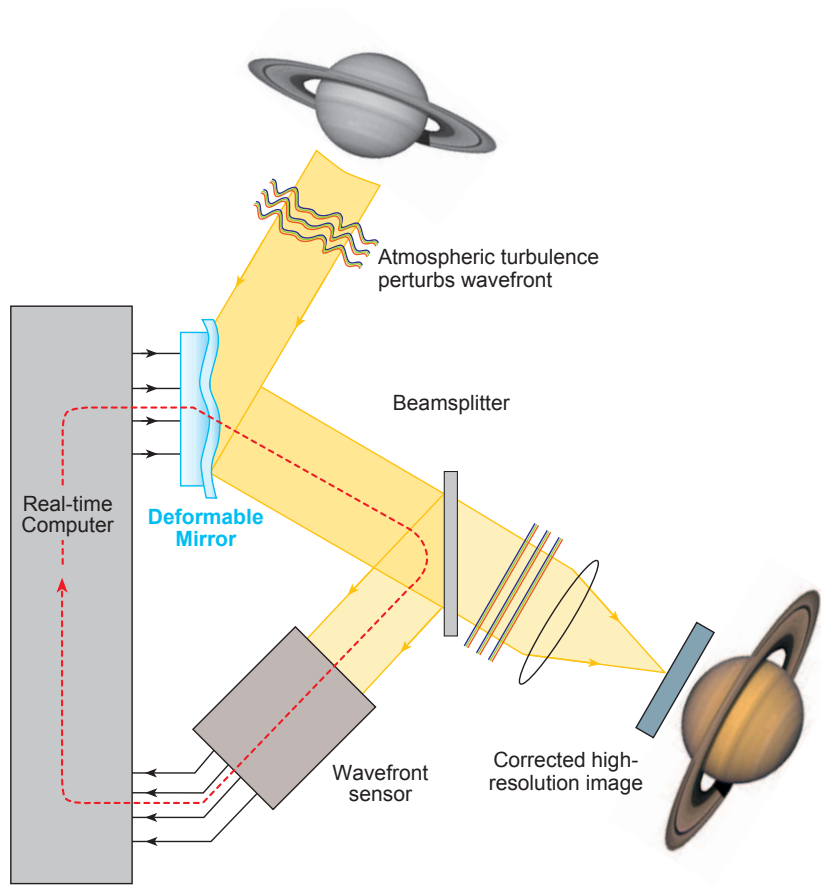


**Figure 1.2:** Adaptive optics working principle. Courtesy of S.Hippler.

from earlier observations in 2002/2003. NACO is currently the only instrument available providing high spatial resolution, near-infrared imaging with milliarcseconds astrometric accuracy at the VLT.

## 1.5 Astrometry of starburst clusters

The current knowledge of starburst clusters is highly incomplete beyond a few kiloparsec from the Sun due to interstellar extinction and crowding. Only about a dozen starburst clusters are known today in the Milky Way and so far they have been detected either in the spiral arms or in the Galactic Center region (see Fig. 1.3). Table 1.1 contains the information about the 8 most massive galactic clusters known today.  $L$  and  $B$  are galactic longitude and latitude and  $d$  is the distance to the cluster.

Arches, Quintuplet and Young Nuclear Cluster (YNC) are located in the Galactic Center region and provide an example of extreme star formation as observable in extragalactic

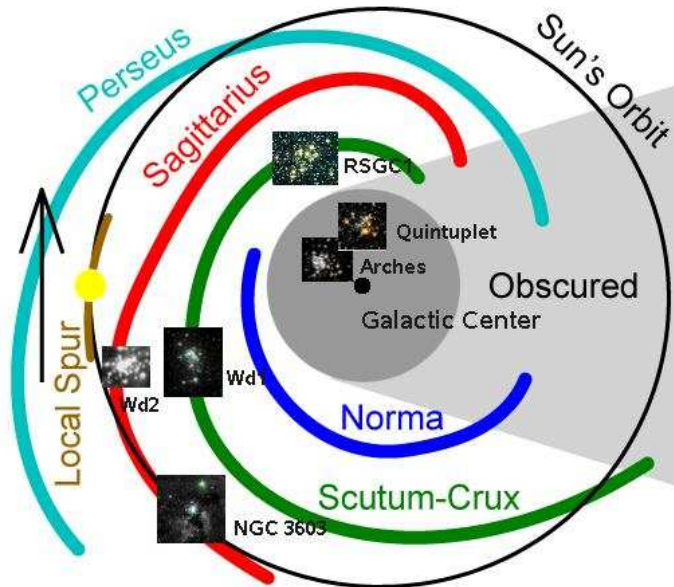


**Figure 1.3:** The schematic location of the starburst clusters in the Milky Way. The yellow dot indicates the Sun. Courtesy of A.Stolte.

cases. Scientists are still puzzled by how these clusters might have formed in the presence of strong tidal forces and magnetic field, high radiation and high temperature of the molecular clouds in the Galactic Center. Another interesting subject to study is whether they form in a similar mode as the spiral arm clusters. In chapter 2 of this thesis we combine high angular resolution AO measurements with Hubble Space Telescope observations to multi-epoch astrometric data sets. This is used to study the formation scenario of two spiral arm starburst clusters Westerlund 1 (Wd 1) and NGC 3603 YC. As an indicator of the overall duration of the star formation process in these clusters, we derived an upper limit on the age spread of each cluster's stellar population.

The mass and age of the starburst clusters make them ideal for studies of massive stellar evolution and dense stellar systems. Starburst clusters contain stars at all stages of evolution, from the pre-main sequence to main sequence, and post-main sequence, until the massive stars finally turn into a supernova. By observing such clusters we can examine the influence of high-mass star formation on the formation of low- and intermediate-mass stars. As some of the most massive stars in the Galaxy reside within such clusters, the UV radiation from them lead to rapid photo-evaporation of any remnant circumstellar material around the low-mass members of the cluster, which results in very little differential extinction and well-constrained color-magnitude diagrams for the cluster members.

The initial mass function (IMF) of the cluster can tell us more about the star formation process and the cluster's fate. The largest bias in the IMF comes from the contamina-

## 1. INTRODUCTION

---

**Table 1.1:** The most massive galactic clusters.

Name	L [deg]	B [deg]	d [kpc]	Age [Myr]	Mass [ $M_{\odot}$ ]	Reference
Westerlund 1	339.6	-0.4	4	4 – 5	$5 \cdot 10^4$	Gennaro et al. (2011)
RSGC2	26.2	0	5.8	14 – 20	$4 \cdot 10^4$	Davies et al. (2007)
RSGC1	25.3	-0.2	6.6	10 – 14	$3 \cdot 10^4$	Davies et al. (2008)
RSGC3	29.2	-0.2	6	18 – 24	$2 \cdot 10^4$	Alexander et al. (2009)
GC YNC	0	0	7.6	4 – 8	$1.5 \cdot 10^4$	Paumard et al. (2006)
NGC 3603 YC	291.6	-0.5	6	1 – 2.5	$1.3 \cdot 10^4$	Rochau et al. (2010)
Arches	0.1	0	8	$\sim 2$	$1.1 \cdot 10^4$	Clarkson et al. (2012)
Quintuplet	0.2	-0.1	8	3 – 5	$10^4$	Hußmann et al. (2011)

tion with field stars in the spiral arms and Galactic Center. The powerful tool for the discrimination between cluster members and field stars is the proper motion membership selection. In chapter 3 of this thesis we use 2 epochs of the VLT/NACO observations of the most massive starburst cluster Wd1 in order to construct an unbiased IMF of the cluster and to study its dynamical properties. High resolution AO observations allowed to resolve a big amount of stars in the cluster center and improve the statistics.

### 1.6 Long baseline astrometry

For ground-based observations at 8 m to 10 m class telescopes the single aperture astrometry even with the implementation of AO has the best possible astrometric accuracy of  $100\mu\text{as}$ . To overcome this limit, long-baseline interferometry was proposed by Shao and Colavita (1992) for a narrow-angle astrometry. The key features are dual-beam operation to perform a simultaneous differential measurement between a science object and a reference star, baselines more than 100 m to reduce atmospheric and photon-noise errors, laser metrology to control systematic errors and infrared observations with phase referencing to increase the sensitivity of a stellar interferometer. The latter can be done by simultaneously observing a bright reference star and the science target using two separate interferometric beam-combiners, and using the reference star to correct for the fringe motion introduced by the atmosphere. A significant advantage in finding reference star is given for a long-baseline interferometer operating at  $2.2\text{-}\mu\text{m}$  band. At this wavelength the isoplanatic patch of  $\sim 15\text{--}20''$  is much larger than at visible wavelengths of  $\sim 3\text{--}4''$ . Furthermore, operations in the near-infrared are scientifically more interesting for all types of obscured objects. The GRAVITY (General Relativity Analysis via VLT InTerferometrY) instrument for the VLTI (Eisenhauer et al., 2011) will exploit the technique of differential astrometry to achieve micro-arcsecond astrometric accuracy. It will combine near-infrared

## 1.6 Long baseline astrometry

---

light from all four 8.2 m Unit Telescopes or 1.8 m Auxiliary Telescopes of the VLTI, utilize 1.7" field of view to provide simultaneous interferometry of 2 objects and use AO at the telescope level and fringe tracking at the interferometer level. This will allow to perform relative astrometry at  $10 \mu\text{as}$  accuracy, the size of ten-cent coin on the Moon. How powerful GRAVITY will be in characterizing exoplanets is described in chapter 4 of this thesis.

The tremendous progress in astrometric accuracy has been achieved since the observations by Timocharis of Alexandria and Aristillus about 3<sup>rd</sup> century BC. Modern astrometric telescopes observe hundreds of thousands of stars a night, overcoming the problem of atmosphere. The progress in astrometry is vitally important for other fields of astronomy, like celestial mechanics, stellar dynamics and galactic astronomy.

## 1. INTRODUCTION

---

## 2

# Instantaneous starburst of the massive clusters Wd 1 and NGC 3603 YC

*We present a new method to determine the age spread of resolved stellar populations in a starburst cluster. The method relies on a two-step process. In the first step, kinematic members of the cluster are identified based on multi-epoch astrometric monitoring. In the second step, a Bayesian analysis is carried out, comparing the observed photometric sequence of cluster members with sets of theoretical isochrones. When applying this methodology to optical and near-infrared high-angular resolution Hubble Space Telescope (HST) and adaptive optics observations of the  $\sim 5$  Myr old starburst cluster Westerlund 1 and  $\sim 2$  Myr old starburst cluster NGC 3603 YC, we derive upper limits for the age spreads of 0.4 and 0.1 Myr, respectively. The results strongly suggest that star formation in these starburst clusters happened almost instantaneously. <sup>a</sup>.*

---

<sup>a</sup>A version of this chapter has been published in the *Astrophysical Journal Letters*, Volume 750, Issue 2 (2012) ([Kudryavtseva et al., 2012](#))

### 2.1 Introduction

Our understanding of star formation, in particular for high-mass stars, has progressed considerably in recent years (e.g., [Commerçon et al. 2011](#); [Krumholz et al. 2009](#); [Kuiper et al. 2011](#)), though the exact sequence of the formation of individual stars during a star formation event is not yet entirely understood. In particular, it is still unknown if low-mass stars tend to form later than high-mass stars (e.g., [Klessen 2001](#)), or if high-mass stars form last, resulting in a rapid termination of star formation (e.g., [Zinnecker and Yorke 2007](#)).

The age spread of a cluster’s stellar population is a good indicator of the overall duration of the star formation process in the cluster. Studies of star-forming regions have reported different results: from a single age, as in NGC 4103 ([Forbes, 1996](#)) to age spreads of 2 to 4 Myr, e.g., in LH95 ([Da Rio et al., 2010](#)), the Orion Nebula Cluster ([Reggiani et al., 2011](#)), W3 Main ([Bik et al., 2012](#)), and even larger age spreads of tens of Myr, like in the Pleiades star cluster ([Belikov et al., 1998](#)). In case of the Pleiades cluster, very old stars might be field stars that were captured by a giant molecular cloud (GMC) during its life time prior to star formation ([Bhatt, 1989](#)). The broad range of age spreads might indicate the existence of different star formation scenarios for different star-forming environments. At the same time, discrepant results on the age spread in individual regions indicate that both observational and theoretical (e.g., [Naylor 2009](#)) biases and the overall methodology used to assign ages to individual stars, might also be of importance. Observational difficulties include small number statistics, contamination of samples by field stars, variable extinction and intrinsic infrared excess, unresolved binaries, problems in determining effective temperatures and luminosities and insufficient characterization of photometric uncertainties originating in varying degrees of crowding.

We present a new method, which takes into account these effects in order to derive an accurate age spread of the stellar population of clusters. As a first step, we assign cluster membership to individual stars based on kinematics derived from multi-epoch astrometric observations. The second step is to use a Bayesian method to determine the probability distribution for the age of each member star, given its photometric properties. From this we determine the age spread for each of the clusters.

For our analysis, we have selected Westerlund 1 (Wd 1) and NGC 3603 YC, two of the most populous and massive Galactic starburst clusters (e.g., [Clark et al. 2005](#); [Melena et al. 2008](#)). The clusters have half-mass radii of  $\approx 1$  and 0.5 pc, respectively. They are composed of more than 10,000 stars each, a large fraction of which can be resolved individually via ground-based adaptive optics and HST observations from space. It is still unclear how such compact clusters have been formed and on which time-scales. For NGC 3603 YC, [Stolte et al. \(2004\)](#) suggest a single age of 1 Myr from isochrone fitting to the pre-main sequence (PMS) transition region and a single burst of star formation, while

Beccari et al. (2010) report a 10 Myr age spread for the PMS population, and therefore two distinct episodes of star formation. Brandner et al. (1997) also state that the simultaneous presence of early O-stars and blue supergiants (BSGs) in NGC 3603 YC might hint at two star formation events separated by 10 Myr. At the same time a ring nebula and bipolar outflows associated with BSG Sher 25 are remarkably similar to the triple-ring nebula around Supernova 1987A that was formed as a result of a binary evolution (Morris and Podsiadlowski, 2009). In case Sher 25 is the result of binary interaction, one cannot use single star evolutionary tracks to estimate its age.

For Wd 1 recent studies give an age in the range 3 to 6 Myr (Brandner et al., 2008; Gennaro et al., 2011; Negueruela et al., 2010), and an age spread of less than 1 Myr (Negueruela et al., 2010). The latter is based on spectral classification of Wd 1’s OB supergiant population.

## 2.2 Method

The first step of our method is a proper motion selection (e.g., Bedin et al. 2001) of cluster members on the basis of multi-epoch astrometric observations. This enabled us to reject the majority of the contaminating field stars. Next, we apply Bayesian analysis to the photometry of cluster members with respect to theoretical isochrones to determine the probability distribution for the age of each member star, given its photometric properties (e.g., Da Rio et al. 2010). We modified the Bayesian method of Jørgensen and Lindegren (2005) both by taking into account the cluster membership probability and by adjusting the mass function (MF) by a completeness factor. The posterior probability of the  $i$ -th star with magnitudes, e.g.,  $J_i, K_{S_i}$  to belong to the isochrone of age  $t$  is:

$$p(t|J_i, K_{S_i}) = \int_{box} p(J_i, K_{S_i}|M, t) \cdot \xi(M|\alpha, t) dM, \quad (2.1)$$

where  $M$  is the initial stellar mass,  $\xi(M|\alpha, t)$  is the stellar MF with a slope  $\alpha$ . The integration region is a "box", i.e. a rectangular area in color-magnitude (CM) space:  $K_{S_{min}} < K_S < K_{S_{max}}, (J - K_S)_{min} < (J - K_S) < (J - K_S)_{max}$ . The limits of this area define a mass range which is considered during integration. This box has been chosen in order to exclude fore- and background field star contaminants based on their too blue or too red colors relative to the cluster sequence. To account for residual field star contamination, the first multiplier inside the integral is defined as:

$$p(J_i, K_{S_i}|M, t) = P_{good} \cdot p(J_i, K_{S_i}|M, t, cluster) + (1 - P_{good}) \cdot p(J_i, K_{S_i}|field), \quad (2.2)$$

where  $P_{good}$  is the probability of a star to be a cluster member,  $(1 - P_{good})$  is the probability to be a field star.

## 2. INSTANTANEOUS STARBURST OF THE MASSIVE CLUSTERS WD 1 AND NGC 3603 YC

---

From the normalization conditions

$$\int_{box} p(J_i, K_{S_i} | M, t, cluster) dJ dK_S = 1, \quad (2.3)$$

$$\int_{box} p(J_i, K_{S_i} | field) dJ dK_S = 1 \quad (2.4)$$

we derive the probability that a cluster member or field star is found in a given position on the color-magnitude diagram (CMD) as:

$$p(J_i, K_{S_i} | M, t, cluster) = \frac{1}{2\pi\sigma_{J_i}\sigma_{K_{S_i}}} \times e^{-\frac{1}{2}\left[\left(\frac{J(M,t)-J_i}{\sigma_{J_i}}\right)^2 + \left(\frac{K_S(M,t)-K_{S_i}}{\sigma_{K_{S_i}}}\right)^2\right]}, \quad (2.5)$$

$$p(J_i, K_{S_i} | field) = \frac{1}{\Delta(K_S)\Delta(J - K_S)}, \quad (2.6)$$

where  $\sigma_{J_i}, \sigma_{K_{S_i}}$  are the photometric uncertainties of star  $i$ ,  $J(M, t), K_S(M, t)$  are the magnitudes of the theoretical isochrone,  $\Delta(K_S) = K_{S_{max}} - K_{S_{min}}$ ,  $\Delta(J - K_S) = (J - K_S)_{max} - (J - K_S)_{min}$ . The MF  $\xi(M|\alpha, t)$  was modified by  $compl(M|t)$  to include source incompleteness and has the following form:

$$\xi(M|\alpha, t) = B \cdot M^{-\alpha} \cdot compl(M|t) \quad (2.7)$$

where B was derived from the normalization condition

$$\int_{box} \xi(M|\alpha, t) dM = 1 \quad (2.8)$$

and  $compl(M|t)$  from completeness simulations (see Sect. 2.3.2).

By multiplying the individual age distributions, we obtain the global probability function for the cluster, as a whole, to have an age  $t$ :

$$L(t) = \prod_i p(t|J_i, K_{S_i}). \quad (2.9)$$

## 2.3 Observations and data reduction

### 2.3.1 Observations of Wd 1 and NGC 3603 YC

Near-infrared adaptive optics observations of the central region of Wd 1 were carried out in 2003 April, using NACO at the VLT (Fig. 2.1a).  $K_S$  observations with a plate scale

---

## 2.3 Observations and data reduction

of 27 mas/pixel and a field of view (FOV) of  $27'' \times 27''$  (corresponding to  $0.5\text{pc} \times 0.5\text{pc}$  at 4.0 kpc distance (Gennaro et al., 2011)) were centered on  $RA(2000) = 16h47m06.5s$ ,  $Dec(2000) = -45^\circ 51' 00''$ .  $K_S$  frames with integration times of 1 min were coadded, resulting in a total integration time of 5 min.

In 2010 August (epoch difference 7.3 yr), Wd1 was observed with the HST Wide Field Camera 3 (WFC3/IR) in the F125W band with a plate scale of 130 mas/pixel (Fig. 2.1b). The final image consists of 7 individual exposures with small ( $< 10''$ ) offsets to compensate for bad pixels, with a total integration time of 2444 s. The overlapping FOV with NACO is  $\approx 18'' \times 24''$  (corresponding to  $0.35\text{pc} \times 0.47\text{pc}$  at 4.0 kpc distance (Gennaro et al., 2011)). For a detailed description of the full data set and data reduction, we refer to the work of M. Andersen et al. (2012, in prep.).

Positions and magnitudes of the stars were determined using the IRAF implementation for the stellar photometry in crowded fields DAOPHOT (Stetson, 1987). Instrumental magnitudes were calibrated against 2MASS, using suitable stars identified on the NTT/SOFI data from the work by Gennaro et al. (2011) as secondary photometric standards. To align the two data sets, identical bright stars with a high probability of being cluster members were identified. For the initial matching between NACO and WFC3 coordinates, a linear transformation, scaling and rotation was computed based on the  $x, y$  positions of two stars. This gave a first order estimate of the NACO coordinates of all stars (with  $12.5 < m_{K_S} < 16.0$  mag) in the WFC3 coordinate system. The root mean square (RMS) between the translated NACO coordinates and the positions of the corresponding stars in the WFC3 system is 0.17 WFC3/IR pixel (or 21.8 mas). As a second step a higher order matching, namely a geometric transformation based on fitting 3rd order polynomials with cross-terms in  $x$  and  $y$ , was done. This reduced the RMS to 0.036 WFC3/IR pixel (or 4.6 mas), which over a time span of 7.3 years corresponds to  $\approx 0.6$  mas/yr.

Images of NGC 3603 YC were taken with HST's Wide-Field Planetary Camera 2 (WFPC2) with an image scale of 45.5 mas/pixel (Fig. 2.1c,d). The first epoch observations in the filters F547M and F814W were separated by 10.15 yr from the second epoch observations in F555W and F814W filters. The common FOV for 2 epochs of observations is a circle with a diameter of  $30''$ . The analysis was carried out for the core ( $< 0.5\text{pc}$ ) of NGC 3603 YC. The details of the data reduction process have already been described by Rochau et al. (2010).

### 2.3.2 Completeness correction

Completeness simulations for the Wd1 data set in J band (F125W) were done for the magnitude range  $m_J$  from 14.0 to 23.0 mag. For each simulation, 25 artificial stars were added at random positions in the image, the image was then analyzed using DAOPHOT, and the position and magnitude of the recovered stars recorded. This procedure was re-

## 2. INSTANTANEOUS STARBURST OF THE MASSIVE CLUSTERS WD 1 AND NGC 3603 YC

---

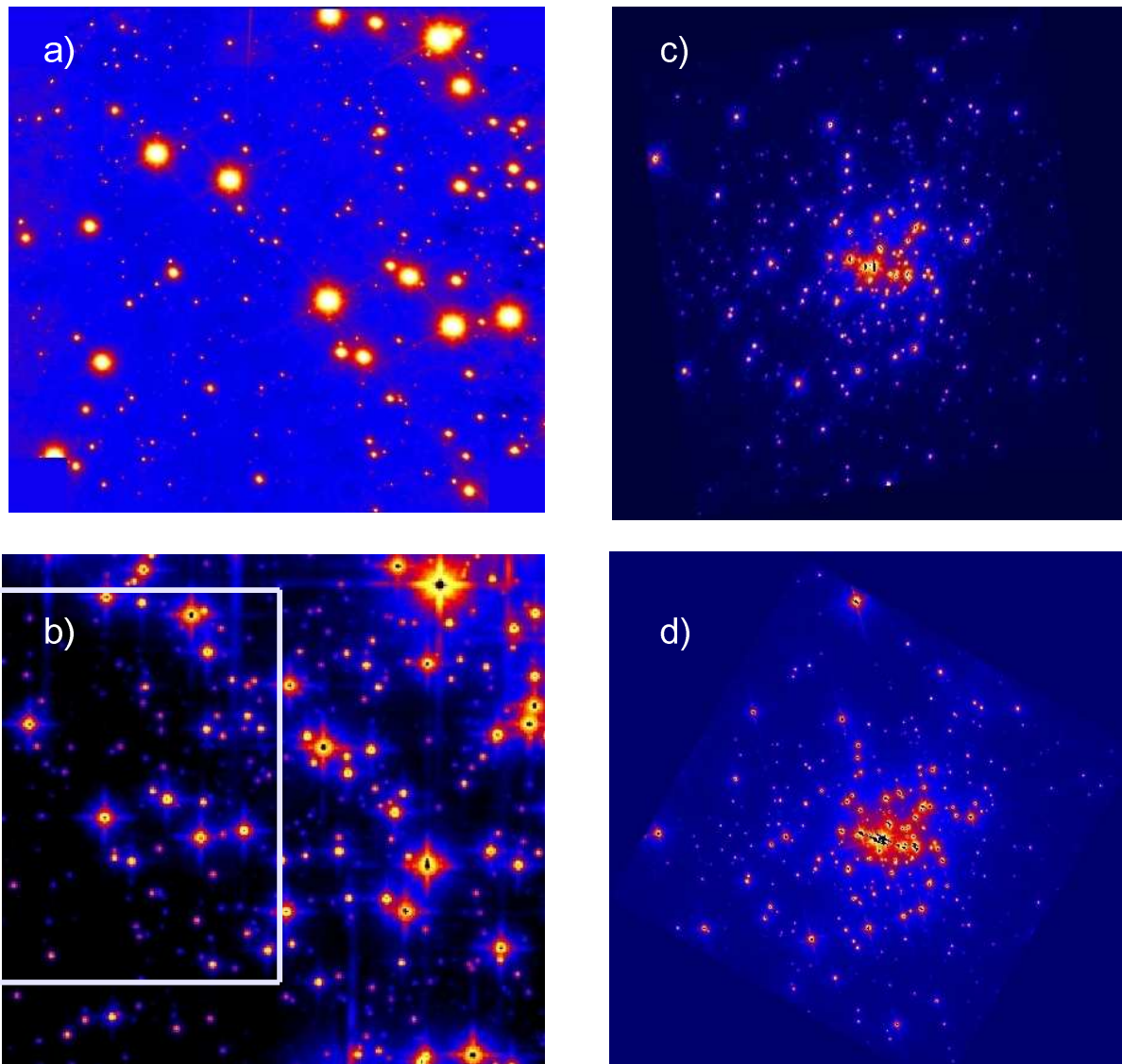


**Figure 2.1:** (a): VLT/NACO 2003 image of Wd1 in  $K_S$ -band. (b): HST/WFC3 2010 image of Wd1 in F125W filter. The overlapping FOV with NACO is enclosed by a white box. (c): HST/WFPC2 2007 image of NGC 3603 YC in F814W filter. (d): HST/WFPC2 2007 image of NGC 3603 YC in F555W filter.

peated 1600 times, i.e. encompassing 40,000 artificial stars in total. The recovery fractions were determined following the steps outlined by [Gennaro et al. \(2011\)](#). We calculated the average completeness for the WFC3/IR area overlapping with the NACO frame as a function of  $m_J$  and fitted this by a Fermi function  $C_J(M|t) = \frac{A_0}{e^{\frac{m_J(M,t)-A_1}{A_2}} + 1}$  (Fig. 2.2a). In case of NACO/VLT image 5 stars were added at each of 100 runs, in total 500 stars

## 2.3 Observations and data reduction

for each  $m_{K_S}$  magnitude bin between 12.0 and 21.0 mag. The average completeness as a function of  $m_{K_S}$  was calculated and fitted by a Fermi function  $C_{K_S}(M|t) = \frac{B_0}{e^{\frac{m_{K_S}(M,t)-B_1}{B_2}} + 1}$  (Fig. 2.2b). As the detections of a star in each band are independent, the total incompleteness correction is a product of two corrections:  $compl(M|t) = C_J(M|t) \times C_{K_S}(M|t)$ .

Completeness simulations for NGC 3603 YC were done for the magnitude range from 14.0 to 23.0 mag in both F555W and F814W bands. Ten artificial stars were added at each of 50 runs, in total 500 stars for each magnitude bin. The average completenesses for the HST/WFPC2 images and the fitted to them Fermi functions  $C_{F555W}(M|t)$ ,  $C_{F814W}(M|t)$  are presented on Fig. 2.2(c,d). The total incompleteness correction for NGC 3603 YC was defined as  $compl(M|t) = C_{F555W}(M|t) \times C_{F814W}(M|t)$ .

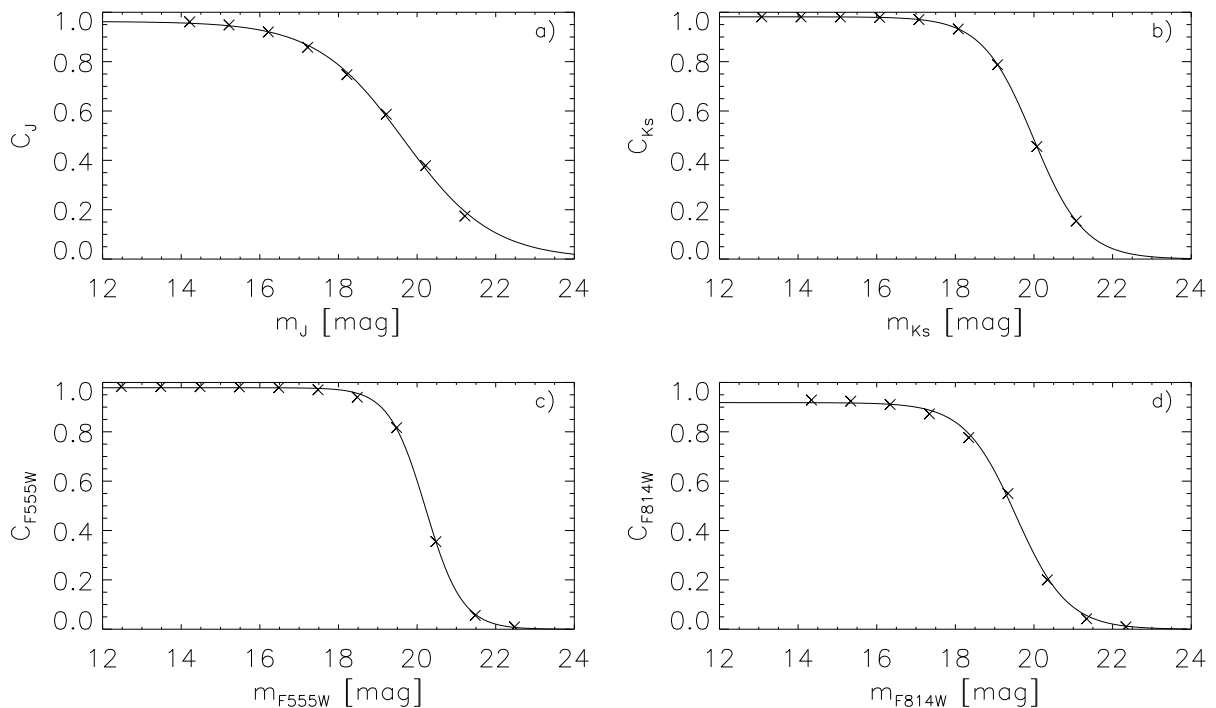


**Figure 2.2:** Average completeness for the WFC3/IR area overlapping with the NACO frame as a function of  $m_{F125W}$  (a), for the NACO/VLT frame as a function of  $m_{K_S}$  (b), for HST/WFPC2 images as functions of  $m_{F555W}$  (c) and  $m_{F814W}$  (d). Overplotted are Fermi-functions fitted to the data.

## 2. INSTANTANEOUS STARBURST OF THE MASSIVE CLUSTERS WD 1 AND NGC 3603 YC

---

### 2.3.3 Proper motion selection

The main contaminants apparent in CMDs of the starburst clusters are dwarf stars in the foreground and giants in the background. Due to galactic rotation, their proper motion is different from that of cluster stars. Velocity dispersions of disk and halo stars are  $\approx 50$  km/s to 150 km/s (Navarro et al., 2011).

For Wd 1 (see Fig. 2.3) our selection criterion for the astrometric residual of 5.8 mas corresponds to a proper motion of 0.8 mas/yr in the cluster rest frame (or 15.2 km/s at a distance of 4.0 kpc), which is higher than Wd 1’s internal velocity dispersion of 2.1 km/s (Cottaar et al., 2012). In a histogram of number of stars vs. absolute value of proper motion our criterion of 0.8 mas/year corresponds to a standard deviation of  $1\sigma$  of a Gaussian function fitted to the histogram. The histograms for the proper motions in RA and DEC and fitted to them Gaussian functions are shown in Fig. 2.4. As you can see from Fig. 2.6a, our selection provides an effective discriminant between cluster members and field stars.

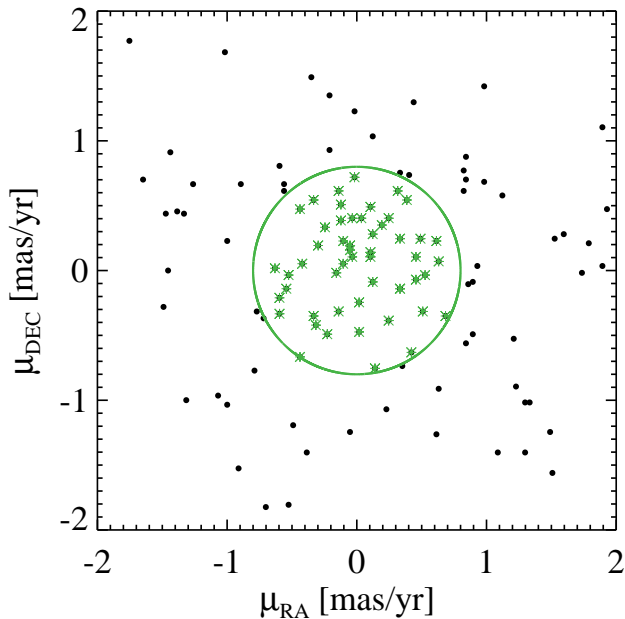


**Figure 2.3:** Proper motion diagram for Wd1. Stars with proper motions less than 0.8 mas/year are marked by green asterisks.

For NGC 3603 YC, we used the result of Rochau et al. (2010), which is based on proper motions over an epoch difference of 10.15 years. The authors calculated cluster membership probabilities ( $P_{mem}$ ) as described by Jones and Walker (1988), and considered the

## 2.3 Observations and data reduction

stars with  $P_{mem} > 90\%$  as cluster members. The histogram of number of stars vs. cluster membership probability  $P_{mem}$  is shown in Fig. 2.5

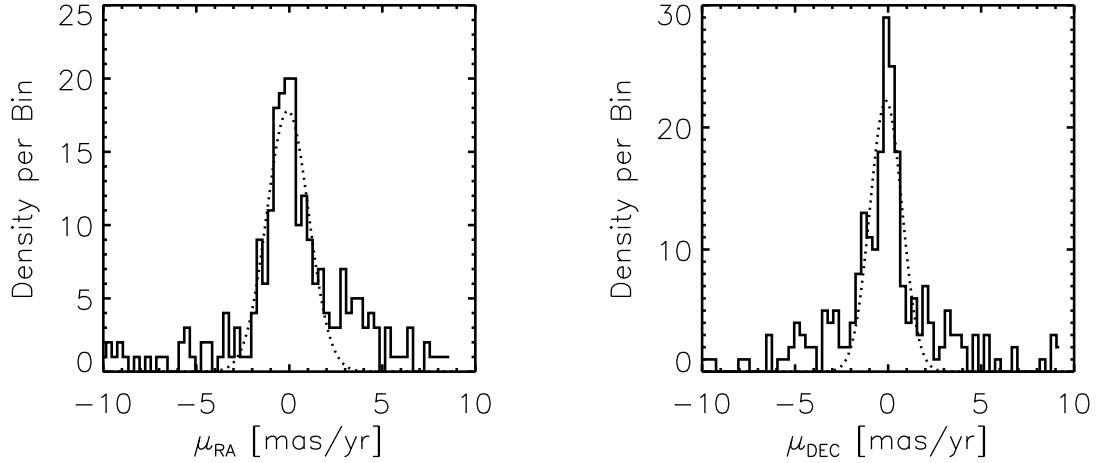


**Figure 2.4:** Histograms of number of stars vs. proper motion in RA and DEC for Wd1. Bin size is 0.3 mas/year. Dotted line is a Gaussian function fitted to the histogram.

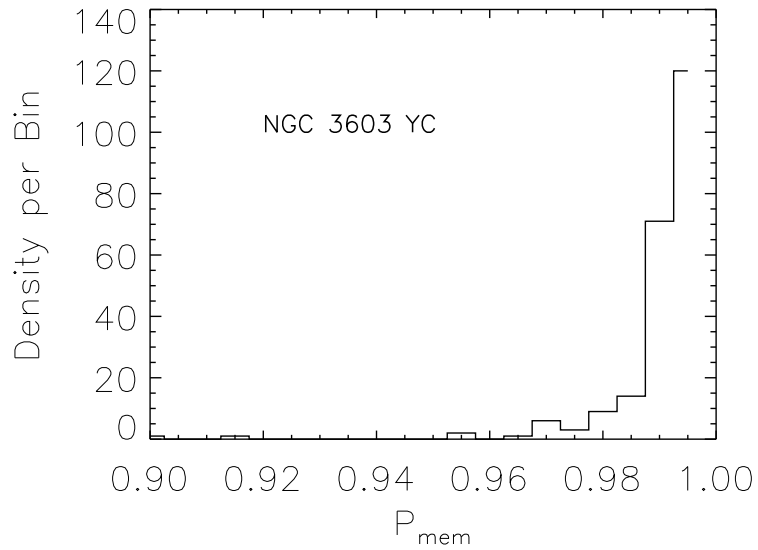


**Figure 2.5:** Histogram of number of stars vs. cluster membership probability  $P_{mem}$  for NGC 3603 YC. Bin size is 0.005.

## 2. INSTANTANEOUS STARBURST OF THE MASSIVE CLUSTERS WD 1 AND NGC 3603 YC

---

### 2.4 CMD for Wd 1 and NGC 3603 YC

The CMD for Wd 1 is presented in Fig. 2.6a. For our further analysis we consider only the region with  $12.5 < m_{K_S} < 17.0$  mag and  $1.2 < m_J - m_{K_S} < 2.9$  mag (red box in Fig. 2.6), which comprises 41 stars with masses in the range from 0.5 to  $11.5 M_{\odot}$ . Brighter stars were excluded because of saturation, fainter stars because of lower signal-to-noise ratio and hence larger photometric and astrometric uncertainties. The sample includes main sequence (MS), Pre-MS, and transition region stars, which have terminated their fully-convective Hayashi phase and are rapidly moving towards the MS. The CMD for NGC 3603 YC (Fig. 2.6b) is derived from 2nd epoch observations in F555W and F814W. For the age spread determination we selected the region with  $16.5 < m_{F555W} < 21.5$  mag,  $1.4 < m_{F555W} - m_{F814W} < 3.3$  mag (red box), which comprises 228 stars with masses from 0.8 to  $6.5 M_{\odot}$ . Overplotted is the best fitting isochrone assuming a particular distance, for a solar metallicity  $Z=0.015$ , calculated from the latest version of FRANEC evolutionary models<sup>1</sup> (Tognelli et al., 2011), adopting a mixing length value of  $ML = 1.68$ . We supplement the FRANEC models with Padova models (Marigo et al., 2008) for masses  $M > 7 M_{\odot}$ . The FRANEC models have been transformed into the observational plane using spectra from ATLAS9 model atmospheres (Castelli and Kurucz, 2004). For the analysis, we used isochrones with 0.1 Myr spacing, covering an age range from 0.5 to 6 Myr.

### 2.5 Age likelihood for Wd 1 and NGC 3603 YC

The application of our method (Sect. 2.2) to Wd 1 and NGC 3603 YC reveals a degeneracy between the cluster's distance and age. To take it into account we present our result in form of two-dimensional (2d) maps  $\log(L(t, DM))$ , where  $DM$  is the distance modulus. Since all cluster members should be at virtually the same distance, we can make a cut of this map at a particular value of  $DM$  and then analyse the resulting cluster age and age spread at such distance.

In order to evaluate  $P_{good}$  in Eq.(2.2) for Wd 1 we estimated the density of stars in the CMD regions adjacent to the red box (Fig. 2.6,  $m_J - m_{K_S} > 2.9$  mag,  $m_J - m_{K_S} < 1.2$  mag), where the stars are apparently non-cluster members. The extinction value of  $A_{K_S} = 1.1$  mag (Brandner et al., 2008) was assumed to be the same for all cluster members. The extinction law was taken from Rieke and Lebofsky (1985). For the MF slope in Eq.(2.7) we assumed  $\alpha = 1.42$ , as we derived from near-infrared adaptive optics observations of the central region of Wd 1.

---

<sup>1</sup>FRANEC models in a wide range of masses and ages, for several chemical compositions and mixing length parameter, are available at <http://astro.df.unipi.it/stellar-models/>

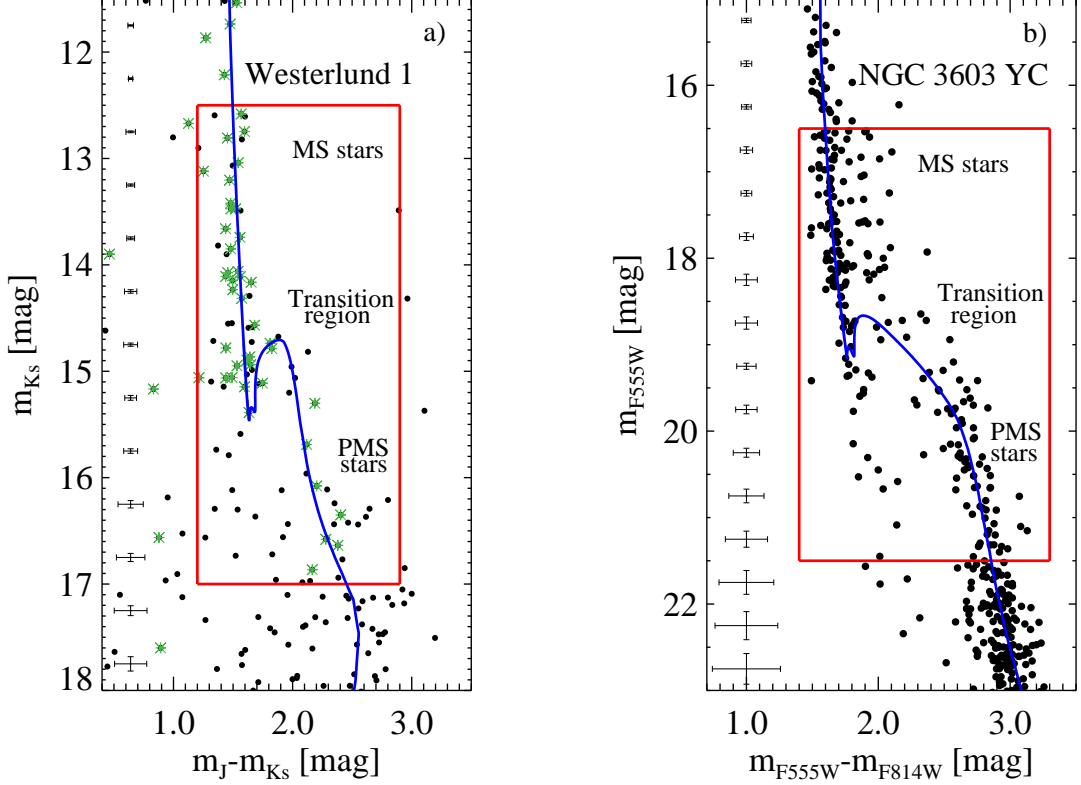


**Figure 2.6:** Color-magnitude diagrams of Wd 1 (a) and NGC 3603 YC (b). Error bars indicate typical errors in color and magnitude. Red boxes show the regions that were taken for the analysis of the age spread. Proper motion selected stars for Wd 1 are marked by green asterisks. The CMD of NGC 3603 YC includes only stars with cluster membership probabilities more than 90%. FRANEC-Padova isochrones (blue) are overplotted. For Wd 1 this is a 5.0 Myr isochrone at  $DM=13.0$  mag, for NGC 3603 YC a 2.0 Myr isochrone at  $DM=14.1$  mag.

In order to quantify the photometric error  $\sigma$  in Eq.(2.5), we used the results of the artificial star experiments to compare the known input magnitudes with output magnitudes recovered by DAOPHOT. A more detailed explanation of the procedure is described in [Gennaro et al. \(2011\)](#). The maximum photometric errors we got for Wd 1 are 0.05 mag in  $K_S$  and 0.18 mag in J down to limiting magnitudes of  $m_{K_S} = 17$  mag and  $m_J = 19$  mag. Additional source of photometric uncertainty comes from the variable extinction across the FOV due to a variation in the density of remnant molecular material along the line of sight. In case of Wd 1 data our FOV is relatively small and the errors in magnitudes are mainly caused by uncertainties in the photometric zero point determination by converting instrumental to apparent magnitudes or e.g by the bright stars, whose PSF wings affect

## 2. INSTANTANEOUS STARBURST OF THE MASSIVE CLUSTERS WD 1 AND NGC 3603 YC

---

the magnitude estimation of nearby faint sources. The FOV of NGC 3603 YC is larger and for bright stars the effect of variable extinction is significant among other photometric uncertainties. In order to overcome this problem we made the following. We simulated an ensemble of stars according to a single power law initial mass function and added them on the NGC 3603 YC two-color diagram (TCD). After that the value of photometric error was adjusted till the spread in the simulated TCD matched the spread in the observed TCD (see Fig. 2.7). Our result is minimum value of error 0.025 mag for stars with masses  $3 - 10M_{\odot}$ . For faint stars we assigned an error at the same way as for Wd 1 and got a maximum error of 0.17 mag for F555W band and 0.25 mag for F814W band down to limiting magnitudes of  $m_{F555W} = 22$  mag and  $m_{F814W} = 20$  mag. Fig. 2.8 shows the photometric uncertainty as a function of magnitude for WD 1 (a,b) and for NGC 3603 YC (c,d).

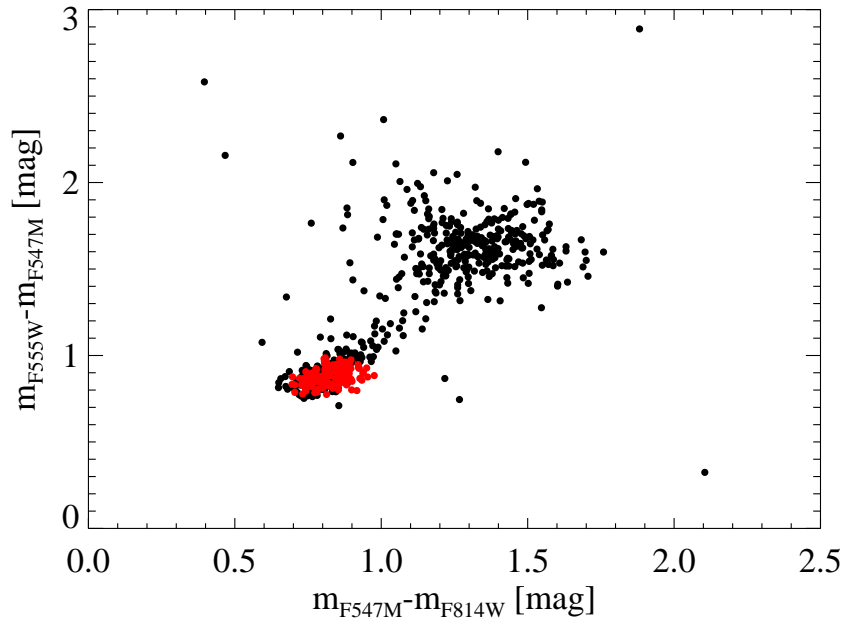


**Figure 2.7:** Two-color diagram of NGC 3603 YC. Red points are simulated stars with masses  $3 - 10M_{\odot}$  scattered within 0.025 mag.

The 2d map of the log-likelihood  $\log(L(t, DM))$  we derived for Wd 1 is presented in Fig. 2.9. There is an evident correlation between distance and age of the cluster. The closer the cluster is to Earth, the older ages for the stars with the same apparent magnitudes we get. In order to estimate the age spread, we did cuts of this map at different  $DM$  values: 12.9 mag, 13.0 mag, 13.1 mag (3.8-4.2 kpc). The normalized  $L(t)$  functions we got are presented in Fig. 2.10(a,b,c). The most probable age is 5.5 Myr at  $DM=12.9$  mag,

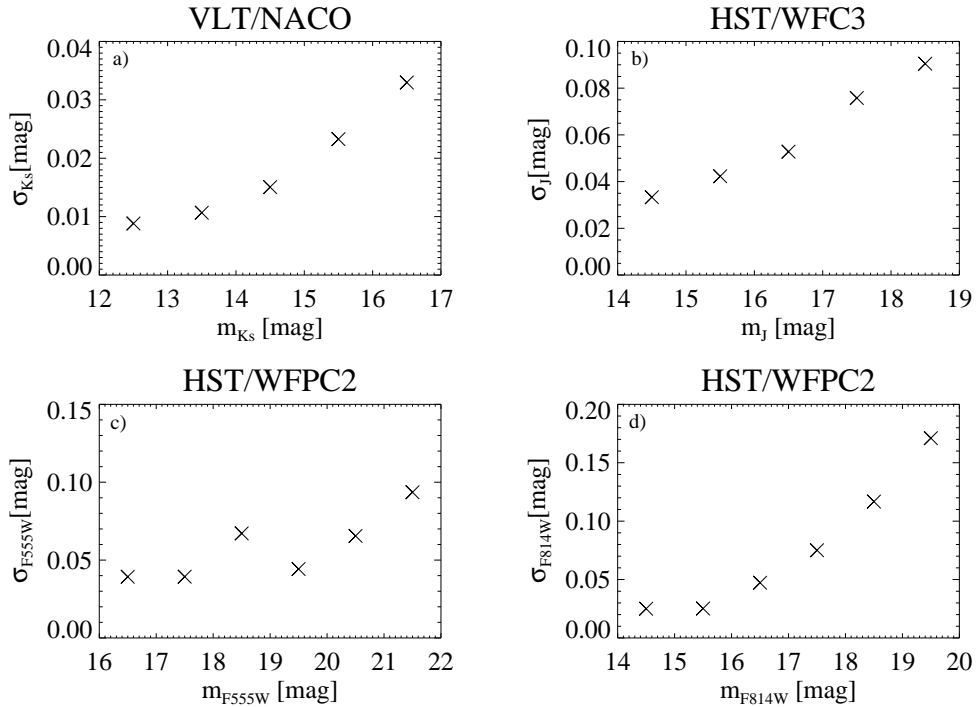


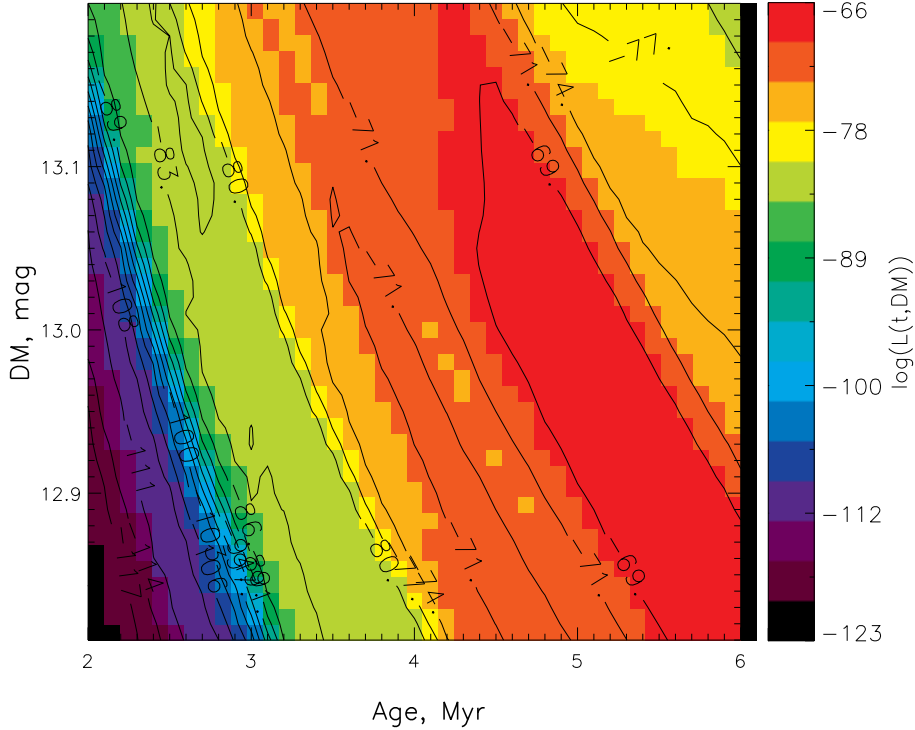
**Figure 2.8:** Photometric error of stars on VLT/NACO (a) and HST/WFC3 (b) images of Wd 1 and HST/WFPC2 images (c,d) of NGC 3603 YC. Each error value is averaged within 1 magnitude.

5.0 Myr at  $DM=13.0$  mag and 4.6 Myr and  $DM=13.1$  mag. The full width at half maximum (FWHM) of a Gaussian fitted to the  $L(t)$  function (red line in Fig. 2.10(a,b,c)) is 0.4 Myr for each distance.

The 2d map of log-likelihood  $\log(L(t, DM))$  for NGC 3603 YC is presented in Fig. 2.11. As contamination by field stars was already significantly reduced by the proper motion selection,  $P_{good}$  in Eq.(2.2) was estimated, assuming that cluster members are the stars with cluster membership probabilities  $P_{mem} > 98\%$ . This criterion was chosen in agreement with Fig. 2.5, where the majority of the stars are concentrated above this limit. The extinction  $A_v = 4.9$  mag is in agreement with the results by Sung and Bessell (2004) and Rochau et al. (2010) and the relative extinction relations from Schlegel et al. (1998). We used the same  $\alpha = 1.9$  as in Stolte et al. (2006) for the MF slope. We made cuts of this 2d map at several  $DM$  values: 14.0 mag, 14.1 mag, 14.2 mag (6.3-6.9 kpc). The result for the normalized  $L(t)$  functions at these  $DM$  values are shown in Fig. 2.12. The maximum age spread we derive for NGC 3603 YC at these distances is 0.1 Myr.

## 2. INSTANTANEOUS STARBURST OF THE MASSIVE CLUSTERS WD 1 AND NGC 3603 YC

---



## 2.6 Broadening of the age likelihood function

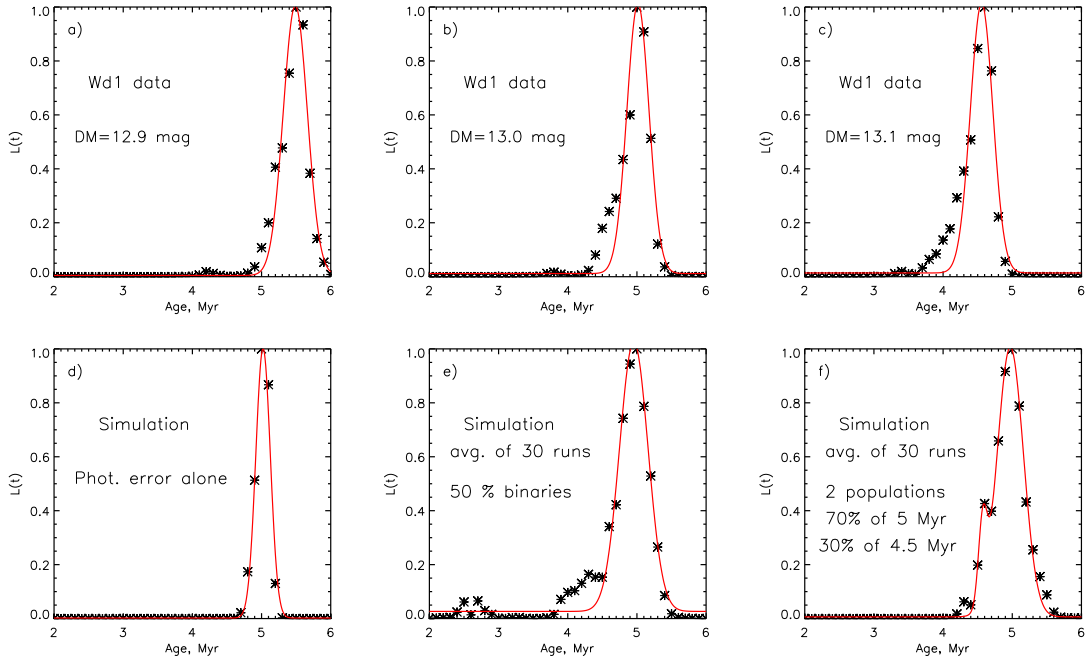


**Figure 2.10:** (a): Normalized  $L(t)$  for Wd 1 at  $DM=12.9$  mag. The red curve is a fitted Gaussian. (b): The same at  $DM=13.0$  mag. (c): The same at  $DM=13.1$  mag. (d): Normalized  $L(t)$  for the simulated 5.0 Myr population at  $DM=13.0$  mag. (e): Normalized  $L(t)$  for the simulated 5.0 Myr population at  $DM=13.0$  mag with a binarity fraction of 50%. (f): Normalized  $L(t)$  for the simulated population with 70% of the stars being 5.0 Myr old and 30% being 4.5 Myr old.

### 2.6.2 Unresolved binarity

There is considerable observational evidence that binary stars might constitute a significant fraction of a cluster population (e.g. [Sharma et al. 2008](#)). As an unresolved binary combines the light of two stars, a binary will result in an offset in brightness by up to  $-0.75$  mag in the CMD compared to a single star. For non-equal mass systems, there might also be an offset in color. Both cases lead to a broadening of the observed cluster sequence on the actual CMD.

To test how the shape of  $L(t)$  is affected by unresolved binarity, we generated stars in the CM space in a similar way as described above for photometric errors, but with a  $0.75$  mag shift along the ordinate for 50% of the artificial points (Fig. 2.13b). We choose 50% as the mean value for the binarity fraction, as recent observations at least for massive population of Wd 1 revealed a high rate (more than 40%) of binary stars ([Ritchie et al., 2009](#)). We applied the same Bayesian analysis to the simulated stars as to the real data to determine  $L(t)$ .

The normalized likelihood  $L(t)$  we obtained after combining the results of 30 simulations

## 2. INSTANTANEOUS STARBURST OF THE MASSIVE CLUSTERS WD 1 AND NGC 3603 YC

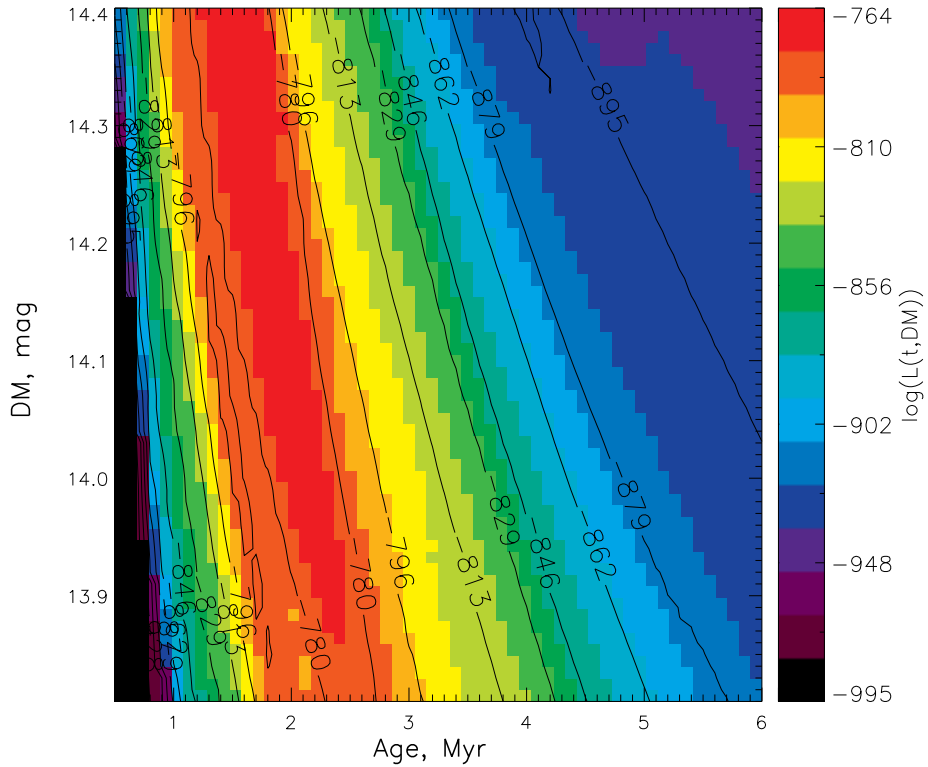


**Figure 2.11:** Two-dimensional map of log-likelihood  $\log(L(t, DM))$  for NGC 3603 YC.

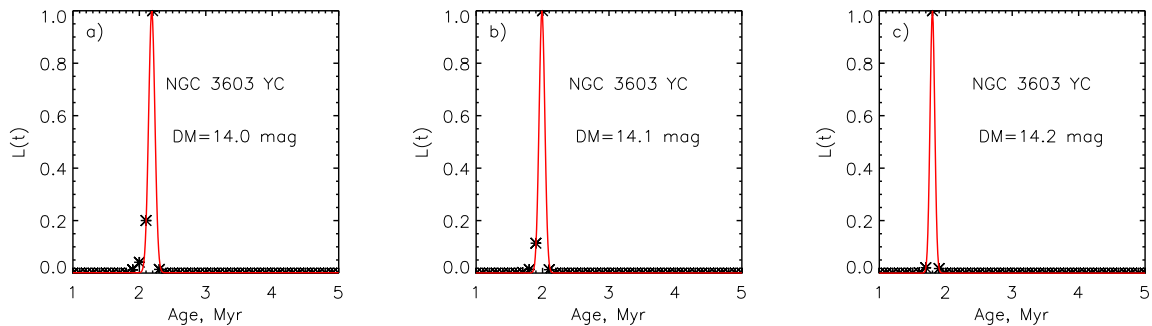


**Figure 2.12:** Normalized  $L(t)$  for NGC 3603 YC at  $DM=14.0$  mag (a),  $DM=14.1$  mag (b),  $DM=14.2$  mag (c). Red curves are fitted Gaussian functions.

on binarity for a 5.0 Myr population at  $DM$  13.0 mag is shown in Fig. 2.10e. It is clearly seen that binarity affects the shape of  $L(t)$  by adding a pronounced wing to the left from the main peak. Hence a small shoulder towards younger ages from the  $L(t)$  maximum for Wd 1 (Fig. 2.10b,c) could be caused by unresolved binarity.

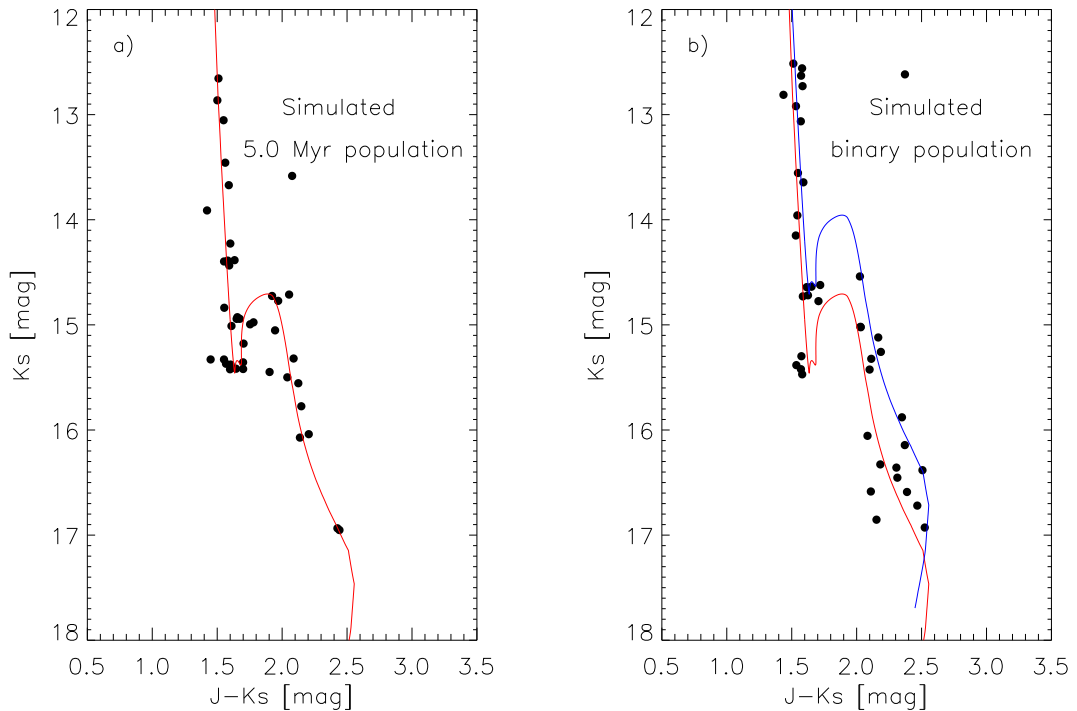


**Figure 2.13:** (a):CMD for the simulated 5.0 Myr population at  $DM=13.0$  mag. The corresponding FRANEK-Padova isochrone (red) is overplotted. (b):CMD for the simulated 5.0 Myr population with a binarity fraction of 50% at  $DM=13.0$  mag. Red line is a 5.0 Myr FRANEK-Padova isochrone at  $DM=13.0$  mag, blue line is the same but shifted vertically by 0.75 mag.

### 2.6.3 Ongoing accretion

For young stellar populations with ages  $\lesssim 10$  Myr, ongoing accretion and the accretion history of a star is also of importance. As discussed in e.g. [Zinnecker and Yorke \(2007\)](#), [Hosokawa et al. \(2011\)](#), low-mass objects, which gain mass through ongoing accretion and a non-accreting PMS star of the same mass arrive at different positions in a Hertzsprung-Russell diagram.

For starburst clusters like Wd 1 and NGC 3603 YC, this effect seems to be strongly attenuated due to the presence of very luminous and massive O-type stars in the clusters. The fast winds and the ionizing radiation from these stars evaporate and remove circumstellar material around the low-mass cluster members, and clean-out any remnant molecular gas in the cluster environment on short time scales of a few  $10^5$  yr (e.g., [Adams et al. 2004](#); [Johnstone et al. 1998](#)). This results in very little differential extinction across the starburst cluster, enabling us to constrain stellar properties using broad-band photometry ([Stolte et al. 2004](#)).

## 2. INSTANTANEOUS STARBURST OF THE MASSIVE CLUSTERS WD 1 AND NGC 3603 YC

---

### 2.6.4 Sensitivity to age spread

In order to test the ability of our method to detect the real age spreads, we simulated a mixed cluster population with two different ages and assuming random photometric errors. We repeated this procedure 30 times and calculated the averaged normalized likelihood  $L(t)$ . The result for a mixed population with 70% stars of age 5.0 Myr and 30% stars of age 4.5 Myr is shown in Fig. 2.10f. Hence a bimodal population with an age difference  $\geq 0.5$  Myr would manifest itself in a prominent secondary peak, but the latter is not revealed in case of Wd 1 (see Fig. 2.10a,b,c).

## 2.7 Discussion

Our analysis highlights the importance of a good membership selection, background rejection and characterization when analysing crowded field data. We emphasize that the photometric component of our analysis only works in young, massive clusters and older clusters with little differential extinction and absence of ongoing accretion. Other environments require detailed spectroscopic analyses to establish precise effective temperatures and luminosities for individual stars, as has been exemplified in the case of ONC (Hillenbrand, 1997) and W3 Main (Bik et al., 2012).

Isochrones based on FRANEC and Padova evolutionary models, and ATLAS9 atmospheric models provide a good match to observed cluster sequences in the age range from 1 to 5 Myr and mass range from 0.6 to 14  $M_{\odot}$  for solar metallicities. Extending the sample of cluster members to lower masses could help to benchmark evolutionary tracks and atmospheric models for young, low-mass stars and quite possibly even brown dwarfs.

As clearly seen from the Fig. 2.10, the shape of  $L(t)$  function for Wd 1 most likely undergoes the influence of photometric uncertainties and unresolved binarity. As all of these effects make  $L(t)$  broader compare to what we would have in their absence, we conclude on an age spread of less than 0.4 Myr for the  $\approx 5.0$  Myr old Wd 1 and less than 0.1 Myr for the  $\approx 2.0$  Myr old NGC 3603 YC. However, as mentioned in introduction, (Beccari et al., 2010) suggest an age spread of 10 Myrs for NGC 3603 YC PMS population. There are several effects that could have caused such a big apparent age spread. Firstly the CMD region that was used by their analysis contains very low-mass and hence faint PMS stars with high photometric error. Secondly the images of NGC 3603 YC are highly contaminated by field stars and statistical subtraction of them is not straightforward in order to discriminate between cluster and non-cluster members and estimate an age spread of the cluster. Our result suggests that in both cases the clusters formed in a single event once a sufficient gas mass had been aggregated and compressed to overcome internal thermal, turbulent or magnetic support, and to initiate an avalanche-like star formation event. This

finding seems to be in agreement with theoretical predictions that clusters with masses between  $10^4$  to  $10^5 M_{\odot}$  lose their residual gas on a timescale shorter than their crossing times (Baumgardt et al., 2008). For Wd 1 and NGC 3603 YC crossing times have been estimated to be of the order of 0.3 Myr (Brandner et al., 2008) and 0.03 Myr (Pang et al., 2010), respectively.

Another cluster, the Quintuplet, one of the six most massive young, open clusters in our galaxy, has most likely a similar evolution scenario. Liermann et al. (2012) suggest an instantaneous burst of its formation at about 3.3- to 3.6 Myr ago from the comparison of number ratios for the different subclasses of high-mass stars with population synthesis models. Furthermore, from the isochrone fitting to the Hertzsprung-Russell diagram (HRD) of the cluster the authors found a slight difference in age between O stars and WN stars. This might be due to the fact that the most massive stars have formed last in the cluster formation process. For the low-mass population of the Quintuplet cluster Hußmann et al. (2011) derived a 4 Myr coeval age by isochrone fitting to the transition region from the PMS to the MS in the member CMD.

Starburst clusters in our galaxy represent a similar way of star formation and can serve as templates for studying extragalactic starburst clusters.

**2. INSTANTANEOUS STARBURST OF THE MASSIVE CLUSTERS  
WD 1 AND NGC 3603 YC**

---

# The Initial Mass Function and internal dynamics of the starburst cluster Westerlund 1 from near-infrared adaptive optics observations

*With an estimated initial mass of more than 50000 solar masses, the  $\sim 5$  Myr old cluster Westerlund 1 (Wd 1) is possibly the most massive young cluster in the Milky Way. In an effort to better discriminate between cluster members and field stars, we have analyzed multiple epochs of near infrared data obtained with the VLT adaptive optics system NACO. The astrometric data enable us to assign cluster membership probabilities to individual stars, to measure the internal velocity dispersion of the cluster and to derive the slope  $\Gamma = -0.46$  of the completeness-corrected IMF for the mass range  $0.6$  to  $18.0 M_{\odot}$  in the cluster center ( $r < 0.23$  pc). New value of IMF slope is in a good agreement with the change in mass function found by [Brandner et al. \(2008\)](#).*

### 3.1 Introduction

Starburst clusters are well known for their high rate of star formation. They contain from ten thousand to a million of stars with a rich population of high-mass stars. All the stars in such clusters were born approximately at the same time (see chapter 2) and are localized roughly at the same distance from the Earth. It gives the opportunity to derive the masses of extremely rare and massive stars at a single age, but at various stages of their evolution. Due to the compactness of the clusters, the light from the most massive stars prohibits to resolve the less massive population. However, with the implementation of adaptive optics (AO) into telescopes, substantial progress has been done in resolving the low mass stars in the starburst clusters. Spatially resolved Galactic clusters will help to understand the cluster mode of star formation that can be observed in unresolved extragalactic star forming regions. In particular, it will be useful in answering the question of whether the initial mass function (IMF) is universal or not, meaning that the ratio of low-mass stars to high-mass stars in a newborn stellar population is the same throughout the universe. The accurate measurements of the IMF is often considered to be the key to understanding star formation. The concentration of high-massive stars in the core of the cluster gives an evidence of mass segregation. The study of the changes of the mass function (MF) with time can tell us if the mass segregation was primordial or dynamic and whether the cluster is likely to remain bound or disperse into the field with time.

Around 10 young massive stellar clusters are known in our Galaxy. Wd1 is currently the most massive one known in the Milky Way. Its population involves hundreds of OB stars, 24 Wolf-Rayet stars, several yellow hypergiants and red supergiants (Clark et al. 2005; Crowther et al. 2006). Such a rich population of rare massive objects make Wd1 an interesting object to study. Brandner et al. (2008) analysed the NTT/SofI observations of Wd1 sensitive to solar mass stars at a distance of 4 kpc. The slope of the stellar mass function they derived for stars with masses  $3.4 - 27 M_{\odot}$  is getting steeper for larger annuli, from  $\Gamma = -0.6$  within  $R < 0.75$  pc to  $\Gamma = -1.7$  for  $R > 2.1$  pc. Gennaro et al. (2011) confirms these findings using the same data set but a two-dimensional approach for the mass function. Furthermore from the density distribution analysis the authors derived that the cluster is elongated along the Galactic plane with an axial ratio  $a : b = 3 : 2$ . In this chapter we analyse multi-epoch high-resolution AO VLT/NACO data of Wd1 in order to resolve the low mass population of the cluster down to  $0.4 M_{\odot}$ , study velocity distribution of the cluster stars, and to measure IMF for the cluster center.

### 3.2 Observations

VLT/NAOS-CONICA adaptive optics observations of Wd 1 were made on two epochs from April 2003 and April 2008. High angular resolution  $JHK_S$  (2008- only  $H, K_S$ ) observations with a plate scale of 27 mas/pixel were centered approximately on  $RA(2000) = 16h47m05s, Dec(2000) = -45^\circ50'56''$ . The overlapping field of view (FOV) was  $24'' \times 24''$ , corresponding to  $0.45 \text{ pc} \times 0.45 \text{ pc}$  (see Fig. 3.1) at 4.0 kpc distance (Gennaro et al., 2011).

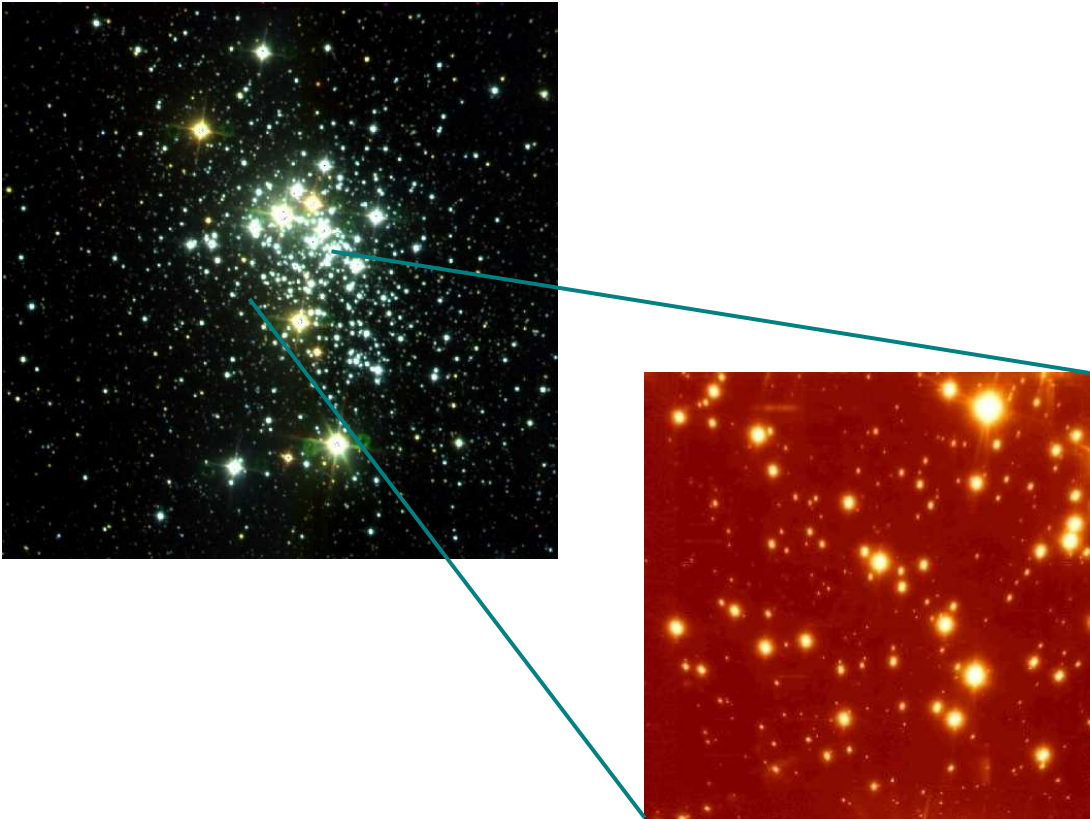


**Figure 3.1:** The location of Wd 1 NACO FOV on composite colour  $JHK_S$  image of Wd 1.

### 3.3 Data reduction

The observations of Wd 1 in 2008 were reduced using NAOS/CONICA imaging PyRAF/IDL data reduction pipeline, developed by A.Stolte and B.Hussman at the University of Cologne. It includes sky subtraction (sky frames with identical integration time, centered on  $RA(2000) = 16h47m17s, Dec(2000) = -45^\circ53'01''$ , were obtained directly after the Wd 1 observations), bad pixel and cosmic ray events corrections, flat fielding. In ad-

### 3. THE INITIAL MASS FUNCTION AND INTERNAL DYNAMICS OF THE STARBURST CLUSTER WESTERLUND 1 FROM NEAR-INFRARED ADAPTIVE OPTICS OBSERVATIONS

---

dition it removes the 50 Hz pickup noise in all dark, sky and object frames of 2008 data. This noise appeared after the replacement of the detector in 2004 and has a horizontal stripe feature about 2 to 5 pixels wide. Prior to the image combination, the pipeline weighted each frame by the Strehl ratio. This enables us to give the strongest weight for the highest resolution images during the drizzle combination and hence to enhance the resolution of the final science frame. By combination of 44  $K_S$  frames with integration times of 30 s each, we got an image with a total integration time of 22 min, with a core FWHM of 80 mas.

The data reduction of 2003 NACO data was carried out using the eclipse jitter routines (Devillard, 2001).  $H, K_S$  frames 2003 with integration times of 1 min were coadded, resulting in total integration times of 5 min and 8 min, respectively.

Stellar positions and PSF fitting photometry were derived for both epochs using the IRAF implementation for the stellar photometry in crowded fields DAOPHOT (Stetson, 1987). For the 2008 data, we modeled the PSF using a Moffat function, as compared to a Gaussian this allows to fit the 'wings' of the stellar profiles (Trujillo et al., 2001). The accuracy of stellar position's determination with DAOPHOT was established in the following way. We divided 44 frames of 2008 epoch into 2 data sets, 22 frames in each set, by choosing next nearest frame in time. Each of this data sets was separately reduced with NAOS/CONICA reduction pipeline and as a result we got 2 different science frames of the same epoch. The positions of 257 stars were compared in these images. The dependence of the positional error in galactic longitude  $l$  and galactic latitude  $b$  via magnitude of the star is presented on Fig. 3.2. It is clearly seen, that the error increases rapidly for the stars fainter than  $K_S = 20$  mag.

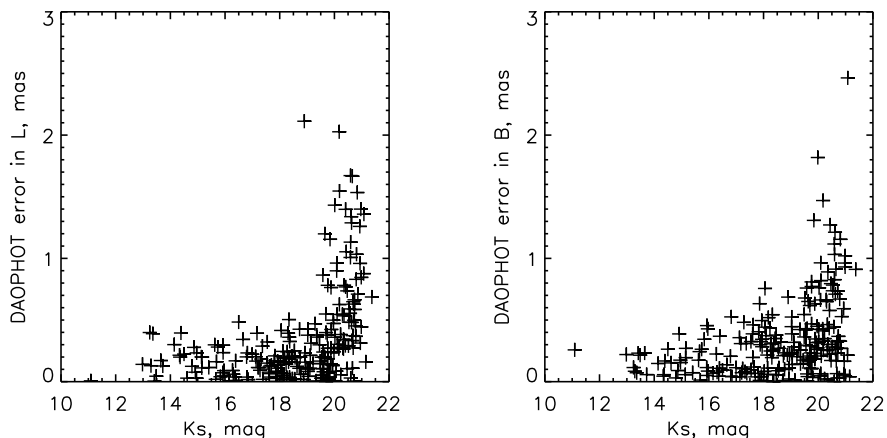


**Figure 3.2:** The error in stellar position in  $l$  (left) and  $b$  (right) derived with DAOPHOT by comparing two halves of the full data set.

### 3.3.1 Geometric transformation

The NACO pixel coordinates of 2008 were converted to NACO 2003 frame, using IRAF task GEOMAP. Geometric transformation was defined by specifying x and y shifts, scaling factor and the rotation angle between the images. The final RMS errors of the transformation was 0.58 mas. The instrumental source magnitudes were converted to calibrated 2MASS magnitudes, where the photometric zero points were established by comparison of these 2 types of magnitudes for some isolated and bright sources.

### 3.3.2 Photometric errors

There are two sources of photometric uncertainty: random and systematic. The last one is caused by photometric zero point determination when the instrumental magnitudes are converted to apparent magnitudes. The random error is caused mainly by bright stars, whose PSF wings affect the magnitude estimation of nearby faint sources. DAOPHOT errors come from the Poisson noise in stellar counts and cannot be used in crowded fields. To evaluate the realistic error as a function of magnitude and the position of the star, we did artificial star experiments as described in [Gennaro et al. \(2011\)](#). We simulated the stars on the NACO 2003 image of Wd 1 and then recovered them by DAOPHOT. The difference between the input and output magnitudes was considered as a robust estimate of the real photometric error. To assign the error to each Wd 1 star in our sample, we selected only those simulated stars that were located in the neighbourhood of the science target. The photometric errors we derived for the cluster members in  $K_S$  and  $H$  bands are presented in Fig. 3.3.

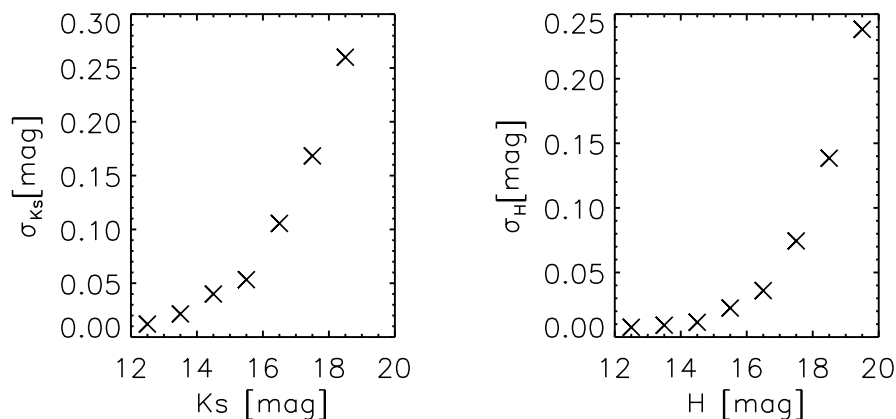


**Figure 3.3:** The photometric error of stars in Wd 1 as a function of magnitude in the  $K_S$ (left) and  $H$ (right) bands. Each error value is averaged within 1 magnitude.

### 3. THE INITIAL MASS FUNCTION AND INTERNAL DYNAMICS OF THE STARBURST CLUSTER WESTERLUND 1 FROM NEAR-INFRARED ADAPTIVE OPTICS OBSERVATIONS

---

#### 3.4 Proper motion membership selection

Wd1 is located in the Scutum-Crux spiral arm very close to the galactic plane ( $b = -0.35^\circ$ ) and is therefore projected against a rich population of field stars. The separation of the cluster members from field stars is essential for an unbiased determination of the cluster parameters, including the stellar mass distribution. Different techniques are used for membership evaluation in nearby star-forming regions: kinematic, photometric (Kharchenko et al., 2004) and statistical (Sanders, 1971). The kinematic method includes proper motion criteria and is the most objective one when the accuracy of the proper motion determination is good enough. Such a technique has already been successfully applied for several Milky Way starburst clusters (e.g., Hußmann et al. 2011; Stolte et al. 2008), as well as for Wd1 by mapping NACO and HST/ACS data over a 2 years time baseline (Stolte and Brandner, 2010). In our case we used the same method but did direct NACO to NACO mapping over a 5 years time baseline, which considerably increased the final accuracy. The proper motion diagram for Wd1 based on these 2 epochs of NACO adaptive optics observations is shown in Fig. 3.4.

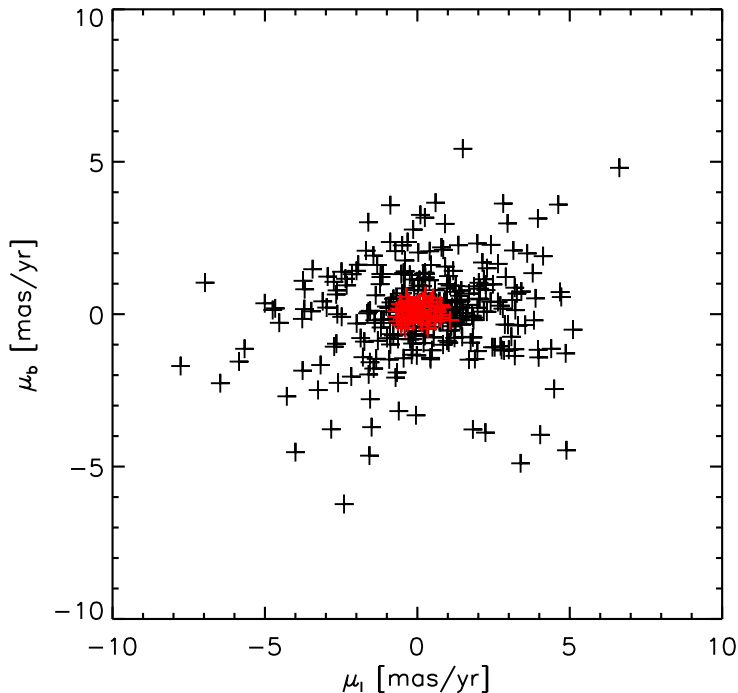


**Figure 3.4:** Proper motion of the stars in Wd1 reference frame in Galactic coordinates. Cluster members are marked by red.

### 3.4 Proper motion membership selection

The expected proper motion for stars along the line of sight towards Wd 1 ( $l = 339.55^\circ$ ) as a function of distance from the Sun is presented in Fig. 3.5. Wd 1 itself should be located at around 3.5 to 4.5 kpc. As the accuracy of our proper motion measurements is less than one milliarcsecond, we can nicely discriminate between foreground stars and cluster members and make estimates of the internal velocity dispersion of Wd 1.

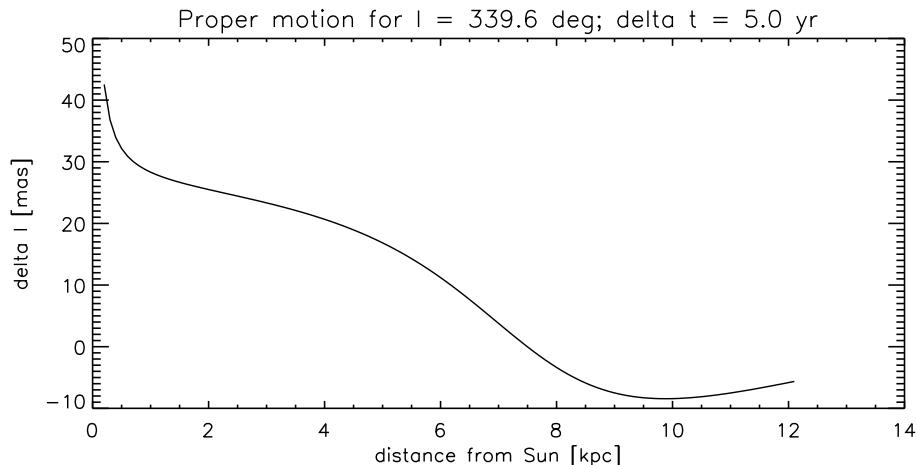


**Figure 3.5:** Observable proper motion for stars along the line of sight towards Wd 1 vs. distance from the Sun.

The algorithm, which we used for selecting the cluster members is similar to the one described in [Jones and Walker \(1988\)](#). The membership probability of a star with magnitude  $m$ , proper motion  $\mu_l, \mu_b$ , and distance from the cluster center  $r$  is defined as the ratio of the density of cluster stars to the density of cluster plus field stars:

$$P(m, \mu_l, \mu_b, r) = \frac{\frac{\rho(m,r)}{f_o(m)} \Phi_c(m, \mu_l, \mu_b)}{\Phi_f(m, \mu_l, \mu_b) + \frac{\rho(m,r)}{f_o(m)} \Phi_c(m, \mu_l, \mu_b)}, \quad (3.1)$$

where  $\rho(m, r)$  is the areal density of the cluster stars,  $f_o(m)$  - the same for the field stars, and  $\Phi_c, \Phi_f$  are the normalized distribution of cluster and field stars in the proper-motion-vector diagram respectively, they are given by

$$\Phi_c(m, \mu_l, \mu_b) = (2\pi\sigma_l\sigma_b)^{-1} e^{-1/2 \left[ \left( \frac{\mu_l - \mu_{l,c}}{\sigma_l} \right)^2 + \left( \frac{\mu_b - \mu_{b,c}}{\sigma_b} \right)^2 \right]}, \quad (3.2)$$

$$\Phi_f(m, \mu_l, \mu_b) = (2\pi\Sigma_l\Sigma_b)^{-1} e^{-1/2 \left[ \left( \frac{\mu_l - \mu_{l,f}}{\Sigma_l} \right)^2 + \left( \frac{\mu_b - \mu_{b,f}}{\Sigma_b} \right)^2 \right]}, \quad (3.3)$$

### 3. THE INITIAL MASS FUNCTION AND INTERNAL DYNAMICS OF THE STARBURST CLUSTER WESTERLUND 1 FROM NEAR-INFRARED ADAPTIVE OPTICS OBSERVATIONS

---

where indexes  $l$  and  $b$  correspond to longitude and latitude in Galactic coordinates,  $\sigma_l, \sigma_b$  are the proper motion dispersions of the cluster stars,  $\Sigma_l, \Sigma_b$  are the proper motion dispersions of the field stars in two coordinates,  $\mu_{l,c}, \mu_{b,c}, \mu_{l,f}, \mu_{b,f}$  are mean proper motions of the cluster and field stars, respectively. The last 8 parameters were found by fitting bivariate normal distribution to the distribution of stars in a proper-motion-vector point diagram (see Fig. 3.6). As these values have a dependence on magnitude, we made a linear extension of the parameters, which were determined in 2 intervals of magnitudes,  $13 < m < 15$  mag and  $14 < m < 16$  mag. These intervals were chosen, such as to contain sufficient amount of stars with accurate values of proper motions. By fitting two-component Gaussians we took into account that the ratio of cluster members to field stars is the same in  $l$  and  $b$ .

In order to calculate the areal density of the cluster stars  $\rho(m, r)$ , we used the results of Gennaro et al. (2011) on NTT/SofI data (FOV  $4.5' \times 4.5'$ ) of Wd1. According to this paper, Wd1 is elongated, with surfaces of constant density lying on ellipses. After matching our NACO data with the SofI data, we found an areal density of cluster stars  $\rho(m, r)$  dependent on its magnitude and position on SofI data based on the results of Gennaro et al. (2011). To estimate the areal density of the field stars  $f_o(m)$ , we used the Wd1 comparison field observed with NTT/SofI in 2004 and centered on  $RA(2000) = 16h47m43s, Dec(2000) = -46^\circ 03' 47''$  ( $\approx 7'$  to the east and  $\approx 13'$  to the south of Wd1). For a detailed description of the NTT/SofI data and data reduction, we refer to the work of Brandner et al. (2008). We calculated the number of stars per magnitude unit on the comparison SofI field and then used Besançon model of our Galaxy (e.g., Robin and Creze 1986; Robin et al. 2004) to predict a ratio of number of stars on our NACO FOV to the number of stars on the SofI FOV depending on the magnitude. This gave us an estimate of  $f_o(m)$  for our VLT/NACO FOV.

The histogram of the membership probabilities  $P$  that we got is presented in Fig. 3.7. The stars with membership probabilities  $P \geq 90\%$  (red crosses in Fig. 3.4) were selected as cluster members.

#### 3.5 Dynamical properties of Wd1

The proper motion distribution in Fig. 3.4 comes not only from the internal velocity dispersion of the cluster but from instrumental effects as well. This includes the error in stellar position  $\sigma_{pos}$  recovered by DAOPHOT (see sect. 3.3) and the error of geometrical transformation  $\sigma_{tr}$  from 2008 to 2003 data (see sect. 3.3.1). Fig. 3.8 shows the observed proper motion dispersion of the cluster members as a function of  $K_S$ -magnitude, averaged within 1 mag. For our further analysis of the internal velocity dispersion of the cluster we took only the stars with  $12 \leq K_S \leq 16$  mag. The bright stars with  $K_S < 12$  mag are most

### 3.5 Dynamical properties of Wd 1

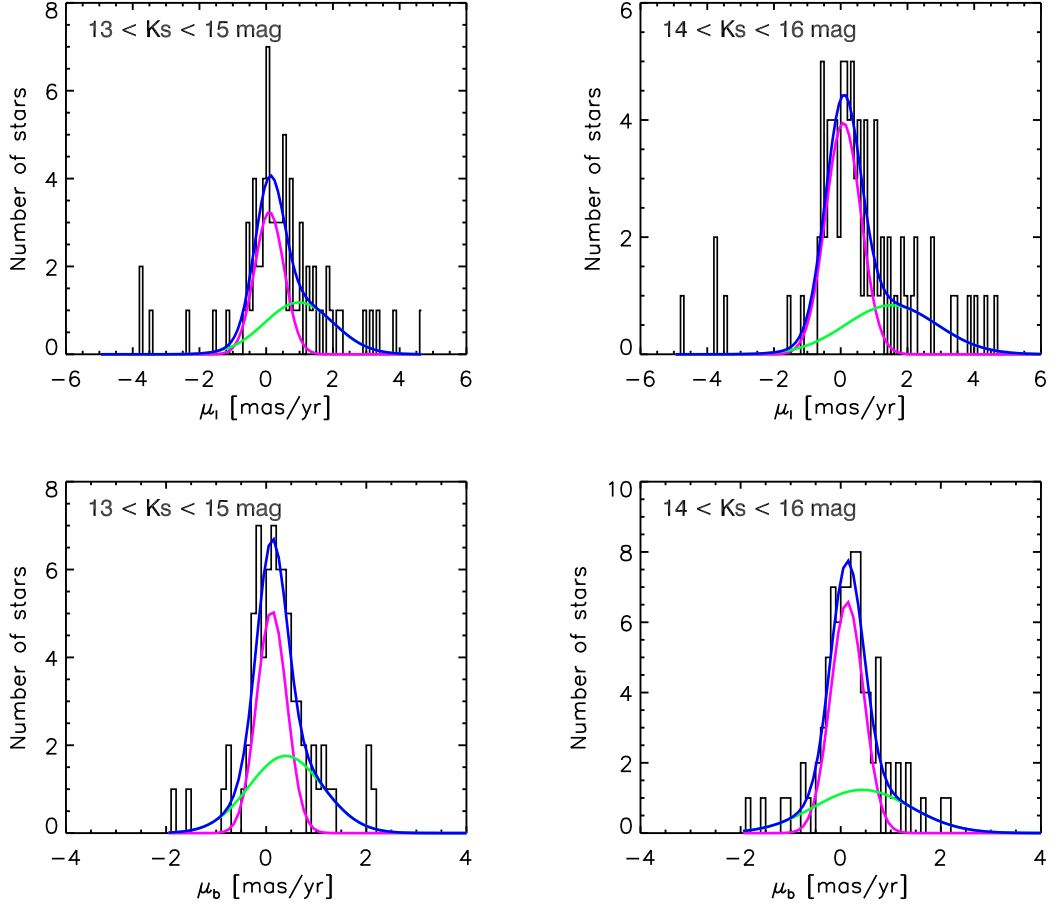


**Figure 3.6:** Histograms of number of stars vs. proper motion components in galactic longitude  $l$  (top) and galactic latitude  $b$  (below). Histograms are fitted by two-component Gaussians (blue), where one component represents the distribution of the field stars (green), the other the distribution of the cluster members (purple). These plots are made for the magnitude intervals  $13 < K_S < 15$  mag (74 stars, left) and  $14 < K_S < 16$  mag (88 stars, right).

likely saturated and faint stars with  $K_S > 16$  mag have large positional errors because of low signal-to-noise ratio. The stars with  $12 \leq K_S \leq 16$  mag show the consistency in their observed proper motion dispersion with  $\sigma_{obs_L} = 0.41$  mas/yr in  $l$  and  $\sigma_{obs_B} = 0.25$  mas/yr in  $b$ . These values were corrected for the instrumental effects, i.e. positional error  $\sigma_{pos} = 0.03$  mas/year the same in  $l$  and  $b$  for 2003 and 2008 epoch, and the error of transformation  $\sigma_{tr} = 0.12$  mas/year. From  $\sigma_{int} = \sqrt{\sigma_{obs}^2 - 2\sigma_{pos}^2 - \sigma_{tr}^2}$  we got Wd1 internal velocity dispersion of  $\sigma_{int_L} = 0.39 \pm 0.05$  mas/year in  $l$  and  $\sigma_{int_B} = 0.22 \pm 0.06$  mas/year in  $b$ , corresponding to  $7.4 \pm 1.0$  km/s and  $4.2 \pm 1.1$  km/s, respectively.

### 3. THE INITIAL MASS FUNCTION AND INTERNAL DYNAMICS OF THE STARBURST CLUSTER WESTERLUND 1 FROM NEAR-INFRARED ADAPTIVE OPTICS OBSERVATIONS

---

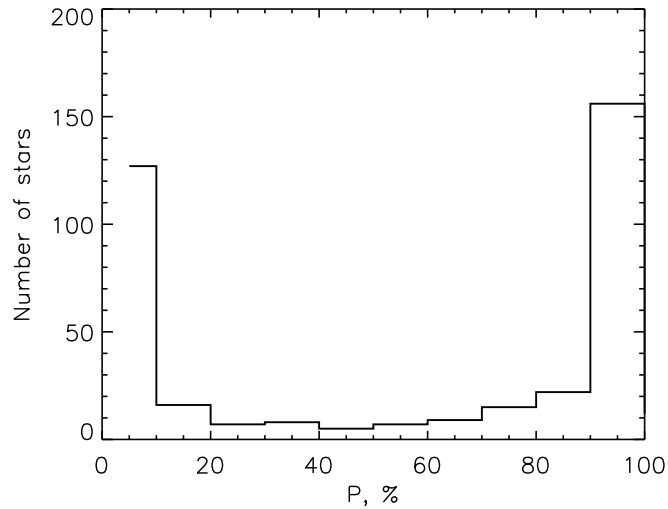


**Figure 3.7:** Histogram of the membership probabilities  $P$ .

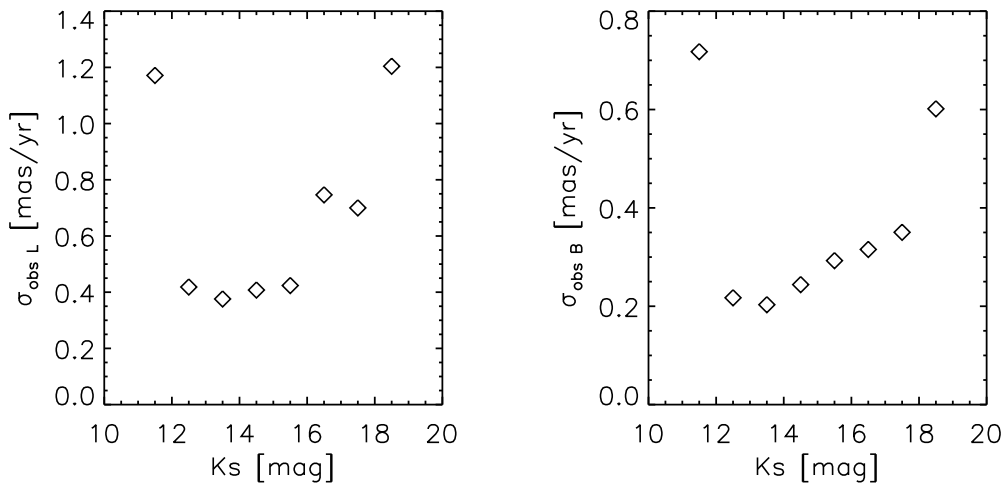


**Figure 3.8:** The observed proper motion dispersion in  $l$  (left) and  $b$  (right) as a function of stellar magnitude.

### 3.6 Colour-magnitude diagram of Wd 1

The proper motion selection of cluster members allowed to significantly clean the colour-magnitude diagram (CMD) of the cluster. Fig. 3.9 shows  $K_S$  vs.  $H - K_S$  CMD of Wd 1, including all the stars in our sample (left), CMD for the stars with  $P < 90\%$

### 3.6 Colour-magnitude diagram of Wd 1

(center), which most probably represent the field contamination, and CMD for the cluster members, i.e. for the stars with  $P \geq 90\%$  (right). The field subtracted CMD looks much cleaner, though there are still some stars to the left and to the right from the MS, which might be blue foreground stars or red background stars with proper motions similar to the cluster members. It is easy to see that most of the faint stars constitute the field contamination. This could be explained by increasing astrometric uncertainty with magnitude (see Fig. 3.2), and hence a larger scatter of faint stars in the proper motion diagram (see Fig. 3.4). The massive stars with  $K_S < 11.5$  mag have already started to evolve off the MS.

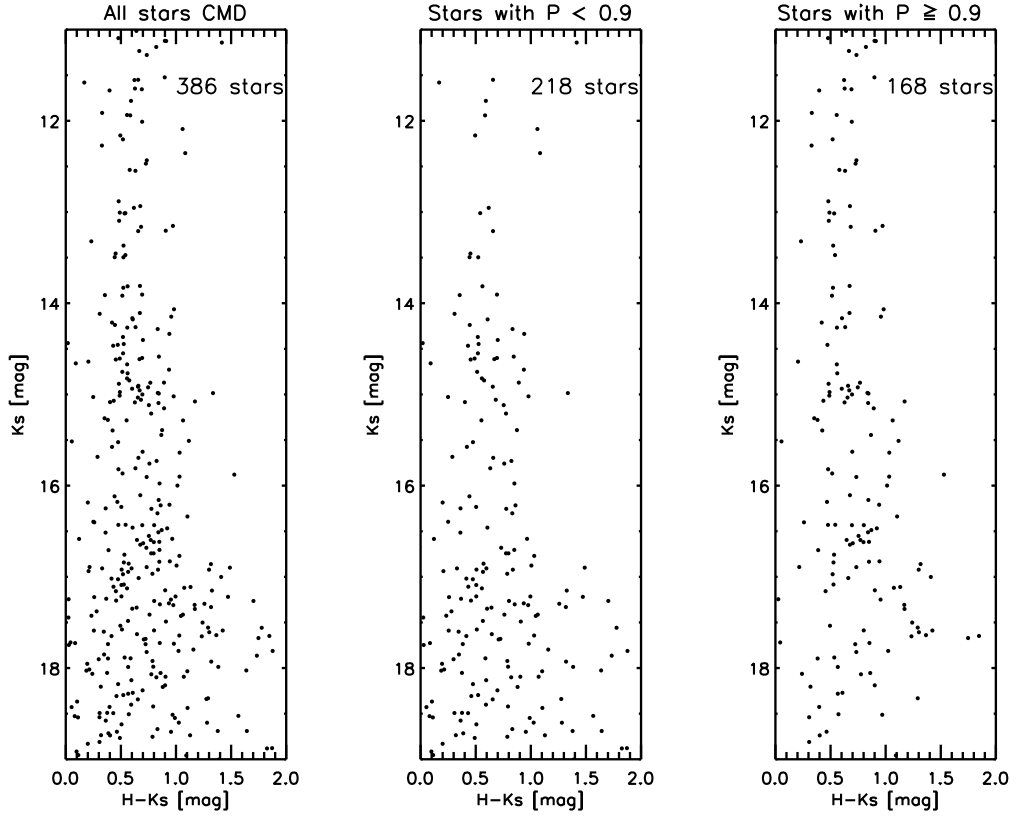


**Figure 3.9:** *Left:* CMD of the cluster (including field contamination). *Center:* CMD for the stars with cluster membership probability  $P < 90\%$ . *Right:* CMD for the stars with  $P \geq 90\%$ .

For a detailed analysis of the mass function, we used the same isochrones, extinction law and the values for a distance and age of Wd 1 as in chapter 2. The 5.0 Myr FRANEC-Padova isochrone at  $DM=13.0$  mag is overplotted to the field subtracted CMD in Fig. 3.10. The stellar masses were derived based on the comparison of their observed magnitudes with this isochrone.

### 3. THE INITIAL MASS FUNCTION AND INTERNAL DYNAMICS OF THE STARBURST CLUSTER WESTERLUND 1 FROM NEAR-INFRARED ADAPTIVE OPTICS OBSERVATIONS

---

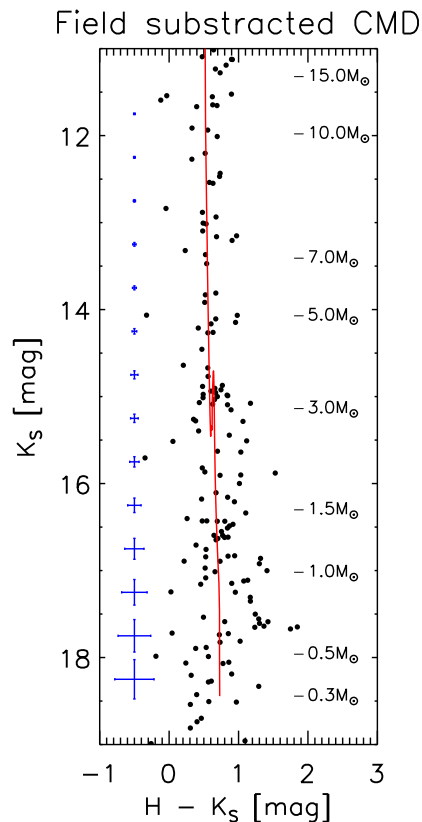


**Figure 3.10:** CMD for the cluster members of Wd1. Red line is a 5.0 Myr FRANEC-Padova isochrone at  $DM=13.0$  mag. Error bars (blue) indicate the typical errors in color and magnitude.

### 3.7 Completeness

Some of the stars on the image were not detected because of their faintness and some because of the big contrast with their neighbours. As all of these effects lead to the incorrect cluster IMF, we have done simulations to derive incompleteness corrections. The way the simulations were done is the same as in [Gennaro et al. \(2011\)](#). We added artificial stars on the Wd1  $K_S$  and  $H$  2003 images with the same PSF, as was obtained by fitting PSF to the reduced science frames and then analysed the images using DAOPHOT. In order not to change the crowding characteristic of the frames, only 10 stars per run were added, and 50 iterations were done for each magnitude bin. In total we added 4500 stars on  $K_S$ -image in magnitude range from  $12.5 < K_S < 21.5$  mag and 5500 stars on  $H$ -image in magnitude range  $10.5 < H < 21.5$  mag. The stars were randomly distributed on the images with a typical separation of 25 pixel. The next step was the calculation of the number of artificial stars that were recovered by DAOPHOT as a function of their position  $x, y$  on the

### 3.8 The initial mass function of Wd 1

image and magnitude. Following the technique from Gennaro et al. (2011), we built a Fermi-like type function  $C(x, y, K_S) = \frac{\alpha(x, y)}{e^{\frac{K_S - \beta(x, y)}{\gamma(x, y)}} + 1}$ ,  $C(x, y, H) = \frac{\alpha_1(x, y)}{e^{\frac{H - \beta_1(x, y)}{\gamma_1(x, y)}} + 1}$  for the completenesses in  $K_S$ - and  $H$ -bands. Once  $\alpha, \beta, \gamma, \alpha_1, \beta_1, \gamma_1$  were calculated, the completeness values  $C_{K_S}, C_H$  were assigned to each cluster member of Wd 1. The result for the average completeness is presented in Fig. 3.11, overplotted with the best fitted Fermi-functions. Fig. 3.12 shows the NACO  $K_S$  2003 frame with superimposed  $K_S$  50% completeness contours. The labels correspond to the  $K_S$  magnitudes for which the completeness drops to 50%.

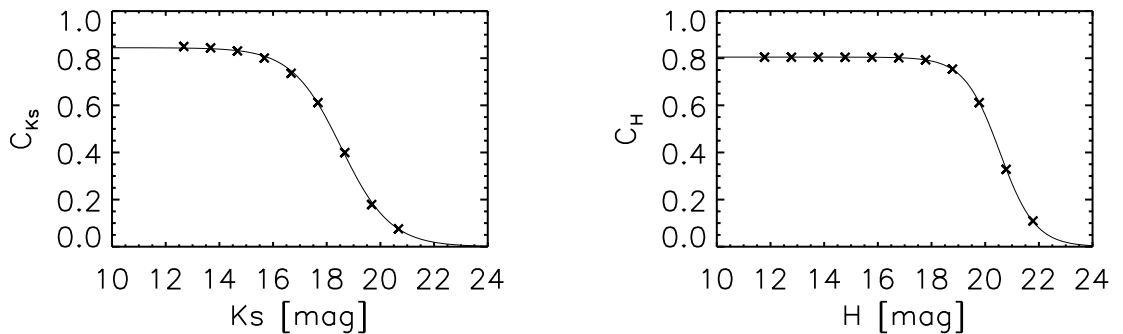


**Figure 3.11:** Average completeness as a function of magnitude for  $K_S$  (left) and  $H$  (right) bands. The best fitted Fermi-functions are overplotted.

### 3.8 The initial mass function of Wd 1

Wd 1 contains a full range of stellar masses and most of them at an age when they are only a little affected by dynamical and stellar evolution. Thus Wd 1 gives a unique opportunity to study its initial mass function. Stellar masses were assigned based on the  $H, K_S$ -magnitudes and  $(H - K_S)$  colours of the stars and a 5.0 Myr FRANEC-Padova isochrone. Fig. 3.13 (left) shows the IMF of the cluster for the mass range  $0.4$  to  $18.0 M_\odot$ , assuming solar metallicities for the stars. The dashed line gives the IMF of Wd 1 corrected by completeness factor  $\frac{1}{C_{K_S} \cdot C_H}$ . The 50% completeness limit is indicated by a vertical dotted line. By only counting the stars with masses between the respective 50% completeness limit ( $0.6 M_\odot$ ) and  $18.0 M_\odot$ , we fitted the IMF slope of  $\Gamma = -0.46$  (blue line). This value changes slightly, depending on our membership selection, including the intervals of magnitude that we have used to fit a bivariate normal distribution to the distribution of stars in a proper-motion-vector point diagram (see sect. 3.4). Another source of error comes from the photometric zero point determination, as discussed in sect. 3.3.2. To

### 3. THE INITIAL MASS FUNCTION AND INTERNAL DYNAMICS OF THE STARBURST CLUSTER WESTERLUND 1 FROM NEAR-INFRARED ADAPTIVE OPTICS OBSERVATIONS

---

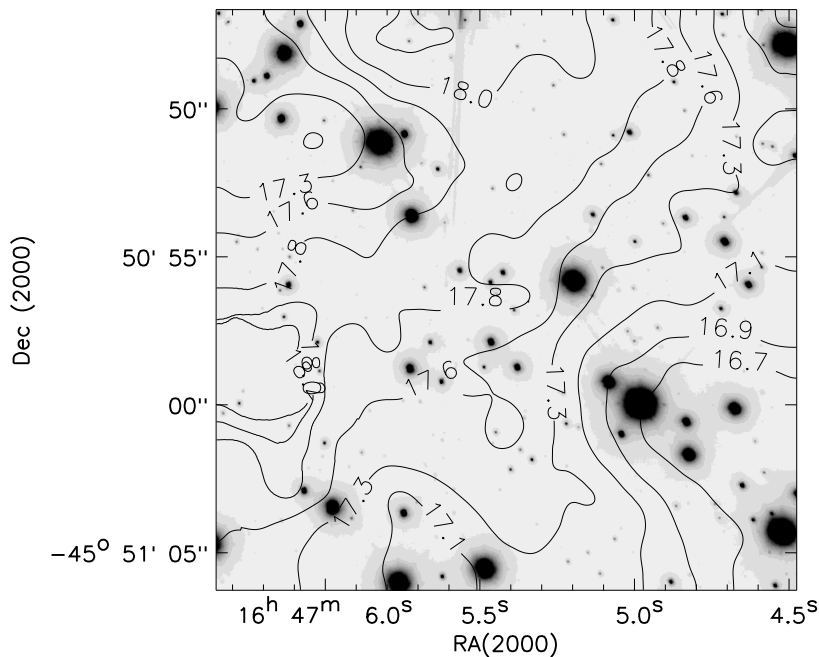


**Figure 3.12:** NACO  $K_S$  2003 image of Wd 1 with superimposed  $K_S$  50% completeness contours. The labels correspond to the  $K_S$  magnitudes for which completeness is 50% along the contours.

overcome these uncertainties, we did tests on the changes of IMF slope by varying the parameters, mentioned above. We found, that  $\Gamma$  lies within the interval  $[-0.5, -0.2]$ . The slopes derived from cumulative IMF are more robust (e.g. [Stolte et al. \(2006\)](#)), because of the absence of binning biases. They are created by consecutively adding stars with decreasing mass, starting with the most massive star observed. The cumulative IMF for Wd 1 is shown in Fig. 3.13 (right). Overplotted are cumulative functions as expected from power laws with different slopes  $\Gamma$ . The observed cumulative IMF matches the shape expected from a power law distribution with an index between  $-0.1$  and  $-0.5$ , consistent with the derived  $\Gamma = -0.46$ .

### 3.9 Discussion and summary

We analysed high spatial resolution  $H$ ,  $K_S$ -images of the center of Wd 1 obtained with the VLT NAOS-CONICA Adaptive Optics instrument at the Paranal Observatory. The cluster members were separated from the field star contamination based on their observed proper motions over 5 years time baseline. By subtracting the instrumental effects from the proper motion distribution of the cluster members, we obtained the Wd 1 internal ve-

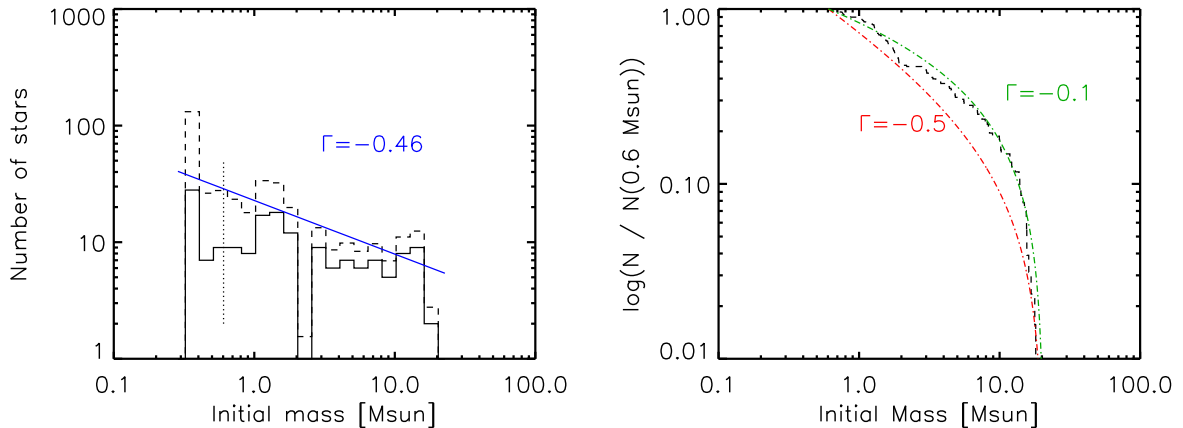


**Figure 3.13:** *Left:* IMF for the central region of Wd 1. The dashed line gives completeness-corrected IMF. The 50% completeness limit is indicated by a vertical dotted line. Blue line corresponds to a fitted IMF slope. *Right:* Cumulative IMF for stars with masses between 0.6 and 18.0  $M_{\odot}$ . Overplotted are cumulative functions as expected from power laws with slopes  $\Gamma = -0.1$  (green) and  $\Gamma = -0.5$  (red).

locity dispersion of  $\sigma_{int_L} = 7.4 \pm 1.0$  km/s in  $l$  and  $\sigma_{int_B} = 4.2 \pm 1.1$  km/s in  $b$ . These values are higher than 1D proper motion dispersion  $\sigma_{int1D} = 2.1_{-2.1}^{+3.3}$  km/s recently determined by Cottaar et al. (2012) and lower than 1D proper motion dispersion  $\sigma_{int1D} = 9.2 \pm 2.5$  km/s derived by Mengel and Tacconi-Garman (2009), but agree within the uncertainty. Both these latter results were based on radial velocity (RV) measurements of the massive population of Wd 1 and are affected by small number statistics. Our astrometric observations, on the contrary, contain big amount of stars and are not biased by unresolved binarity, as both of the stellar components have a similar proper motion. Non-spherical velocity dispersion  $\sigma_{int_L} : \sigma_{int_B} = 1.8$  is in agreement with the recent results on elongation of Wd 1 along the Galactic plane (Brandner et al. 2008; Gennaro et al. 2011; Negueruela et al. 2010). Assuming an elliptical density profile for massive and intermediate mass stars in Wd 1, Gennaro et al. (2011) found an axial ratio of  $a : b = 3 : 2$ . The observed flattening and velocity anisotropy in the cluster might be caused by the rotation of Wd 1. Another reasonable explanation comes from the possible formation scenario, when two or more coeval clusters were merged into one spheroidal structure.

The slope of the initial mass function for the cluster center within  $r < 0.23$  pc and for the masses down to  $0.6 M_{\odot}$  was derived for the first time. The initial masses of the cluster members were assigned based on 5.0 Myr FRANECA-Padova isochrone at  $DM=13.0$  mag. In order to avoid binning biases a cumulative IMF was created. Our new value of IMF

### 3. THE INITIAL MASS FUNCTION AND INTERNAL DYNAMICS OF THE STARBURST CLUSTER WESTERLUND 1 FROM NEAR-INFRARED ADAPTIVE OPTICS OBSERVATIONS

---

slope is in a good agreement with the change in mass function found for Wd 1 by [Brandner et al. \(2008\)](#) (see Fig. 3.15). With  $\Gamma = -0.46$ , the slope of the stellar mass function is quite shallow in the very cluster center ( $r < 0.23$  pc), getting steeper with increasing distance center (from  $\Gamma = -0.6$  within  $r < 0.75$  pc to  $\Gamma = -1.7$  for  $r > 2.1$  pc). This indicates that massive stars are segregated in the cluster core. This result is consistent with the signs of mass segregation in other Galactic young massive clusters, like NGC 3603 YC ([Harayama et al., 2008](#)), Quintuplet ([Hußmann et al., 2011](#)) and Arches ([Stolte et al., 2002](#)). From the simulations on dynamical evolution of star clusters [Allison et al. \(2009\)](#) concluded that the observed mass segregation in young clusters need not be primordial, but could be the result of rapid and violent dynamical evolution.

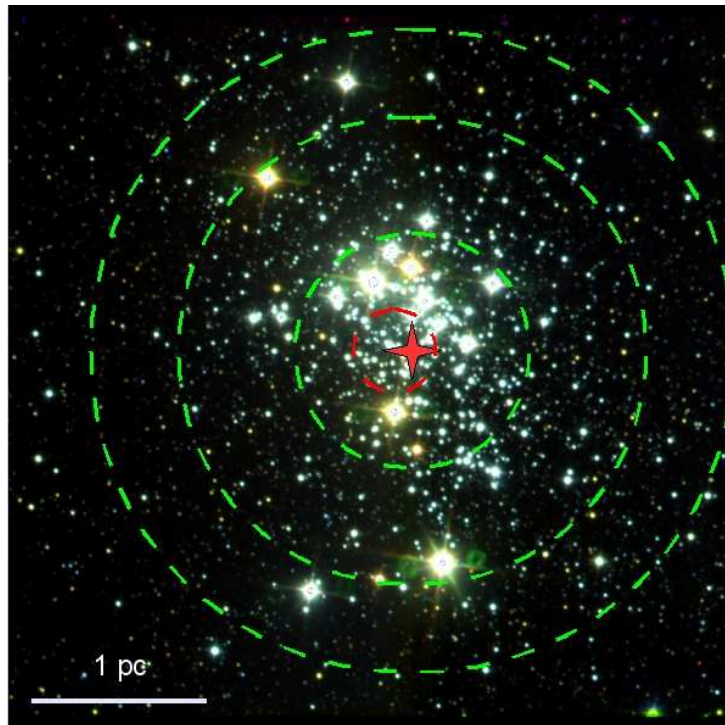


**Figure 3.14:** Composite colour  $JHK_S$  image of Wd 1. Overplotted green annuli define the areas of Wd 1 that were analysed by [Brandner et al. \(2008\)](#). Red annulus shows the region of Wd 1 that was analysed at this work. Red star defines the cluster center.

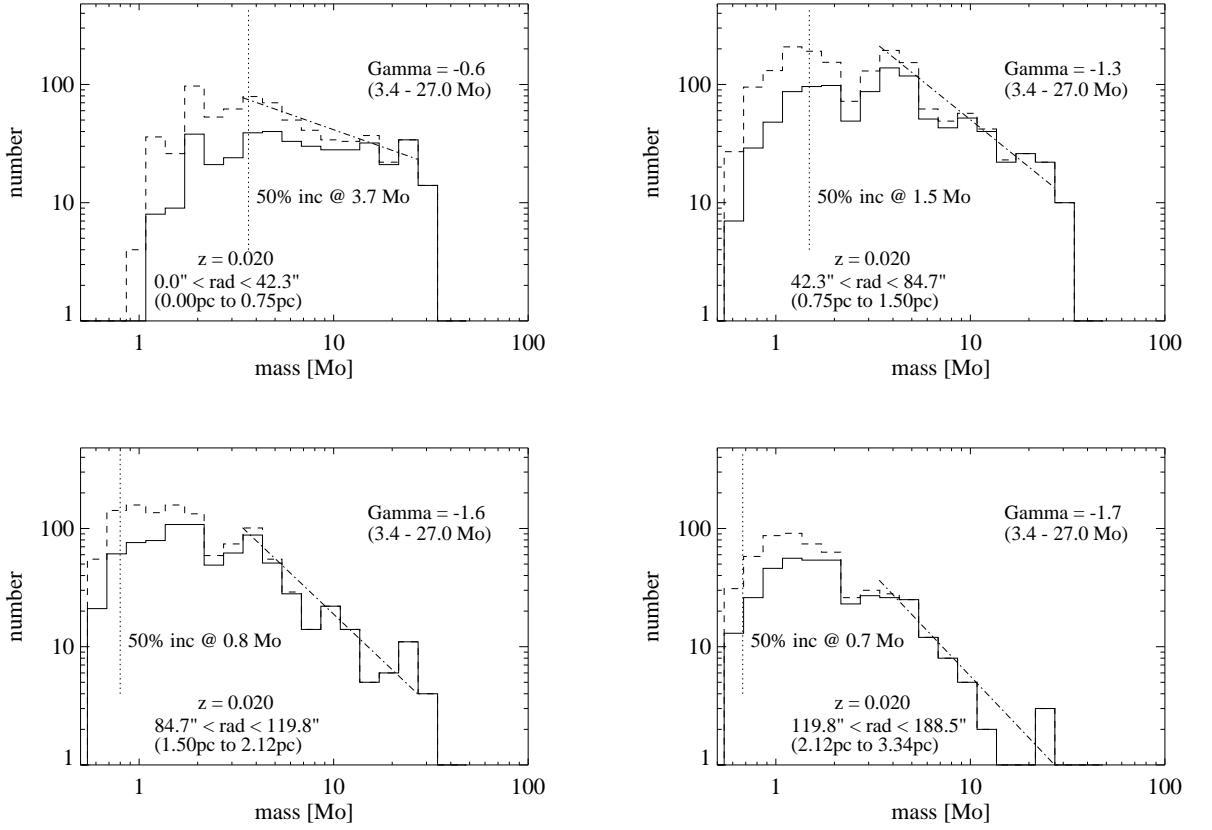


**Figure 3.15:** Mass functions of Wd 1 for 4 annuli found by [Brandner et al. \(2008\)](#) from NTT/SOFI observations. The mass determination is based on a 3.9 Myr isochrone with  $Z=0.020$  for stars with masses  $\geq 6.0 M_{\odot}$ , and on a 3.2 Myr Palla Stahler isochrone with  $Z=0.019$  for stars with masses  $< 6.0 M_{\odot}$ . The slope of the mass function (dash-dotted line is computed from stars with masses between  $3.4$  and  $27 M_{\odot}$ .)

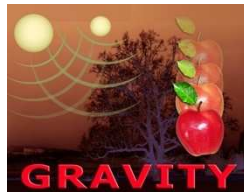
**3. THE INITIAL MASS FUNCTION AND INTERNAL DYNAMICS OF  
THE STARBURST CLUSTER WESTERLUND 1 FROM  
NEAR-INFRARED ADAPTIVE OPTICS OBSERVATIONS**

---

## 4

# Characterizing exoplanets with GRAVITY

*The 2nd generation Very Large Telescope Interferometer instrument GRAVITY aims at achieving micro-arcsecond accuracy astrometry. In a study of the GRAVITY science cases we investigate the astrometric detection of exoplanets around very low mass stars. This includes defining the actual sample of M-dwarfs to be surveyed and doing simulations to identify the best survey strategy. With GRAVITY's astrometric accuracy of  $10\mu\text{as}$ , we expect to detect planets with 4 Earth masses in a 5 years survey.*



## 4. CHARACTERIZING EXOPLANETS WITH GRAVITY

---

### 4.1 GRAVITY

GRAVITY is an adaptive optics (AO) assisted, near-infrared VLTI instrument for precision narrow-angle astrometry and interferometric phase referenced imaging of faint objects.

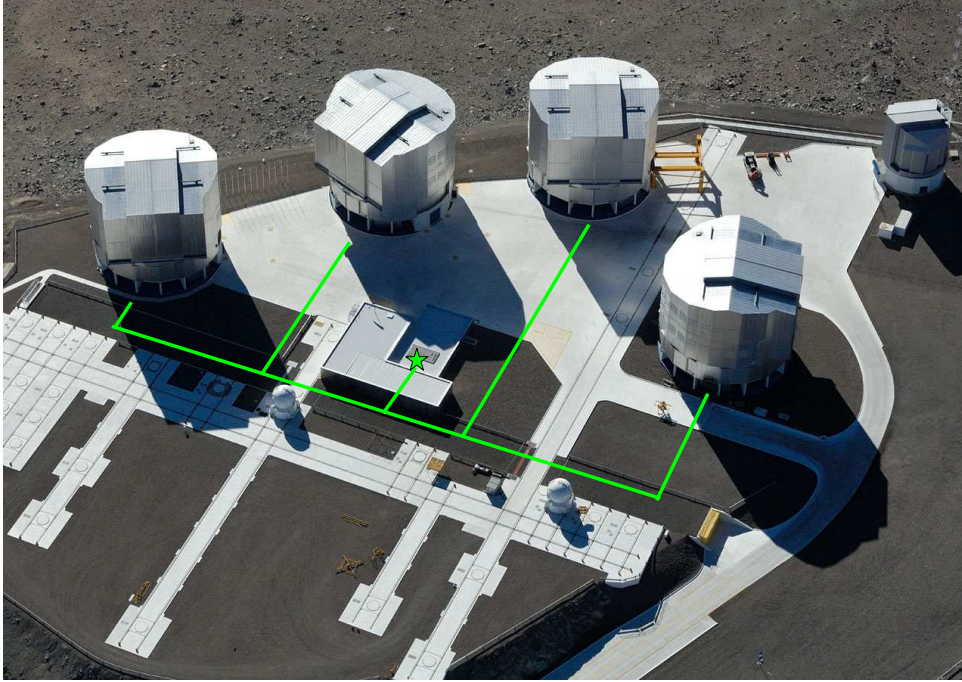


**Figure 4.1:** The VLTI at Paranal. Future location of the GRAVITY beam combiner is marked by a green star.

The instrument is developed by a Consortium of several European institutes and laboratories. This includes MPE in Garching, MPIA in Heidelberg, University of Cologne, LESIA in Paris, IPAG in Grenoble and SIM in Lisbon.

#### Core design:

- combine the light from all four Unit Telescopes (UTs) or Auxiliary Telescopes (ATs) of the VLTI, with a total collecting area of  $200\text{ m}^2$ ;
- offer narrow angle astrometry in the infrared (IR) K-band ( $2.2\ \mu\text{m}$ );
- measure simultaneously the interferograms for six baselines, with a maximum baseline of 200 meters;

- for the first time utilize a large 1.7'' field of view of the VLTI, providing simultaneous interferometry of two objects.

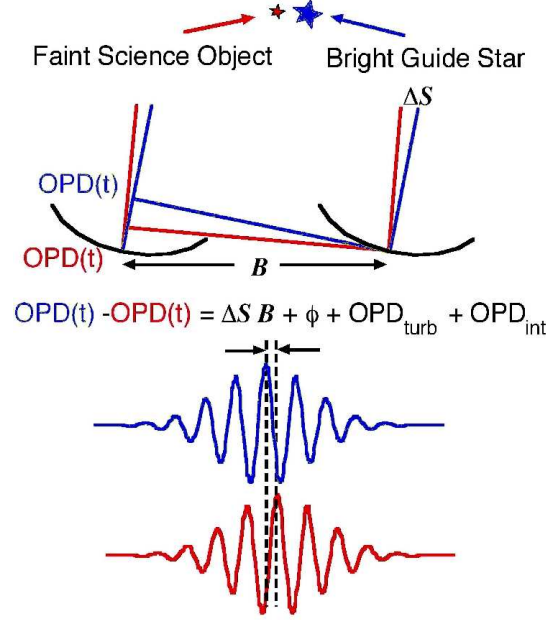


**Figure 4.2:** Principle of dual-feed interferometry. Image credit: [Delplancke \(2008\)](#)

The instrument will provide narrow-angle astrometric measurements, i.e. the position of a target object relative to a nearby reference star within the 1.7'' field of view. The difference of position of the fringe envelopes between these two objects or the difference in their optical path difference (OPD) (see Fig. 4.2) is given by the following equation ([Delplancke, 2008](#)):

$$\Delta OPD = \overline{\Delta s} \cdot \overline{B} + \phi + dOPD_{atm} + dOPD_{int}, \quad (4.1)$$

where  $\overline{\Delta s}$  is the angle vector on sky between the object (red in Fig. 4.2) and the reference star (blue in Fig. 4.2),  $\overline{B}$  is the baseline vector,  $\phi$  is the phase of the object complex visibility (or the sum of the phases of both objects if the reference is not centro-symmetric),  $dOPD_{atm}$  is the random contribution of the atmospheric turbulence,  $dOPD_{int}$  is the internal differential OPD, introduced by the interferometer. The positions of the fringe envelopes will be measured with dedicated interferometric instruments,  $dOPD_{atm}$  will be compensated by a fringe tracker (see below), and  $dOPD_{int}$  will be measured through laser metrology (see below). As a result we will have access to the two scientific observables: the angle vector between both stars projected on the baseline  $\overline{\Delta s} \cdot \overline{B}$  and the phase of the

#### 4. CHARACTERIZING EXOPLANETS WITH GRAVITY

object complex visibility  $\phi$ . As this measurement is done for six baselines simultaneously, the angle vector between both stars  $\vec{\Delta s}$  and the image can be reconstructed. The principle of narrow-angle dual-feed interferometry in detail is described in [Shao and Colavita \(1992\)](#). GRAVITY will allow narrow angle astrometry with a precision of the order of  $10\mu\text{as}$  in 5 minutes for a K=10 primary star and a K=15 secondary star at a distance of  $1''$  (UT) and for a K=7 primary star and a K=12 secondary star at a distance of  $2''$  (AT). The resulting angular resolution in the reconstructed image will be about 4 mas.

An overview of GRAVITY is shown in Fig. 4.3. The unique components will be the IR wavefront sensors, the beam-combiner instrument and the laser metrology system.

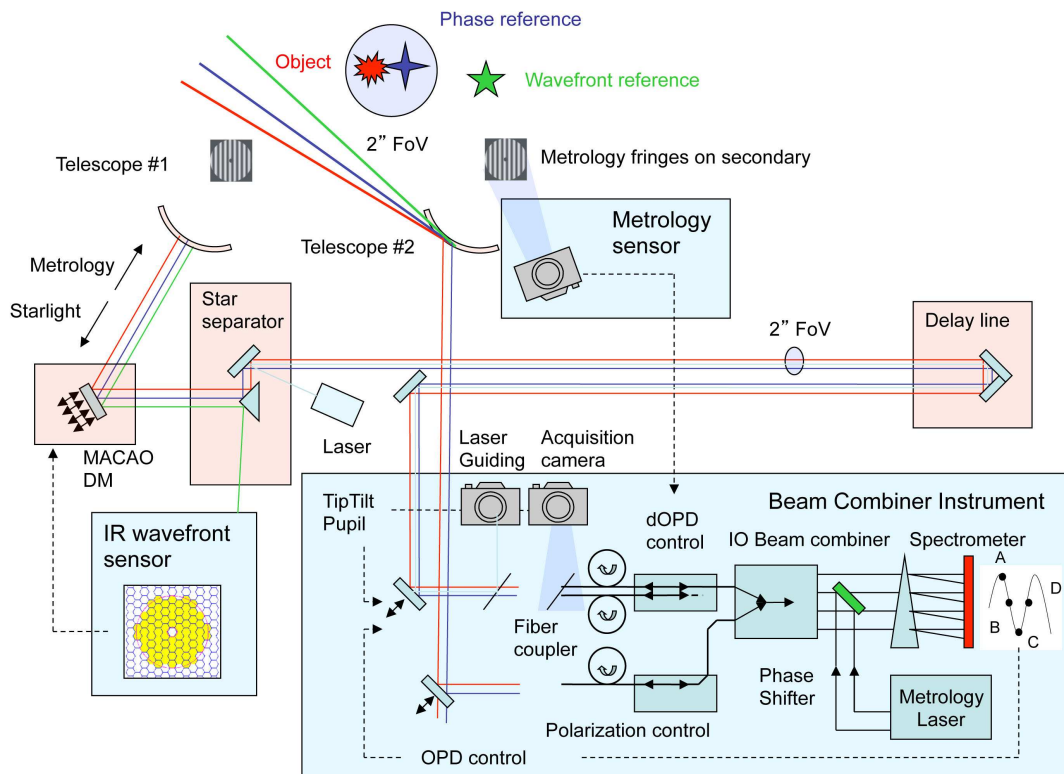


**Figure 4.3:** GRAVITY overview. Only two of 4 telescopes are shown.

The IR wavefront sensors (Fig. 4.4) ([Clénet et al., 2010](#)) will be installed in the Coudé rooms of the UTs and will command the existing MACAO deformable mirrors. They will be capable of measuring the wavefronts of four telescopes simultaneously. The bright star (green in Fig. 4.3) within a  $30''$  field of view will serve as a wavefront reference and short

exposures on it will allow measuring the atmospheric turbulence. GRAVITY will be the first interferometric instrument that will use infrared wavefront sensing for its AO.



**Figure 4.4:** H+K-band NIR wavefront sensor that will be installed on all four 8-m UTs. Image credit: A.Huber and R.Rohloff.

GRAVITY will also have the world’s first K-band integrated optics beam combiner that will provide simultaneous interferometry of two objects in a 2'' (UT) or 4'' (AT) field of view for four telescopes. Operating with 6 baselines it will provide 24 outputs for the four inputs (see Fig. 4.5).

In addition to the AO system, that will reduce the distortion of the wavefront induced by the turbulent atmosphere, GRAVITY will be equipped with a fringe tracker. This system will allow to track a piston mode. Piston mode does not affect single dish imaging instruments, but it has a serious effect on interferometry. The fringe tracker will allow to compensate for this additional phase term and piston variations due to instrumental vibrations and avoid the blurring of fringes on the detector.

For measuring the angular separation of two objects with an accuracy of  $10 \mu\text{as}$ , we need to know the differential optical path difference  $dOPD_{int}$  through the VLTI and GRAVITY with a high accuracy. Typical errors allowed are on the order of 5 nm. This will be done with a dedicated laser metrology (Bartko et al., 2010). The differential phase between the

## 4. CHARACTERIZING EXOPLANETS WITH GRAVITY

---

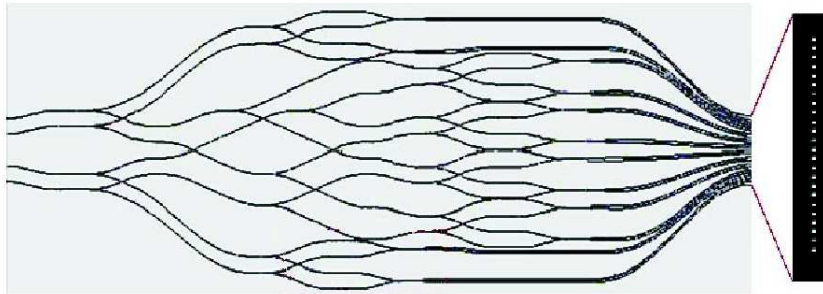


**Figure 4.5:** Beam combination principle, 6-baseline integrated optics beam combiner for the 4-telescopes.

two-object beam paths will be measured with 1 nm accuracy in only 3 minutes.

The GRAVITY project was presented for the first time to the astronomical community in 2005 during the ESO workshop on second generation VLTI instruments. At the moment the project is in its final design and the first light at the VLTI is planned for 2014.

### 4.1.1 Scientific goals

The main goal of GRAVITY is to answer the question whether or not the Galactic Centre harbors a four million solar mass black hole. This includes exploring the nature of flares in Sgr A\* and measurements on the spin of black hole. GRAVITY may even be able to test General Relativity in the presently unexplored strong field limit. All key-experiments that will become possible with GRAVITY are summarized in [Eisenhauer et al. \(2011\)](#). This includes the following science cases:

- **Galactic Center:**
  - origin of flares in Sgr A\*;
  - spin and inclination of the Galactic Center black hole;
  - paradox of youth of the Galactic Center stars;
  - the possibility of testing General Relativity in its strong field around supermassive black holes.
  
- **Active galactic nuclei (AGN):**
  - constrain the size, composition and dynamics of the core AGN structures;
  - imaging the dust and molecular torus;

## 4.2 Astrometric detection of exoplanets with GRAVITY

---

- the direct measurement of the spatial extent of the broad line region (BLR), a compact region in which gas streaming velocities reach several thousand km/s.
- **Intermediate mass black holes (IMBHs):**
  - discovering IMBHs in dense stellar clusters.
- **Masses of the most massive stars and brown dwarfs:**
  - dynamical mass estimates of the binary components;
  - probe the sub-stellar companions themselves for binarity;
  - calibrating the stellar evolutionary tracks.
- **Circumstellar disks and jets around young stars:**
  - increase the sample of observed young stars towards the poorly explored solar mass regime;
  - search for circumstellar disk disruptions signatures;
  - probe the presence of hot, young sub-stellar and planetary companions;
  - reveal the disk structure evolution;
  - resolve the central jet formation engine around young, nearby stars;
  - put constraints on jet formation models and the role of magnetic fields.
- **Astrometric detection of exoplanets:**
  - This important science case is described in detail in Section [4.2](#).

GRAVITY will increase substantially the range and number of astronomical objects that can be studied with the VLTI.

## 4.2 Astrometric detection of exoplanets with GRAVITY

### 4.2.1 Introduction

The first exoplanet was found in 1988 by [Campbell et al. \(1988\)](#) around the Gamma Cephei star. However, astronomers remained sceptical about this discovery for many years and only in 2003 the existence of the exoplanet around Gamma Cephei was proved ([Hatzes et al., 2003](#)) via radial velocity (RV) method. The first confirmed detection of a planet outside our solar system was made in 1992 ([Wolszczan and Frail, 1992](#)) around the pulsar PSR1257+12. As pulsars represent the most precise natural clocks in the Universe, irregular pulses from PSR1257+12 indicated the presence of at least one planet in the

#### 4. CHARACTERIZING EXOPLANETS WITH GRAVITY

---

system. However, as of April 2012, only 2% of the known exoplanets were detected via pulsar timing measurements (see Fig. 4.6). Most of the exoplanets were detected via the RV method (62%) and the transit method (30%) and only few by microlensing (2%), direct imaging (4%) and pulsar timing (2%), and none so far by astrometry.

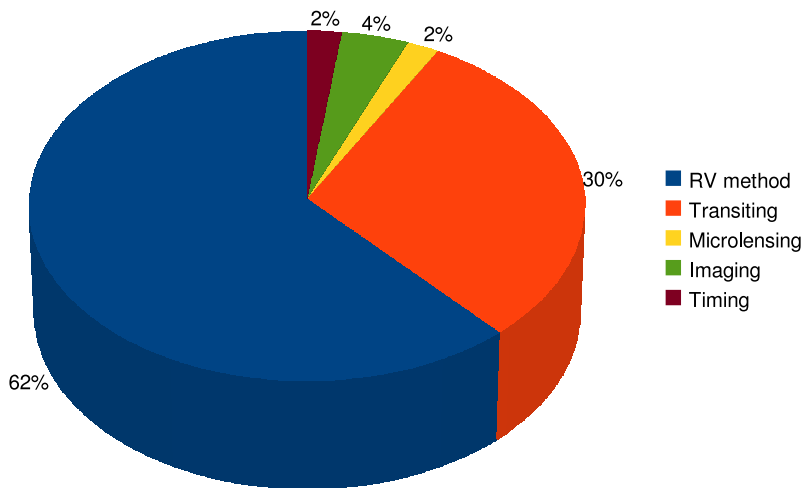


**Figure 4.6:** Number of exoplanets (in percentage) detected via different methods.

One of the main disadvantages of the RV method is that it can give us only a lower-limit on the planet’s mass estimation. Both the star and the planet orbit their common center of gravity with the same period, and with velocities and semi-major axis inversely proportional to their mass ratios. By measuring the projected displacement  $\theta$  of a star due to a planet (see Fig. 4.7) via astrometry we can unambiguously determine a planet mass and its full three-dimensional orbit. Measuring a planet’s mass is crucial for deriving the density and chemical composition of a planet and hence its potentiality for habitability. In contrast to the RV method, which is sensitive to close-in planets with short periods, astrometry is more sensitive to planets in wide orbits with longer periods. RV method, though, cannot derive the inclination of an orbit. [Tuomi et al. \(2009\)](#) shows the complementarity of astrometric and RV observations. It is commonly assumed that to be able to detect a signature of a planetary companion, an observational timeline longer than the orbital period is required. However, when high-precision RV and accurate astrometric measurements are both available, the orbital parameters and planetary mass could be accessible within only one fourth of the orbital period. The ability to use RV and astrometric measurements simultaneously will considerably increase the efficiency of observations. Prior astrometric observations will also improve the science yield of a mission to image exoplanets. As shown in [Shao et al. \(2010\)](#), given an orbital solution from a prior astro-

metric mission will lead to an inevitable detection of a planet via direct imaging and will gain coronagraph efficiency, more targets will be observed in the same mission time.

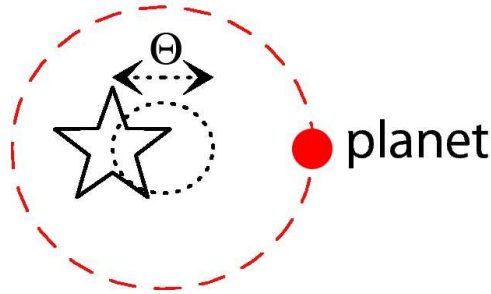


Figure 4.7: Displacement of the star due to a planet.

So far no planet has been discovered via astrometry, as this technique requires extremely high accurate observations. For example, the displacement  $\theta$  of a solar mass star at a distance of 10 pc due to a Jupiter-mass planet at 10 AU separation is only 1 mas. A number of astrometric missions have been proposed and planned for the next decade (see Table 4.1). These include ground-based instruments, like PRIMA (ESO) at the VLTI or ASTRA (NSF/NASA) on the Keck Interferometer, both with  $50 \mu\text{as}$  accuracy, as well as space-borne astrometric missions like GAIA (ESA) with expected astrometric precision of  $24 \mu\text{as}$ . The 2nd generation VLTI instrument GRAVITY will open a new window in a range of planet masses that can be discovered via astrometry.

#### 4.2.2 GRAVITY astrometric capability

About 70% of all the stars in our galaxy are comprised of M-type dwarf stars. These are low mass stars with masses ranging from  $0.5M_{\odot}$  down to  $0.08M_{\odot}$  and surface temperature of less than 4000 K. These stars fuse hydrogen to helium via the direct proton-proton chain, a slow rate mechanism that resulted in a low luminosity of M dwarfs. Because of their low intrinsic luminosity, only 8% of all known exoplanets were found around M dwarfs. Such optically faint stars are also difficult to observe with space-based astrometric missions. The extremely high light gathering power of all four 8-meter UTs of the VLTI and astrometric capability of  $10 \mu\text{as}$  make GRAVITY an ideal instrument for the detection of very low mass planets around late-type M dwarfs. Fig. 4.8 shows the astrometric capability of GRAVITY (blue) of exoplanet detection around M7.5 dwarf star at a distance of 6 pc as compared to RV measurements by HARPS (red) and SPHERE direct imaging (green). In this plot we assume the minimum astrometric signal of  $50 \mu\text{as}$  of the host star, 8.2 m/s RV accuracy of HARPS for this star and SPHERE limits of 1 Jupiter-mass planet at separation of  $0.1''$ . As RV and astrometric methods working separately require

#### 4. CHARACTERIZING EXOPLANETS WITH GRAVITY

observational periods exceeding the orbital period to produce positive results, the right edges of the blue and red zones in Fig. 4.8 correspond to observational time limit of 20 years.

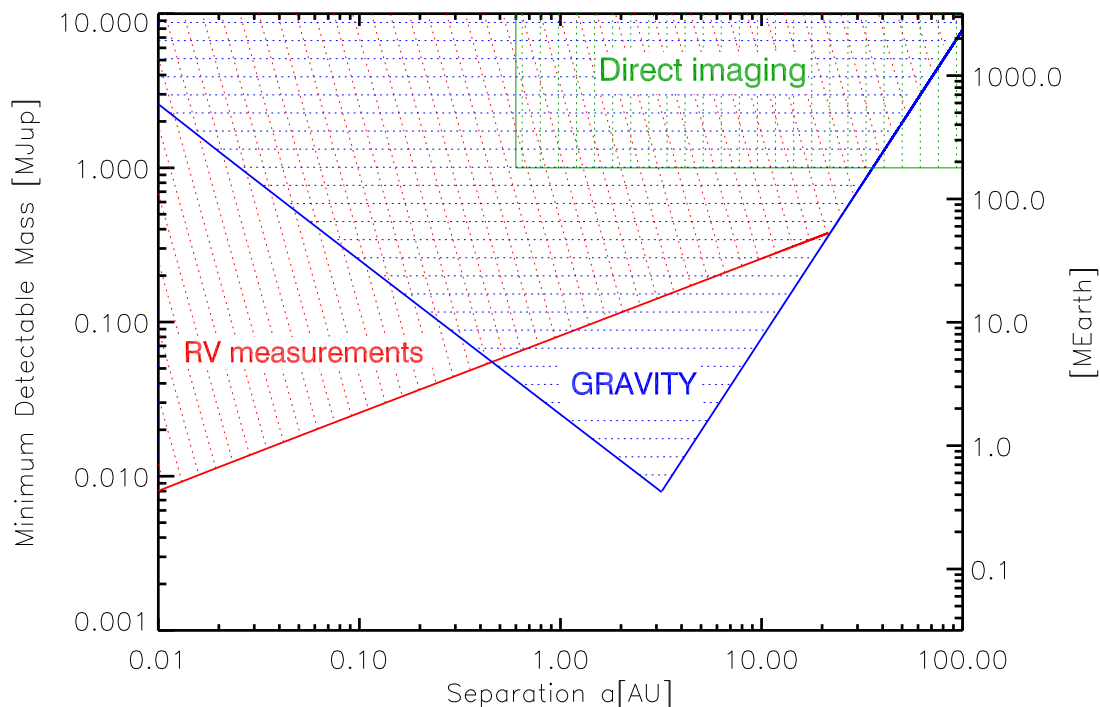


**Figure 4.8:** GRAVITY astrometric capabilities as compared to radial velocities measurements by HARPS and SPHERE direct imaging. Blue zone corresponds to GRAVITY exoplanet detection capabilities around M7.5 dwarf star at a distance of 6 parsec.

In case of a circular orbit displacement of the star due to a planet over the full orbit is given by:

$$\theta = 20.5 \mu as \left( \frac{M_{planet}}{4M_{Earth}} \right) \left( \frac{d}{5pc} \right)^{-1} \left( \frac{\tau}{5yr} \right)^{2/3} \left( \frac{M_{star}}{0.2M_{Sun}} \right)^{-2/3} \quad (4.2)$$

where  $d$  is the distance to the system in parsecs,  $\tau$  is the orbital period of the planet in years,  $M_{star}$  is the mass of the host star in solar masses and  $M_{planet}$  is the planet mass in Earth masses. With GRAVITY we expect to detect planets of 2-3 Earth masses around M5 dwarfs within 10 pc. Maximum distance for an early type M0V star in order to detect the astrometric signature of a 4.2 Jupiter-mass planet at 5 AU with GRAVITY will be 780 pc.

	Astrometric project	Availability	Accuracy	Wavelength, Limiting magnitude	Exoplanet targets
	<b>HST/FGS</b> (NASA/ ESA/ STScI)	since 1990	1-2 mas	optical, ultraviolet, near-infrared $m_v \leq 17$ mag	<ul style="list-style-type: none"> <li>• Known radial velocity-planets</li> </ul>
	<b>GAIA</b> (ESA)	2013	$24 \mu\text{as}$	optical, $m_v \leq 20$ mag	<ul style="list-style-type: none"> <li>• Habitable Earth-size planets around solar type stars brighter than <math>m_v = 12</math> mag within 200 pc from the Sun;</li> <li>• Jupiter-mass planets around all stars within 50 pc from the Sun</li> </ul>
	<b>VLTI/PRIMA</b> (ESO)	2012	$50 \mu\text{as}$	near-infrared $m_k \leq 14$ mag	<ul style="list-style-type: none"> <li>• Known radial velocity-planets within 200 pc from the Sun;</li> <li>• Low-mass planets around nearby stars of any spectral type within 15 pc from the Sun;</li> <li>• Massive planets orbiting young stars within 100 pc from the Sun</li> </ul>
	<b>VLTI/GRAVITY</b> (ESO)	2014	$12 \mu\text{as}$	near-infrared $m_k \leq 15$ mag <sup>a</sup>	<ul style="list-style-type: none"> <li>• Earth-like planets with <math>2-3 M_{Earth}</math> around M-dwarfs within 25 pc from the Sun;</li> <li>• Known radial velocity-planets within 200 pc from the Sun;</li> <li>• Exoplanetary systems around G-type stars within 200 pc from the Sun</li> </ul>

Table 4.1: Planet-hunting astrometric missions

<sup>a</sup>the magnitude of the science object when a bright reference source of  $m_k \sim 10$  is found within  $2''$  field of view of GRAVITY

## 4. CHARACTERIZING EXOPLANETS WITH GRAVITY

---

### 4.2.3 Observing strategy

For detecting exoplanets with GRAVITY we assume a 2 year survey program. Each star will be observed 5 times during the first year with a total exposure time of one hour per target. After the first year survey, the stars that will show a wobble in their position, will be selected as candidates for a second year survey. After 10 observations of such target within 2 years we plan to completely determine an object's orbit and estimate the mass of a planet. As a preliminary observation, precise radial velocity measurements of all our targets will be made. It is necessary to ensure that the star has no stellar or substellar companions or starspots that could impact the astrometry. These astrophysical effects have already been studied by several authors (e.g., [Makarov et al. \(2009\)](#), [Eriksson and Lindgren \(2007\)](#)) and it was shown that in general they have a smaller impact on astrometry compare to RV measurements.

GRAVITY will measure relative astrometry. Thus, after detecting astrometric signature we will need additional RV observations to solve a problem of ambiguity on which of the two stars in the observed pair hosts the planet.

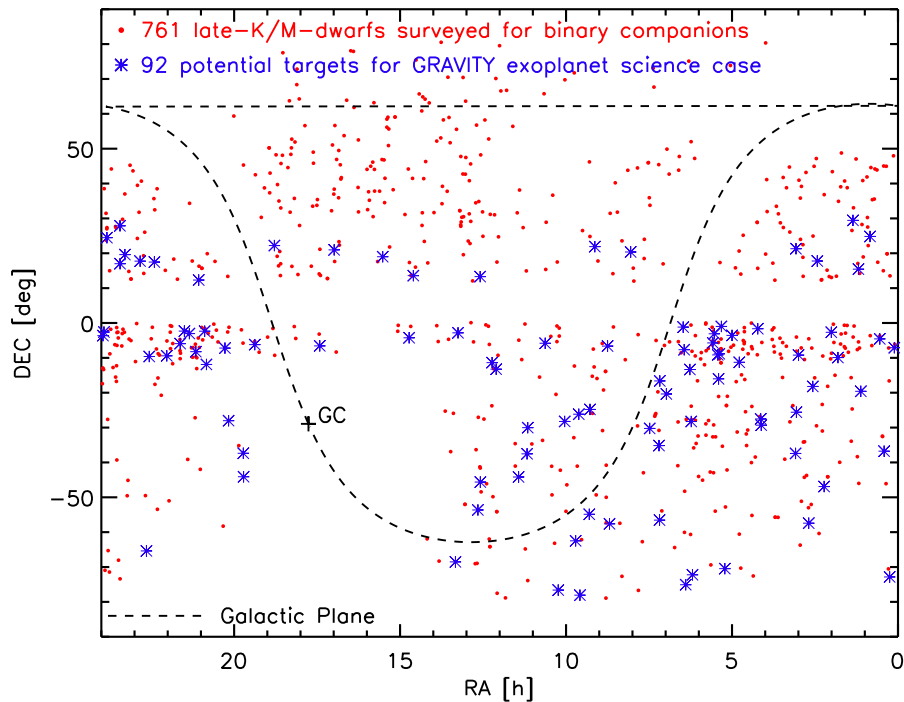
### 4.2.4 Target list

Narrow-angle astrometry as well as phase-referenced imaging of faint objects rely on the existence of reference stars around the target object within the same field of view. As the effective field of view of GRAVITY will be  $d \sim 1.7''$ , we should select the binaries with the angular separation less than  $d$ . Signal-to-noise ratio sets a natural magnitude limit to the reference star that can be used for observations with GRAVITY. The minimum K-band brightness for a reference star required to reach  $10\mu\text{as}$  accuracy is  $K \sim 10$  mag. In order to observe the planets in stable orbits we should take into account the orbital stability criteria for planets in stellar binary systems. The criteria was found to depend on the mass ratio between the stellar components and the distance ratio  $\frac{a_{\text{planet}}}{a_{\text{binary}}}$  ([Cuntz et al., 2007](#)). The planets that have a distance ratio less than 0.25 belong to the domain of orbital stability, where the perturbation of the binary will not disturb the planet's orbit and at the same time where the planet is secured from leaving the system entirely or from being captured by the other stellar components.

For our GRAVITY sample selection we choose M-dwarf binaries with the angular separation less than  $1.7''$ . Our targets are all selected to be physical binaries, and hence share the same angular parallax and proper motion. Thus unlike in the case of PRIMA observations, we do not need to solve for or measure absolute parallax and proper motion. Table 4.2 presents a preliminary list of 5 such targets at a distance within 25 pc. Several targets are bright enough for observation with the ATs ( $K < 7$  for the primary and  $K < 12$  for the secondary). The other targets are too faint to be observed with ATs but both

## 4.2 Astrometric detection of exoplanets with GRAVITY

components of these 5 targets are bright enough for fringe tracking with the UTs. Due to the low luminosity of M dwarfs, there is a large uncertainty in their physical properties and multiplicity fraction. However, recent Lucky Imaging survey at the ESO 3.5 m New Technology Telescope (NTT) and the Calar Alto 2.2 m telescope (Bergfors et al. 2010; Janson et al. 2012) has considerably increased our knowledge about M dwarfs. In the observed sample of 701 M dwarfs and 60 late K-type stars, 182 new and 37 previously known companions were detected in 205 systems. The sample of AstraLux M dwarf binaries suitable for observations with GRAVITY is presented in Table 4.4 in the Appendix. These are 92 candidates, among of which 38 are still unconfirmed physical binaries, as common proper motions have yet to be confirmed. Fig. 4.9 shows the distribution on the sky of the AstraLux late-K and M dwarf sample, as well as selected 92 potential GRAVITY targets. The targets have a good all-sky distribution, and only few of them are located near the Galactic Center. As can be seen from Fig. 4.10, around 60% of all potential GRAVITY targets have primary masses below  $0.3 M_{star}$ . Such small stars will allow the detection of 10-20 Earth mass planets around them. The observations of later type M dwarfs (from M6 to M9) with AstraLux have already been started in January 2012. These observations will give an opportunity to find potential targets for the detection of exo-Earthes.



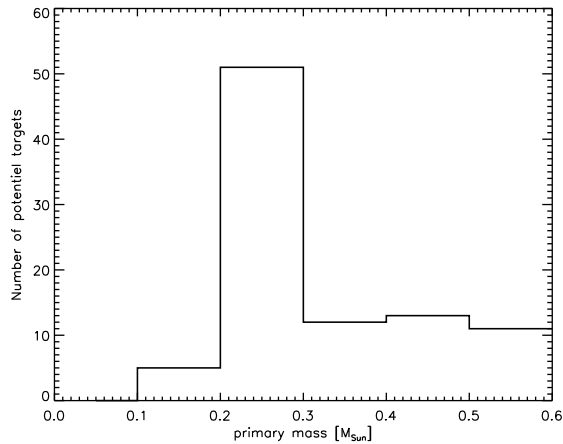
**Figure 4.9:** AstraLux Large M-dwarf multiplicity survey. Courtesy of W.Brandner.

Table 4.2: M-dwarf targets

Name	RA	DEC	Distance, pc	Spectral type	$m_k$ , mag	Separation, arcsec	Period, yr	Mass, $M_\odot$
NS 0728-3014 GJ 2060 Primary Secondary	07h28m51.38s	-30d14m49.06s	15.6±0.6	M0.5 M1.5	6.27 6.71	0.175	6±1	0.59±0.05 0.52±0.08
2M1036BC Primary Secondary	10h36m44.79s	15d21m39.6s	19.6±4.6	M4.5 M4.5	9.60 9.60	0.189	16±9	0.16±0.05 0.16±0.05
LP 642-48 Primary Secondary	23h20m57.50s	-01d47m37s	22.6±6.7	M4.0 M4.0	9.12 9.39	0.099	6±3	0.25±0.18 0.21±0.17
GJ 234 Ross 614 Primary Secondary	06h29m23.4s	-02d48m50s	4.09±0.03	M4.5 M8	5.49 9.17	1.101	16.60±0.01	0.22±0.01 0.11±0.01
GJ 1005 L 722-22 Primary Secondary	00h15m 28.1s	-16d08m02s	5.0±0.23	M4 M6	7.10 9.02	0.304	4.57±0.01	0.18 0.11

### 4.3 Transiting exoplanet detection capabilities of GRAVITY

---



**Figure 4.10:** Histogram of the mass distribution of the M dwarf GRAVITY potential targets.

The next interesting group of targets is binary stars with known exoplanets 200 pc from the Sun. The RV method gives only a lower limit on a planet mass and precise astrometric observations are required to get all orbital parameters and a true planet mass. List of such targets, suitable for observations with GRAVITY is presented in Table 4.3.

### 4.3 Transiting exoplanet detection capabilities of GRAVITY

The GRAVITY instrument will give a great opportunity to observe transiting exoplanets. The transit of a planet in front of its parent star causes an apparent motion of the photocenter of the star. For a dwarf star of  $1 R_{\odot}$  with an apparent angular diameter of 2 mas (i.e. located within  $\sim 4$  pc), the sensitivity of GRAVITY will be such that the transit of an exoplanet covering only 0.5% of the apparent disk of the star (Saturn-size planet) will be detectable. This type of measurement will give the orbit spin orientation. It might also yield dependence of astrometric signal via wavelength, and hence in addition provide information of the atmospheric properties of the planet or surface properties of the star.

The orbit orientation combined with measurements of the degree of polarization of light reflected by the planet (e.g. SPHERE ZIMPOL observations), will give an opportunity to place constraints on the distribution of clouds and weather zones on the planet.

Thus in combination with present-day and future extrasolar planet search programs, GRAVITY will improve our understanding of the statistical properties of the extrasolar planets and collect interesting targets for future spectroscopic characterization of habitable planets around nearby stars.

Table 4.3: Binary stars with known exoplanets

Name	RA	DEC	Distance, pc	Spectral type	m, mag	Separation, arcsec	$\theta$ from Eq.(4.2), $\mu\text{as}$	Ref., notes
Gliese 86 A B	02h10m24.00s	-50d49m31.13s	10.9	K1 V WD	4.12(K) 13.7(K)	1.93	$\geq 50$	Raghavan et al. (2006), Els et al. (2001)
HD 196885 A B	20h39m51.85s	+11d14m58.01s	33	F8 IV M1 V	5.07(K) 8.17(K)	0.71	$\geq 167$	Chauvin et al. (2007)
HD 41004 A B	05h59m49.69s	-48d14m23.46s	43	K1 IV M2.5 V	6.43(K) 12.33(V)	0.5	$\geq 140$	*triple star Raghavan et al. (2006)
HD 177830 A B	19h05m20.80s	+25d55m14.83s	59	K0 M2-M5	4.8(K) 11.2(K)	1.6	$\geq 20$	Eggenberger et al. (2007)
HD 126614 A B	14h26m48.37s	-05d10m38.71s	72.4	K0 V M V	7.06(K) 11.04(K)	0.5	$\geq 10$	Howard et al. (2010)

## 4.4 Appendix

**Table 4.4:** Targets from the AstraLux M-dwarf multiplicity survey suitable for observations with GRAVITY

2MASS ID	$SpT_A$	$SpT_B$	$m_A, [M_\odot]$	$m_B, [M_\odot]$	$\rho, ['']$
J00063925-0705354AB	M3.0	M4.5	0.290	0.175	$0.250 \pm 0.001$
J00150240-7250326AB	M0.5	M3.5	0.565	0.245	$0.290 \pm 0.009$
J00250428-3646176AB	M2.5	M5.0	0.355	0.150	$0.605 \pm 0.012$
J00325313-0434068AB	M3.5	M6.0	0.245	0.120	$0.428 \pm 0.006$
J00503319+2449009AB	M3.5	M4.5	0.245	0.175	$1.320 \pm 0.001$
J01071194-1935359AB	M1.0	M2.0	0.540	0.420	$0.426 \pm 0.002$
J01112542+1526214AB	M5.0	M6.0	0.150	0.120	$0.293 \pm 0.002$
J01212520+2926143AB	M3.5	M4.0	0.245	0.200	$0.260 \pm 0.001$
J01483524-0955226AB	M4.0	M4.5	0.200	0.175	$0.485 \pm 0.001$
J02002975-0239579AB *	M3.5	M4.5	0.245	0.175	$0.323 \pm 0.001$
J02133021-4654505AB	M4.0	M5.0	0.200	0.150	$0.138 \pm 0.005$
J02255447+1746467AB	M4.0	M5.0	0.200	0.150	$0.099 \pm 0.001$
J02335984-1811525AB *	M3.0	M3.0	0.290	0.290	$0.839 \pm 0.006$
J02411909-5725185AB *	M3.0	M4.5	0.290	0.175	$1.504 \pm 0.007$
J02594789-0913109AB	M4.5	M9.5	0.175	0.083	$0.595 \pm 0.008$
J03033668-2535329AB	M0.0	M3.5	0.590	0.245	$0.823 \pm 0.003$
J03042184+2118154AB *	M1.0	M5.0	0.540	0.150	$0.401 \pm 0.001$
J03050976-3725058AB *	M2.0	M3.5	0.420	0.245	$0.229 \pm 0.005$
J04071148-2918342AB	M0.0	M3.5	0.590	0.245	$0.313 \pm 0.003$
Continued on next page					

\* unconfirmed physical binary, since the companion has not yet been tested for common proper motion

#### 4. CHARACTERIZING EXOPLANETS WITH GRAVITY

Table 4.4 – continued from previous page

2MASS ID	$SpT_A$	$SpT_B$	$m_A, [M_\odot]$	$m_B, [M_\odot]$	$\rho, ["]$
J04080543-2731349AB	M3.5	M4.5	0.245	0.175	0.221±0.003
J04132663-0139211AB	M4.0	M5.5	0.200	0.135	0.759±0.003
J04465175-1116476AB *	M3.0	M3.5	0.290	0.245	1.497±0.002
J04595855-0333123AB	M4.0	M5.5	0.200	0.135	0.141±0.001
J05130132-7027418AB *	M3.5	M5.5	0.245	0.135	1.665±0.006
J05191382-0059423AB	M2.5	M3.0	0.355	0.290	1.151±0.002
J05225705-0850119AB*	M2.0	M2.5	0.420	0.355	0.682±0.001
J05241914-1601153AB	M4.5	M5.0	0.175	0.150	0.613±0.001
J05254166-0909123AB	M3.5	M4.0	0.245	0.200	0.645±0.001
J05320450-0305291AB	M2.0	M3.5	0.420	0.245	0.216±0.003
J05343767-0543044AB *	M2.5	M4.0	0.355	0.200	1.437±0.001
J06112997-7213388AB *	M4.0	M5.0	0.200	0.150	0.164±0.002
J06134171-2815173AB *	M3.5	M3.5	0.245	0.245	1.056±0.003
J06161032-1320422AB	M3.5	M5.0	0.245	0.150	0.194±0.008
J06234024-7504327AB *	M3.5	M5.0	0.245	0.150	0.566±0.005
J06262932-0739540AB *	M1.0	M2.0	0.540	0.420	0.465±0.002
J06281861-0110504AB *	M2.0	M2.0	0.420	0.420	1.432±0.001
J06583980-2021526AB *	M4.0	M4.0	0.200	0.200	1.445±0.004
J07102991-1637350AB	M2.5	M4.0	0.355	0.200	0.558±0.003
J07105990-5632596AB	M1.5	M4.0	0.480	0.200	1.119±0.002
J07115917-3510157AB *	M3.0	M3.0	0.290	0.290	1.029±0.006
Continued on next page					

\* unconfirmed physical binary, since the companion has not yet been tested for common proper motion

Table 4.4 – continued from previous page

2MASS ID	$SpT_A$	$SpT_B$	$m_A, [M_\odot]$	$m_B, [M_\odot]$	$\rho, ['']$
J07285137-3014490AB	M1.5	M3.5	0.480	0.245	0.464±0.001
J08031018+2022154AB	M3.0	M4.0	0.290	0.200	0.200±0.002
J08412528-5736021AB *	M3.0	M3.0	0.290	0.290	1.467±0.001
J08445566-0637259AB	M3.0	M3.5	0.290	0.245	0.276±0.007
J09075823+2154111AB	M2.0	M3.5	0.420	0.245	0.107±0.001
J09164398-2447428AB *	M0.5	M2.5	0.565	0.355	0.076±0.012
J09180165-5452332AB *	M4.0	M5.0	0.200	0.150	0.486±0.001
J09345604-7804193AB	M3.0	M4.5	0.290	0.175	0.431±0.005
J09365782-2610111AB *	M4.0	M4.5	0.200	0.175	0.389±0.004
J09423823-6229028AB *	M3.5	M3.5	0.245	0.245	1.288±0.004
J10023100-2814280AB *	M4.0	M6.0	0.200	0.120	0.559±0.004
J10140807-7636327AB	M4.0	M5.5	0.200	0.135	0.226±0.002
J10374401-0548577AB	M2.5	M5.0	0.355	0.150	0.514±0.001
J11091380-3001398AB	M1.5	M3.0	0.480	0.290	0.436±0.001
J11102788-3731520AB	M4.0	M4.5	0.200	0.175	1.523±0.001
J11254754-4410267AB	M4.0	M4.5	0.200	0.175	0.553±0.003
J12062214-1314559AB *	M3.5	M5.5	0.245	0.135	0.420±0.003
J12134173-1122405AB *	M1.5	M3.5	0.480	0.245	1.296±0.002
J12345629-4538075AB *	M2.5	M3.0	0.355	0.290	0.616±0.001
J12351726+1318054AB	M6.0	M6.5	0.120	0.115	0.332±0.001
J12392104-5337579AB *	M2.5	M2.5	0.355	0.355	1.455±0.001
Continued on next page					

\* unconfirmed physical binary, since the companion has not yet been tested for common proper motion

#### 4. CHARACTERIZING EXOPLANETS WITH GRAVITY

---

Table 4.4 – continued from previous page

2MASS ID	$SpT_A$	$SpT_B$	$m_A, [M_\odot]$	$m_B, [M_\odot]$	$\rho, ["]$
J13151846-0249516AB *	M3.5	M4.5	0.245	0.175	0.215±0.002
J13195689-6831142AB *	M1.5	M4.0	0.480	0.200	0.878±0.002
J14360274+1334484AB	M2.5	M2.5	0.355	0.355	1.194±0.002
J14433804-0414354AB *	M2.0	M2.5	0.420	0.355	0.965±0.001
J15312428+1900268AB	M2.5	M5.5	0.355	0.135	0.517±0.001
J16590962+2058160AB	M3.0	M4.0	0.290	0.200	0.689±0.001
J17250940-0633536AB	M0.5	M2.5	0.565	0.355	0.437±0.001
J18471129+2212413AB	M3.5	M4.5	0.245	0.175	0.371±0.001
J19224005-0612076AB	M2.5	M4.0	0.355	0.200	0.146±0.001
J19425324-4406278AB *	M3.5	M4.5	0.245	0.175	0.836±0.002
J19432464-3722108AB *	M3.5	M6.0	0.245	0.120	1.623±0.004
J20100002-2801410AB *	M2.5	M3.5	0.355	0.245	0.615±0.001
J20163382-0711456AB *	M0.0	M2.0	0.590	0.420	0.107±0.007
J20500010-1154092AB *	M3.5	M4.5	0.245	0.175	0.459±0.007
J20531465-0221218AB	M3.0	M4.0	0.290	0.200	0.086±0.002
J21035992+1218570AB	M3.5	M3.5	0.245	0.245	0.836±0.005
J21091375-0814041AB *	M1.5	M2.5	0.480	0.355	0.973±0.002
J21205172-0301545AB *	M4.0	M4.5	0.200	0.175	1.305±0.002
J21295166-0220070AB *	M0.0	M3.5	0.590	0.245	0.719±0.001
J21372900-0555082AB	M3.0	M3.5	0.290	0.245	0.222±0.001
J22014336-0925139AB *	M1.5	M2.0	0.480	0.420	0.930±0.002
Continued on next page					

---

\* unconfirmed physical binary, since the companion has not yet been tested for common proper motion

Table 4.4 – continued from previous page

2MASS ID	$SpT_A$	$SpT_B$	$m_A, [M_\odot]$	$m_B, [M_\odot]$	$\rho, ['']$
J22240821+1728466AB	M4.0	M5.0	0.200	0.150	0.146±0.007
J22332264-0936537AB	M2.5	M3.0	0.355	0.290	1.547±0.002
J22382974-6522423AB	M3.5	M3.5	0.245	0.245	0.842±0.001
J22495622+1744414AB	M0.0	M3.0	0.590	0.290	0.117±0.004
J23172807+1936469AB	M3.0	M4.5	0.290	0.175	0.293±0.001
J23261182+1700082AB	M4.5	M6.0	0.175	0.120	0.195±0.002
J23261707+2752034AB *	M3.0	M3.5	0.290	0.245	0.151±0.001
J23495365+2427493AB	M3.5	M4.5	0.245	0.175	0.131±0.001
J23551649-0235417AB	M4.0	M4.5	0.200	0.175	0.694±0.001
J23570417-0337559AB	M4.0	M5.5	0.200	0.135	0.191±0.001

\* unconfirmed physical binary, since the companion has not yet been tested for common proper motion

#### 4. CHARACTERIZING EXOPLANETS WITH GRAVITY

---

## 5

# Conclusions

Astrometric data are of great scientific and practical importance for all areas of astronomy, astrophysics and cosmology. A variety of astronomical problems can be addressed using astrometric methods, including the structure and dynamics of the Milky Way, the cosmic distance ladder, or tests of the validity of the theory of general relativity. In this thesis we focus on present and future activities in the astrometry domain from ground-based and space observations. Special attention is given to the application of astrometric data to the study of exoplanets and starburst clusters.

### 5.1 Results on starburst clusters

Chapter 2 deals with the formation scenario of two of the most populous galactic clusters Westerlund 1 (Wd 1) and NGC 3603 YC, with masses  $5 \cdot 10^4 M_{\odot}$  and  $1.3 \cdot 10^4 M_{\odot}$  and half-mass radii 1 pc and 0.5 pc, respectively. The formation of such compact and massive clusters is still an open astrophysical problem. We used the age spread of a cluster's stellar population as an indicator of the overall duration of the star formation process in the cluster. From multi-epoch optical and near-infrared high-angular resolution HST and adaptive optics (AO) observations kinematic cluster membership was determined. For the  $\sim 5$  Myr old starburst cluster Wd 1 and  $\sim 2$  Myr old starburst cluster NGC 3603 YC we derived upper limits for the age spreads of 0.4 and 0.1 Myr, respectively. Our results suggest a single event for starburst cluster formation, in contradiction to previous claims that star formation in young massive clusters might have been ongoing for several 10 Myr. Our conclusions can be summarized in more detail as follows.

- The AO NAOS/CONICA observations of Wd 1 and high-angular resolution HST observations of NGC 3603 YC allowed to resolve the stars with masses below  $0.3 M_{\odot}$  in each cluster;

## 5. CONCLUSIONS

---

- The accurate proper motion measurements of stars in the central region of Wd 1, based on two epochs of VLT/NACO and HST/WFC3 observations separated by 7.3 years represent the powerful tool to discriminate between cluster members and field stars in the spiral arms;
- To take into account the effect of crowding, completeness simulations have been done. The 50% completeness limit for Wd1 is reached at  $K_S = 19.9$  mag, for NGC 3603 YC at  $m_{F555W} = 20.1$  mag;
- A new two-step method to determine the age spread of resolved stellar populations in young, massive cluster is developed. The Bayesian method of [Jørgensen and Lindgren \(2005\)](#) was modified both by taking into account the cluster membership probability and by adjusting the mass function by a completeness factor;
- To overcome both observational and theoretical biases we analysed the influence of unresolved binarity, photometric error and ongoing accretion on our result;
- Maximum age spread of 0.4 Myr for Wd 1 and 0.1 Myr for NGC 3603 YC is a strong indication that in both cases the clusters formed in a single event once a sufficient gas mass had been aggregated and compressed to overcome internal thermal, turbulent or magnetic support, and to initiate an avalanche-like star formation event.

Chapter 3 deals with the formation, evolution and internal dynamics of the  $\sim 5$  Myr old starburst cluster Wd 1. At such a young age, stellar evolution has affected only stars with masses above  $25 M_\odot$  and all other stellar members of this cluster are still on the main sequence or pre-main sequence. Hence, Wd 1 presents a unique opportunity to study its initial mass function (IMF). From the multi-epoch AO observations of Wd 1 we derived the completeness-corrected IMF slope of  $\Gamma = -0.46$  for the cluster center within  $r < 0.23$  pc and for the masses down to  $0.6 M_\odot$ . This value is in a good agreement with the change in mass function found by [Brandner et al. \(2008\)](#) and [Gennaro et al. \(2011\)](#), and confirms that massive stars are segregated in the cluster core. After the correction for the instrumental effects we derived the internal velocity dispersions of  $\sigma_{int_L} = 7.4 \pm 1.0$  km/s in galactic longitude  $l$  and  $\sigma_{int_B} = 4.2 \pm 1.1$  km/s in galactic latitude  $b$  for Wd 1. Our conclusions can be summarized in more detail as follows.

- The AO NAOS/CONICA observations allowed to resolve the Wd 1 center population down to  $0.4 M_\odot$ ;
- Direct NACO to NACO mapping over a 5 years time baseline allowed to achieve better than 1 mas/yr accuracy for the proper motion measurements. For selecting the cluster members we used an algorithm similar to the one described in [Jones](#)

and Walker (1988). The astrometric data enable us to assign cluster membership probabilities to individual stars;

- Non-spherical velocity dispersion  $\sigma_{int_L} : \sigma_{int_B} = 1.8$  is in agreement with the recent results of Gennaro et al. (2011) on elongation of the cluster along the Galactic plane;
- For the first time the completeness-corrected IMF slope  $\Gamma = [-0.5, -0.2]$  was derived for the cluster center within  $r < 0.23$  pc. So far the mass function of Wd 1 was only derived for the outer parts with minimum  $r = 0.75$  pc (Brandner et al., 2008). The calculated cumulative IMF helped to avoid binning biases;
- Our result is consistent with the signs of mass segregation in other Galactic young massive clusters, like NGC 3603 YC (Harayama et al., 2008), Quintuplet (Hußmann et al., 2011) and Arches (Stolte et al., 2002).

Repeated collisions between massive stars in Wd 1 might have led to the formation of an intermediate mass black hole (IMBH) in the core of this dense cluster. The evidence for the existence of IMBH can be obtained from astrometric observations of stars whose motion is dominated by the gravitational influence of the central black hole. The precise measurements of all orbital parameters of the stars near the IMBH and their kinematics will become possible with the GRAVITY instrument in the near future. This will further improve our understanding of the structure of Wd 1 and its formation scenario.

## 5.2 Results on exoplanets

Chapter 4 deals with the astrometric detection of exoplanets around very low mass stars using GRAVITY. GRAVITY is a second generation instrument of the VLTI that is designed to work with all four 8-meter Unit Telescopes. With the expected  $10 \mu\text{as}$  astrometric capability GRAVITY will open a new window in a range of planet masses that can be discovered via astrometry. GRAVITY will focus on detecting exoplanets in close binary systems with angular separation smaller than  $1.7''$ . Our target list includes M-dwarf binaries within 25 pc and binary stars with known RV-exoplanets. We aim to detect 4 Earth mass planets around M-dwarfs in a 5-year survey. In addition, the GRAVITY instrument will be able to measure the position angle of the planet orbit on the sky by observations of transiting exoplanets. The planet orbit orientation combined with measurements of the degree of polarization of light reflected by the planet (e.g. SPHERE ZIMPOL observations), will give an opportunity to place constraints on the distribution of clouds and weather zones on the planet. Our conclusions can be summarized in more detail as follows.

## 5. CONCLUSIONS

---

- GRAVITY is an ideal instrument for the detection of very low mass planets around late-type M dwarfs. Thus far, only 8% of all known exoplanets were found around such dim and faint objects;
- Our estimations show that in a 5-year survey with GRAVITY one can detect planets of 4 Earth masses around late-type M-dwarfs within 10 pc. Maximum distance for an early type M0V star in order to detect the astrometric signature of a 4.2 Jupiter-mass planet at 5 AU with GRAVITY will be 780 pc;
- Our GRAVITY sample selection includes M-dwarf binaries with the angular separation less than 1.7". A big contribution to our target list came with the recent results of an extensive high-resolution imaging survey of M-dwarf multiplicity using the Lucky Imaging technique (Bergfors et al. 2010; Janson et al. 2012). From the 701 M-dwarfs observed during this survey we selected 92 candidates which are suitable for observation with the GRAVITY instrument. Among these candidates 38 are still unconfirmed physical binaries, as common proper motions have yet to be confirmed;
- As the RV method gives only a lower limit to the planet mass, we selected binary stars with known RV-exoplanets for precise astrometric observations with GRAVITY to get all orbital parameters and a true planet mass.

The observations of later type M dwarfs (from M6 to M9) with AstraLux will give an opportunity to find potential targets for the detection of exo-Earthes with GRAVITY.

## 6

# Acronym

<b>2MASS</b>	2 Micron All Sky Survey
<b>ACS</b>	Advanced Camera for Surveys
<b>AGN</b>	Active Galactic Nuclei
<b>AO</b>	Adaptive Optics
<b>AT</b>	Auxiliary Telescope
<b>AU</b>	Astronomical Unit
<b>BC</b>	Before Christ
<b>BSG</b>	Blue SuperGiant
<b>CM</b>	Color-Magnitude
<b>CMD</b>	CM Diagram
<b>DEC</b>	Declination
<b>DM</b>	Distance Modulus
<b>ESA</b>	European Space Agency
<b>ESO</b>	European Southern Observatory
<b>FK5</b>	Fifth Fundamental Catalogue
<b>FOV</b>	Field Of View
<b>FWHM</b>	Full Width at Half Maximum
<b>GAIA</b>	Global Astrometric Interferometer for Astrophysics
<b>GMC</b>	Giant Molecular Cloud
<b>GRAVITY</b>	General Relativity Analysis via VLT InTerferometrY
<b>HARPS</b>	High Accuracy Radial velocity Planet Searcher
<b>HIPPARCOS</b>	HIgh Precision PARallax COLlecting Satellite
<b>HRD</b>	Hertzsprung-Russell Diagram
<b>HST</b>	Hubble Space Telescope
<b>IDL</b>	Interactive Data Language
<b>IMBH</b>	Intermediate Mass Black Hole

## 6. ACRONYM

---

**IMF** Initial Mass Function  
**IR** InfraRed  
**IRAF** Image Reduction and Analysis Facility  
**MACAO** Multi-Applications Curvature Adaptive Optics  
**MF** Mass Function  
**MS** Main Sequence  
**NAOS** Nasmyth Adaptive Optics System  
**NACO** NAOS/CONICA  
**NGC** New General Catalogue  
**NTT** New Technology Telescope  
**ONC** Orion Nebula Cluster  
**OPD** Optical Path Difference  
**PMS** Pre-Main Sequence  
**PRIMA** Phase Referenced Imaging and Microarcsecond Astrometry  
**PSF** Point Spread Function  
**RA** Right Ascension  
**RMS** Root Mean Square  
**RSGC** Red SuperGiant Cluster  
**RV** Radial Velocity  
**SPHERE** Spectro-Polarimetric High-contrast Exoplanet Research  
**TCD** Two-Color Diagram  
**UT** Unit Telescope  
**VLT** Very Large Telescope  
**VLTI** VLT Interferometer  
**Wd 1** Westerlund 1  
**WFC3** Wide Field Camera 3  
**WFPC2** Wide Field Planetary Camera 2  
**YC** Young Cluster  
**YNC** Young Nuclear Cluster  
**ZAMS** Zero Age Main Sequence

# Bibliography

- Adams, F. C., Hollenbach, D., Laughlin, G., and Gorti, U.: 2004, ApJ **611**, 360 [25](#)
- Alexander, M. J., Kobulnicky, H. A., Clemens, D. P., Jameson, K., Pinnick, A., and Pavel, M.: 2009, AJ **137**, 4824 [6](#)
- Allison, R. J., Goodwin, S. P., Parker, R. J., de Grijs, R., Portegies Zwart, S. F., and Kouwenhoven, M. B. N.: 2009, ApJ **700**, L99 [44](#)
- Bartko, H., Gillessen, S., Rabiën, S., Thiel, M., Gräter, A., Haug, M., Kellner, S., Eisenhauer, F., Lacour, S., Straubmeier, C., Berger, J.-P., Jocou, L., Chibani, W., Lüst, S., Moch, D., Pfuhl, O., Fabian, W., Araujo-Hauck, C., Perraut, K., Brandner, W., Perrin, G., and Amorim, A.: 2010, in *Society of Photo-Optical Instrumentation Engineers (SPIE) Conference Series*, Vol. 7734 of *Society of Photo-Optical Instrumentation Engineers (SPIE) Conference Series* [51](#)
- Baumgardt, H., Kroupa, P., and Parmentier, G.: 2008, MNRAS **384**, 1231 [27](#)
- Beccari, G., Spezzi, L., De Marchi, G., Paresce, F., Young, E., Andersen, M., Panagia, N., Balick, B., Bond, H., Calzetti, D., Carollo, C. M., Disney, M. J., Dopita, M. A., Frogel, J. A., Hall, D. N. B., Holtzman, J. A., Kimble, R. A., McCarthy, P. J., O’Connell, R. W., Saha, A., Silk, J. I., Trauger, J. T., Walker, A. R., Whitmore, B. C., and Windhorst, R. A.: 2010, ApJ **720**, 1108 [11](#), [26](#)
- Bedin, L. R., Anderson, J., King, I. R., and Piotto, G.: 2001, ApJ **560**, L75 [11](#)
- Belikov, A. N., Hirte, S., Meusinger, H., Piskunov, A. E., and Schilbach, E.: 1998, A&A **332**, 575 [10](#)
- Bergfors, C., Brandner, W., Janson, M., Daemgen, S., Geissler, K., Henning, T., Hippler, S., Hormuth, F., Joergens, V., and Köhler, R.: 2010, A&A **520**, A54 [59](#), [72](#)
- Bhatt, H. C.: 1989, A&A **213**, 299 [10](#)

## BIBLIOGRAPHY

---

- Bik, A., Henning, T., Stolte, A., Brandner, W., Gouliermis, D. A., Gennaro, M., Pasquali, A., Rochau, B., Beuther, H., Ageorges, N., Seifert, W., Wang, Y., and Kudryavtseva, N.: 2012, *ApJ* **744**, 87 [10](#), [26](#)
- Brandner, W., Clark, J. S., Stolte, A., Waters, R., Negueruela, I., and Goodwin, S. P.: 2008, *A&A* **478**, 137 [ix](#), [11](#), [18](#), [27](#), [29](#), [30](#), [36](#), [43](#), [44](#), [45](#), [70](#), [71](#)
- Brandner, W., Grebel, E. K., Chu, Y.-H., and Weis, K.: 1997, *ApJ* **475**, L45 [11](#)
- Cameron, P. B., Britton, M. C., and Kulkarni, S. R.: 2009, *AJ* **137**, 83 [3](#)
- Campbell, B., Walker, G. A. H., and Yang, S.: 1988, *ApJ* **331**, 902 [53](#)
- Castelli, F. and Kurucz, R. L.: 2004, *ArXiv Astrophysics e-prints* [18](#)
- Chauvin, G., Lagrange, A. ., Udry, S., and Mayor, M.: 2007, *ArXiv e-prints* [62](#)
- Clark, J. S., Negueruela, I., Crowther, P. A., and Goodwin, S. P.: 2005, *A&A* **434**, 949 [10](#), [30](#)
- Clarkson, W. I., Ghez, A. M., Morris, M. R., Lu, J. R., Stolte, A., McCrady, N., Do, T., and Yelda, S.: 2012, *ApJ* **751**, 132 [6](#)
- Clénet, Y., Gendron, E., Rousset, G., Hippler, S., Eisenhauer, F., Gillessen, S., Perrin, G., Amorim, A., Brandner, W., Perraut, K., and Straubmeier, C.: 2010, in *Society of Photo-Optical Instrumentation Engineers (SPIE) Conference Series*, Vol. 7736 of *Society of Photo-Optical Instrumentation Engineers (SPIE) Conference Series* [50](#)
- Commerçon, B., Hennebelle, P., and Henning, T.: 2011, *ApJ* **742**, L9 [10](#)
- Cottaar, M., Meyer, M. R., Andersen, M., and Espinoza, P.: 2012, *A&A* **539**, A5 [16](#), [43](#)
- Crowther, P. A., Hadfield, L. J., Clark, J. S., Negueruela, I., and Vacca, W. D.: 2006, *MNRAS* **372**, 1407 [30](#)
- Cuntz, M., Eberle, J., and Musielak, Z. E.: 2007, *ApJ* **669**, L105 [58](#)
- Da Rio, N., Gouliermis, D. A., and Gennaro, M.: 2010, *ApJ* **723**, 166 [10](#), [11](#)
- Davies, B., Figer, D. F., Kudritzki, R.-P., MacKenty, J., Najarro, F., and Herrero, A.: 2007, *ApJ* **671**, 781 [6](#)
- Davies, B., Figer, D. F., Law, C. J., Kudritzki, R.-P., Najarro, F., Herrero, A., and MacKenty, J. W.: 2008, *ApJ* **676**, 1016 [6](#)
- Delplancke, F.: 2008, *New Astronomy Reviews* **52**, 199 [x](#), [49](#)

## BIBLIOGRAPHY

---

- Devillard, N.: 2001, in F. R. Harnden Jr., F. A. Primini, & H. E. Payne (ed.), *Astronomical Data Analysis Software and Systems X*, Vol. 238 of *Astronomical Society of the Pacific Conference Series*, p. 525 [32](#)
- Eggenberger, A., Udry, S., Chauvin, G., Beuzit, J.-L., Lagrange, A.-M., Ségransan, D., and Mayor, M.: 2007, *A&A* **474**, 273 [62](#)
- Eisenhauer, F., Perrin, G., Brandner, W., Straubmeier, C., Perraut, K., Amorim, A., Schöller, M., Gillessen, S., Kervella, P., Benisty, M., Araujo-Hauck, C., Jocou, L., Lima, J., Jakob, G., Haug, M., Clénet, Y., Henning, T., Eckart, A., Berger, J.-P., Garcia, P., Abuter, R., Kellner, S., Paumard, T., Hippler, S., Fischer, S., Moulin, T., Villate, J., Avila, G., Gräter, A., Lacour, S., Huber, A., Wiest, M., Nolot, A., Carvas, P., Dorn, R., Pfuhl, O., Gendron, E., Kendrew, S., Yazici, S., Anton, S., Jung, Y., Thiel, M., Choquet, É., Klein, R., Teixeira, P., Gitton, P., Moch, D., Vincent, F., Kudryavtseva, N., Ströbele, S., Sturm, S., Fédou, P., Lenzen, R., Jolley, P., Kister, C., Lapeyrière, V., Naranjo, V., Lucuix, C., Hofmann, R., Chapron, F., Neumann, U., Mehrgan, L., Hans, O., Rousset, G., Ramos, J., Suarez, M., Lederer, R., Reess, J.-M., Rohloff, R.-R., Haguenaue, P., Bartko, H., Sevin, A., Wagner, K., Lizon, J.-L., Rabien, S., Collin, C., Finger, G., Davies, R., Rouan, D., Wittkowski, M., Dodds-Eden, K., Ziegler, D., Cassaing, F., Bonnet, H., Casali, M., Genzel, R., and Lena, P.: 2011, *The Messenger* **143**, 16 [6](#), [52](#)
- Els, S. G., Sterzik, M. F., Marchis, F., Pantin, E., Endl, M., and Kürster, M.: 2001, *A&A* **370**, L1 [62](#)
- Eriksson, U. and Lindegren, L.: 2007, *A&A* **476**, 1389 [58](#)
- Forbes, D.: 1996, *JRASC* **90**, 329 [10](#)
- Gennaro, M., Brandner, W., Stolte, A., and Henning, T.: 2011, *MNRAS* **412**, 2469 [6](#), [11](#), [13](#), [14](#), [19](#), [30](#), [31](#), [33](#), [36](#), [40](#), [41](#), [43](#), [70](#), [71](#)
- Harayama, Y., Eisenhauer, F., and Martins, F.: 2008, *ApJ* **675**, 1319 [44](#), [71](#)
- Hatzes, A. P., Cochran, W. D., Endl, M., McArthur, B., Paulson, D. B., Walker, G. A. H., Campbell, B., and Yang, S.: 2003, *ApJ* **599**, 1383 [53](#)
- Hillenbrand, L. A.: 1997, *AJ* **113**, 1733 [26](#)
- Hosokawa, T., Offner, S. S. R., and Krumholz, M. R.: 2011, *ApJ* **738**, 140 [25](#)
- Howard, A. W., Johnson, J. A., Marcy, G. W., Fischer, D. A., Wright, J. T., Bernat, D., Henry, G. W., Peek, K. M. G., Isaacson, H., Apps, K., Endl, M., Cochran, W. D., Valenti, J. A., Anderson, J., and Piskunov, N. E.: 2010, *ApJ* **721**, 1467 [62](#)

## BIBLIOGRAPHY

---

- Hußmann, B., Stolte, A., Brandner, W., and Gennaro, M.: 2011, *ArXiv e-prints* **6**, 27, 34, 44, 71
- Janson, M., Hormuth, F., Bergfors, C., Brandner, W., Hippler, S., Daemgen, S., Kudryavtseva, N., Schmalzl, E., Schnupp, C., and Henning, T.: 2012, *ApJ* **754**, 44 59, 72
- Johnstone, D., Hollenbach, D., and Bally, J.: 1998, *ApJ* **499**, 758 25
- Jones, B. F. and Walker, M. F.: 1988, *AJ* **95**, 1755 16, 35, 70
- Jørgensen, B. R. and Lindegren, L.: 2005, *A&A* **436**, 127 11, 70
- Kharchenko, N. V., Piskunov, A. E., Röser, S., Schilbach, E., and Scholz, R.-D.: 2004, *Astronomische Nachrichten* **325**, 740 34
- Klessen, R. S.: 2001, *ApJ* **550**, L77 10
- Krumholz, M. R., Klein, R. I., McKee, C. F., Offner, S. S. R., and Cunningham, A. J.: 2009, *Science* **323**, 754 10
- Kudryavtseva, N., Brandner, W., Gennaro, M., Rochau, B., Stolte, A., Andersen, M., Da Rio, N., Henning, T., Tognelli, E., Hogg, D., Clark, S., and Waters, R.: 2012, *ApJ* **750**, L44 9
- Kuiper, R., Klahr, H., Beuther, H., and Henning, T.: 2011, *ApJ* **732**, 20 10
- Liermann, A., Hamann, W.-R., and Oskinova, L. M.: 2012, *ArXiv e-prints* 27
- Makarov, V. V., Beichman, C. A., Catanzarite, J. H., Fischer, D. A., Lebreton, J., Malbet, F., and Shao, M.: 2009, *ApJ* **707**, L73 58
- Marigo, P., Girardi, L., Bressan, A., Groenewegen, M. A. T., Silva, L., and Granato, G. L.: 2008, *A&A* **482**, 883 18
- Melena, N. W., Massey, P., Morrell, N. I., and Zangari, A. M.: 2008, *AJ* **135**, 878 10
- Mengel, S. and Tacconi-Garman, L. E.: 2009, *Ap&SS* **324**, 321 43
- Morris, T. and Podsiadlowski, P.: 2009, *MNRAS* **399**, 515 11
- Navarro, J. F., Abadi, M. G., Venn, K. A., Freeman, K. C., and Anguiano, B.: 2011, *MNRAS* **412**, 1203 16
- Naylor, T.: 2009, *MNRAS* **399**, 432 10
- Negueruela, I., Clark, J. S., and Ritchie, B. W.: 2010, *A&A* **516**, A78 11, 43

## BIBLIOGRAPHY

---

- Pang, X., Grebel, E. K., and Altmann, M.: 2010, in R. de Grijs & J. R. D. Lépine (ed.), *IAU Symposium*, Vol. 266 of *IAU Symposium*, pp 24–28 [27](#)
- Paumard, T., Genzel, R., Martins, F., Nayakshin, S., Beloborodov, A. M., Levin, Y., Trippe, S., Eisenhauer, F., Ott, T., Gillessen, S., Abuter, R., Cuadra, J., Alexander, T., and Sternberg, A.: 2006, *ApJ* **643**, 1011 [6](#)
- Raghavan, D., Henry, T. J., Mason, B. D., Subasavage, J. P., Jao, W.-C., Beaulieu, T. D., and Hambly, N. C.: 2006, *ApJ* **646**, 523 [62](#)
- Reggiani, M., Robberto, M., Da Rio, N., Meyer, M. R., Soderblom, D. R., and Ricci, L.: 2011, *A&A* **534**, A83 [10](#)
- Rieke, G. H. and Lebofsky, M. J.: 1985, *ApJ* **288**, 618 [18](#)
- Ritchie, B. W., Clark, J. S., Negueruela, I., and Crowther, P. A.: 2009, *A&A* **507**, 1585 [23](#)
- Robin, A. and Creze, M.: 1986, *A&A* **157**, 71 [36](#)
- Robin, A. C., Reylé, C., Derrière, S., and Picaud, S.: 2004, *A&A* **416**, 157 [36](#)
- Rochau, B., Brandner, W., Stolte, A., Gennaro, M., Gouliermis, D., Da Rio, N., Dzyurkevich, N., and Henning, T.: 2010, *ApJ* **716**, L90 [6](#), [13](#), [16](#), [21](#)
- Sanders, W. L.: 1971, *A&A* **14**, 226 [34](#)
- Schlegel, D. J., Finkbeiner, D. P., and Davis, M.: 1998, *ApJ* **500**, 525 [21](#)
- Shao, M., Catanzarite, J., and Pan, X.: 2010, *ApJ* **720**, 357 [54](#)
- Shao, M. and Colavita, M. M.: 1992, *A&A* **262**, 353 [6](#), [50](#)
- Sharma, S., Pandey, A. K., Ogura, K., Aoki, T., Pandey, K., Sandhu, T. S., and Sagar, R.: 2008, *AJ* **135**, 1934 [23](#)
- Stetson, P. B.: 1987, *PASP* **99**, 191 [13](#), [32](#)
- Stolte, A. and Brandner, W.: 2010, in R. de Grijs and J. R. D. Lépine (eds.), *IAU Symposium*, Vol. 266 of *IAU Symposium*, pp 123–128 [34](#)
- Stolte, A., Brandner, W., Brandl, B., and Zinnecker, H.: 2006, *AJ* **132**, 253 [21](#), [42](#)
- Stolte, A., Brandner, W., Brandl, B., Zinnecker, H., and Grebel, E. K.: 2004, *AJ* **128**, 765 [10](#), [25](#)

## BIBLIOGRAPHY

---

- Stolte, A., Ghez, A. M., Morris, M., Lu, J. R., Brandner, W., and Matthews, K.: 2008, *ApJ* **675**, 1278 [34](#)
- Stolte, A., Grebel, E. K., Brandner, W., and Figer, D. F.: 2002, *A&A* **394**, 459 [44](#), [71](#)
- Sung, H. and Bessell, M. S.: 2004, *AJ* **127**, 1014 [21](#)
- Tognelli, E., Prada Moroni, P. G., and Degl’Innocenti, S.: 2011, *A&A* **533**, A109 [18](#)
- Trujillo, I., Aguerri, J. A. L., Cepa, J., and Gutiérrez, C. M.: 2001, *MNRAS* **328**, 977 [32](#)
- Tuomi, M., Kotiranta, S., and Kaasalainen, M.: 2009, *A&A* **494**, 769 [54](#)
- Wolszczan, A. and Frail, D. A.: 1992, *Nature* **355**, 145 [53](#)
- Zinnecker, H. and Yorke, H. W.: 2007, *ARA&A* **45**, 481 [10](#), [25](#)

## Acknowledgements

First of all I would like to thank IMPRS-HD for giving such a great opportunity for international students to study abroad, to collaborate with scientists from all over the world, to participate in numerous interesting conferences.

I would like to thank my supervisors Wolfgang Brandner, Stefan Hippler and Thomas Henning for proposing this exciting project and for their help along the way. I spent really pleasant and useful time during my PhD in Heidelberg. Many special thanks to Wolfgang Brandner for his encouragement, his scientific advice and his accurate explanations.

I would like to express my gratitude to my co-authors and colleagues: Andrea Stolte, Mario Gennaro, Boyke Rochau, Maria Lenius and Carolina Bergfors for valuable and illuminating comments and helpful discussions.

Many thanks to all my friends for cheering me up and for having so many good times together and especially to our table tennis team for really good breakes after lunch.

Thanks to the IMPRS coordinator Christian Fendt for his help.

Most of all I would like to thank my family. My parents, grandparents, my brother and his wife for their great support, their reliable advice and for believing in me at all times.